Order Number 9018997

Theoretical study of the interaction of hydrogen with metals

Yu, Rici, Ph.D.

University of Hawaii, 1989

U·M·I
300 N. Zeeb Rd.
Ann Arbor, MI 48106

Theoretical Study of the Interaction of Hydrogen with Metals

A DISSERTATION SUBMITTED TO THE GRADUATE DIVISION OF
THE UNIVERSITY OF HAWAII IN PARTIAL FULFILLMENT
OF THE REQUIREMENTS FOR THE DEGREE OF

DOCTOR OF PHILOSOPHY

IN PHYSICS

DECEMBER 1989

By

Rici Yu

Dissertation Committee:

Pui K. Lam, Chairman
Charles S. Fadley
James R. Gaines
William Pong
Chester A. Vause

ACKNOWLEDGMENTS

I wish to thank my thesis advisor, Professor Pui K. Lam, for his guidance and encouragement.

I would also like to thank Professors Charles Fadley, James Gaines, William Pong, and Chester Vause for their serving on my dissertation committee.

I am very grateful to Professor T. D. Lee and others who were involved in the CUSPEA program, under which I was able to come to Hawaii.

Various computation facilities were utilized for the work presented in this dissertation. Thanks are due to the San Diego Supercomputer Center for use of the CRAY X-MP, the high energy physics group at the University of Hawaii at Manoa for use of its VAX, and the University of Hawaii computing center. Consultations at these computing facilities are deeply appreciated. I would also like to thank Diane Ibaraki for helping with using TEX.

I give my special thanks to my parents for their encouragement and support during my graduate career.

ABSTRACT

Electronic structure calculations are carried out for simple metal hydrides and hydrogen adsorption on simple metal surfaces. The studies are based on the *ab initio* pseudopotential method and the local-density approximation.

Structural and electronic properties of magnesium hydride are studied. The calculated structural properties include equilibrium lattice parameters, cohesive energy, elastic constants, bulk modulus, and phonon frequency. The electronic band structure, density of states, charge density distribution are also obtained. Superconductivity in doped magnesium hydride is proposed. Lithium beryllium hydride is studied because of its proposed metallic behavior. The relative stability of two perovskite structures of lithium beryllium hydride is investigated. Band structures are calculated under ambient and high pressure conditions to determine whether the structures are metallic.

The adsorption of hydrogen on the close-packed surface of Be and Mg are studied. The equilibrium distance between hydrogen and the surfaces, the adsorption energy, and the hydrogen oscillation frequency are calculated for hydrogen in the high-symmetry adsorption sites. The energetics for hydrogen to go into a subsurface site is also investigated. Charge density distribution, work function and potential are studied for the clean and hydrogen-covered surfaces. Electronic band structure and H-induced surface states are determined for hydrogen adsorption on Be. Surface energy of the clean surfaces is also calculated.

TABLE OF CONTENTS

LIST OF TABLES

LIST OF FIGURES

Chapter I

Introduction

This thesis reports the results of band structure calculations of simple metal hydrides and hydrogen adsorption on simple metal surfaces. Various structural and electronic properties are calculated to elucidate the metal-hydrogen interactions in the bulk and on the surface.

Metal hydrides are compounds of metal (metal alloys) and hydrogen, which may exist over a broad range of composition [1]. The existence of a variety of fundamental physical phenomena in metal hydrides and various applications have lead to their intense study [2–5]. The occurrences of superconductivity with elevated transition temperatures (T_c) in hydrides of thorium (Th_4H_{15}) and palladium (PdH) are marked examples, whose discovery in the early seventies [6] have in fact aroused renewed interest in these materials. The coupling of the hydrogen optical-phonon modes with electrons is believed to be important [6] for the superconductivity in these compounds. The highest T_c in metal hydrides so far is about 17 K in hydrides of Pd-Cu alloys [6]. This is low compared to the conjectured T_c of metallic hydrogen [7]. To improve on T_c, simple metal hydrides may be advantageous in that the valence electrons are expected to be largely of hydrogen character. The electron-phonon coupling is sizeable compared to transition metal and rare earth hydrides [8]. However, simple metal hydrides are usually insulating. Before any progress can be made in improving T_c in hydrides, stable metallic hydrides of simple metals have to be found. Besides the basic properties, metal hydrides are also of interest because of their use in various applications. For instance, the formation of hydrides is a good way of storing

hydrogen [9]. This could become useful, e.g., in vehicular applications. Here the light-weight magnesium hydride is a potential candidate [10]. Electronic properties of many transition metal hydrides have now been studied experimentally and theoretically [11]. On the other hand, very little is known about the electronic properties of simple metal hydrides. A better understanding of the bonding and the resulting electronic structure in these materials is necessary in order to explore possible interesting properties such as superconductivity and to utilize them in different applications.

A related subject is the adsorption of hydrogen on metal surfaces. As part of the surface physics, properties of atoms and molecules upon their adsorption on surfaces have been studied extensively [12]. Because of the simple electronic structure of hydrogen, its adsorption on a variety of transition metal surfaces has been investigated experimentally and theoretically [12]. On the other hand, properties of hydrogen adsorbed on simple metal surfaces have not been well studied. The interaction of the hydrogen and the metal surfaces is important for the absorption and desorption of hydrogen in the metal host and thus relates also to hydrogen storage in metals.

In this thesis, we investigate the fundamental properties of the simple metal hydrides and the hydrogen adsorption on simple metal surfaces via band structure theory. The *ab initio* pseudopotential method [13] is used. Two bulk hydrides (magnesium hydride and lithium beryllium hydride) are studied. As mentioned above, the former is a potential candidate as storage medium for vehicular application. Various structural and dynamical properties such as equilibrium lattice constants, bulk modulus, elastic constants, and a phonon frequency are calculated. Electronic band structure and charge density distribution are obtained.

We also suggest doping as a way of inducing metallic behavior and superconductivity. Lithium beryllium hydride was proposed as a good candidate for high-T_c superconductivity [14]. The equilibrium structural properties of $LiBeH_3$ in two assumed perovskite structures are calculated. The electronic structures at normal and high pressures are examined. Studies of hydrogen adsorption are made on H on the (0001) surface of two hcp metals, Be and Mg. The stable adsorption site, equilibrium distance between H and the surfaces and the hydrogen vibrational frequency are calculated. The energetics for hydrogen to go into a subsurface site is investigated. The changes in the charge distribution and work function upon the adsorption of hydrogen are studied. The electronic band structure is obtained and hydrogen-induced surface states are identified for H on Be(0001).

The rest of the thesis is organized as follows. In Chapter II, brief reviews are given of the theoretical methods utilized in the electronic structure calculations. In Chapter III, we describe the result of the electronic structure calculations on magnesium hydride and lithium beryllium hydride. In Chapter IV, the results of the calculations on hydrogen adsorption on the Be(0001) and Mg(0001) surfaces are described and discussed. A summary of all results and conclusions is given in Chapter V.

References for Chapter I

[1] W. M. Muller, J. P. Blackledge, and G. G. Libowitz (eds.), *Metal Hydrides* (Academic, New York, 1968); K. M. Mackay, *Comprehensive Inorganic Chemistry*, 1st ed. (Pergamon, New York, 1973), Vol. 1.

[2] G. Alefeld and J. Völkl (eds.), *Hydrogen in Metals* I and II (Springer, New York, 1978).

[3] G. Bambakidis (ed.), *Metal Hydrides* (Plenum, New York, 1981).

[4] P. Jena and C. B. Satterthwaite (eds.), *Electronic Structure and Properties of Hydrogen in Metals* (Plenum, New York, 1983).

[5] L. Schlapbach (ed.), *Hydrogen in Intermetallic Compounds* I and II (Springer, New York, 1988).

[6] See B. Stritzker and H. Wühl, in *Hydrogen in Metals* II, edited by G. Alefeld and J. Völkl (Springer, New York, 1978), p. 243.

[7] Estimates of T_c are around 250 K. See T. Schneider, Helv. Phys. Acta **42**, 957 (1969); A. C. Switendick, in *Superconductivity in d- and f-Band Metals* edited by D. H. Douglass (Plenum, New York, 1976), p. 593; D. A. Papaconstantopoulos and B. M. Klein, Ferroelectrics **16**, 307 (1977).

[8] M. Gupta, in Ref. 4, p. 321.

[9] See, e.g., R. Wiswall, in *Hydrogen in Metals* II, edited by G. Alefeld and J. Völkl (Springer, New York, 1978), p. 202.

[10] P. Selvam, B. Viswanathan, C. S. Swamy, and V. Srinivasan, Int. J. Hydrogen Energy **11**, 169 (1986).

[11] A. C. Switendick, in *Hydrogen in Metals* I, edited by G. Alefeld and J. Völkl (Springer, New York, 1978), p. 101; M. Gupta, in *The Electronic Structure of Complex Systems*, edited by P. Phariseau and W. M. Temmerman (Plenum, New York, 1984), p.243; M. Gupta and L. Schlapbach, in *Hydrogen in Intermetallic Compounds* I, edited by L. Schlapbach (Springer, New York, 1988), p. 139.

[12] J. P. Muscat and D. M. Newns, in *Progress in Surface Physics*, edited by S. G. Davison (Pergamon, New York, 1978), Vol. 9, p. 1; T. N. Rhodin and G. Ertl (eds.), *The Nature of Surface Chemical Bond* (North-Holland, New York, 1979).

[13] M. L. Cohen and V. Heine, in *Solid State Physics*, edited by H. Ehrenreich, F. Seitz, and D. Turnbull (Academic, New York, 1970), Vol. 24, p. 37; D. R. Hamann, M. Schlüter, and C. Chiang, Phys. Rev. Lett. **43**, 1494 (1979).

[14] A. W. Overhauser, Phys. Rev. B **35**, 411 (1987).

Chapter II

Theoretical Methods

In this chapter, a brief review is given of the theories which are applied to the electronic structure calculations described in Chapter III and IV. Sec. 1 deals with the density functional theory of a many-electron system and its application in the electronic structure calculations. In Sec. 2, the development of the pseudopotential method and the generation of the accurate norm-conserving pseudopotentials are discussed. Finally, the formulation of the electronic structure calculation in the reciprocal space is outlined in Sec. 3. The Rydberg atomic units will be used: $\hbar = e = a_B = 1$ and energies are in Rydberg.

1. Density Functional Formalism

In this section, we discuss the density functional theory (DFT) of a many-electron system and the application of the theory to the electronic structure calculation. We shall only concern ourselves with the basic formulation and the results that are pertinent to our electronic structure calculations. Further details and applications of the theory can be found in the reviews on the subject [1–5].

1.1 Basic Formalism

DFT had its origin in the Thomas-Fermi theory [6] of electron gas. In the Thomas-Fermi theory, a many-electron system is broken up into small cells. The electrons in each of these cells is treated as a homogeneous electron gas and is thus uniquely described by the electron density within the volume. The problem is then

reduced to finding the electron density as a function of position. The importance of the ground-state electron density distribution of a general electronic system was pointed out by Hohenberg and Kohn [7].. The fundamental theorem involved can be stated as follows.

Theorem. Let $\rho_0(\mathbf{r})$ and $\rho_0'(\mathbf{r})$ be the ground-state electron density of two electronic systems whose external potentials are $v(\mathbf{r})$ and $v'(\mathbf{r})$, respectively. If $\rho_0(\mathbf{r}) = \rho_0'(\mathbf{r})$, $v(\mathbf{r}) = v'(\mathbf{r})$; or conversely, if $v(\mathbf{r}) \neq v'(\mathbf{r})$, $\rho_0(\mathbf{r}) \neq \rho_0'(\mathbf{r})$.

Physically, this means that the external potential is uniquely determined by the ground-state electron density. This theorem is valid regardless of whether the ground state is degenerate or not [5] (for simplicity, we shall assume the ground state is non-degenerate in what follows). Since to a given external potential there corresponds a unique ground-state energy, it follows from the above theorem that the ground-state energy is completely determined by the ground-state electron density. Furthermore, since the ground-state wave function is fixed by the external potential, every physical ground-state property of a system is completely determined by its ground-state electron density distribution.

To determine the ground-state electron density given an external potential $v(\mathbf{r})$, an energy functional $E_v[\rho]$ is defined for an arbitrary electron-density distribution $\rho(\mathbf{r})$. Let $\Psi_{\rho,\nu}$ be the class of normalized antisymmetric wave functions which give the electron density $\rho(\mathbf{r})$ [8], then

$$E_v[\rho] \equiv \int \rho(\mathbf{r})\, v(\mathbf{r})\, d\mathbf{r} + F[\rho], \tag{2.1a}$$

where

$$F[\rho] \equiv min_\nu \, <\Psi_{\rho,\nu}|(T+U)|\Psi_{\rho,\nu}> \tag{2.1b}$$

minimized with respect to all ν. By definition, $F[\rho]$ is a universal functional of the electron density because it is independent of $v(\mathbf{r})$. This functional consists of the kinetic energy and the electron-electron interaction energy, which in turn is composed of Hartree energy and the exchange and correlation energy,

$$F[\rho] = T_s[\rho] + \iint \frac{\rho(\mathbf{r})\,\rho(\mathbf{r}')}{|\mathbf{r}-\mathbf{r}'|}\,d\mathbf{r}\,d\mathbf{r}' + E_{xc}[\rho]. \tag{2.2}$$

From the Rayleigh-Ritz variational principle, it is easily shown that for a given external potential $v(\mathbf{r})$, the energy functional $E_v[\rho]$ is minimized when $\rho(\mathbf{r})$ is the ground state electron density $\rho_0(\mathbf{r})$, and $E_v[\rho_0]$ is the ground state energy. The ground-state electron density and energy can thus be obtained variationally if the functional $F[\rho]$ is known. In practice, approximations are used for $T_s[\rho]$ and $E_{xc}[\rho]$ [7]. The solution by variation of electron density is referred to as the statistical approach, as is the Thomas-Fermi theory [6].

1.2 Kohn-Sham Equation

In analogy to the Hartree theory, Kohn and Sham [9] proposed the solution to the DFT description of a many-electron system by self-consistently solving a Schrödinger equation for single-particle states which, unlike the Hartree equation, includes also the exchange and correlation effects. To derive this equation, one writes the electron density and the kinetic energy functional in terms of single-particle wave functions,

$$\rho(\mathbf{r}) = \sum_i |\psi_i(\mathbf{r})|^2 \tag{2.3a}$$

and

$$T_s[\rho] = -\sum_i \int \psi_i^*(\mathbf{r})\,\nabla^2\psi_i(\mathbf{r})\,d\mathbf{r}. \tag{2.3b}$$

By performing variation on the energy functional $E_v[\rho]$ with respect to $\psi_i(\mathbf{r})$, one obtains the equations for the single-particle wave functions,

$$[-\nabla^2 + v_{\rm eff}(\mathbf{r})]\,\psi_i(\mathbf{r}) = \epsilon_i\,\psi_i(\mathbf{r}), \tag{2.4}$$

where the effective potential is given by

$$v_{\rm eff}(\mathbf{r}) = v(\mathbf{r}) + \int \frac{\rho(\mathbf{r}')}{|\mathbf{r}-\mathbf{r}'|}\,d\mathbf{r}' + v_{\rm xc}(\mathbf{r}). \tag{2.5}$$

The term $v_{\rm xc}(\mathbf{r})$ is the exchange and correlation potential. Eqs. (2.4) and (2.3a) constitute the Kohn-Sham (KS) self-consistent equations.

The local-density approximation is frequently utilized. In this approximation, the exchange and correlation energy density at a point $\mathbf{r}$ depends upon the electron density at $\mathbf{r}$ only,

$$E_{\rm xc}[\rho] = \int \rho(\mathbf{r})\,\epsilon_{\rm xc}(\rho(\mathbf{r}))\,d\mathbf{r}. \tag{2.6}$$

The function $\epsilon_{\rm xc}(\rho)$ is the local average exchange-correlation energy per electron. The definition of exchange and correlation follows from the results of homogeneous electron gas [9],

$$\epsilon_{\rm xc}(\rho) = -\frac{9}{4\pi}\alpha(3\pi^2\rho)^{1/3} + \epsilon_{\rm c}(\rho), \tag{2.7}$$

where $\alpha = \frac{2}{3}$ [9,10]. The first term is the exchange energy and the second the correlation energy. The exact form of $\epsilon_{\rm c}(\rho)$ is not known, although asymptotic forms have been calculated in the high electron density [11] and the low electron density [12] limits. From eq. (2.7), we obtain the exchange-correlation potential (eq. (2.5)),

$$\begin{aligned} v_{\rm xc} &= \frac{\delta}{\delta\rho}[\rho\epsilon_{\rm xc}(\rho)] \\ &= -\frac{3\alpha}{\pi}[3\pi^2\rho(r)]^{1/3} + \frac{\delta}{\delta\rho}[\rho\epsilon_{\rm c}(\rho)]. \end{aligned} \tag{2.8}$$

A number of expressions for $\epsilon_c(\rho)$ have been proposed [10,12–15]. They are widely used in electronic structure calculations.

The above formulation of the exchange-correlation potential is appropriate for the paramagnetic (non-spin-polarized) ground state of an electronic system, in which the spin-up electron density is equal to the spin-down electron density. In magnetic systems, the electron density for one spin is greater than that for the other. The exchange and correlation potential for spin-up electrons is then different from that for spin-down electrons [16]. In our bulk and surface calculations described in Chapters III and IV, we will assume that the paramagnetic state is the ground state.

2. Pseudopotential

A pseudopotential is an effective potential which simulates the interaction between the inert atomic core (nucleus and core electrons) and the valence electrons.

When atoms approach each other to form solids, the valence orbitals undergo significant changes. The core orbitals are, on the other hand, relatively inert and can be understood in terms of the tight-binding description. The slow variation of the valence orbitals away from the atomic cores can be readily represented by plane waves. However, the plane waves are not suitable for the rapidly oscillatory behavior of the valence orbitals in the core regions. To overcome this difficulty, Herring [17] had introduced the orthogonalized-plane-wave (OPW) method in which the basis functions acquire the necessary oscillatory behavior by mixing the plane waves with the core states. The resulting matrix elements between the OPW basis functions prove to be much smaller than those between the plane

waves. The pseudopotential method was introduced by Phillips and Kleinman [18] by reformulating the OPW method. They showed that if the smooth parts of the OPW eigenfunctions are treated as the eigenstates the corresponding potential, the pseudopotential is much weaker in the core region than the true attractive potential. Thus by dealing with the pseudo-wave-function (the smooth part of the OPW wave function), the problems of fast oscillation of the valence orbitals and the strong potential in the core region are eliminated.

Early efforts in the application of the pseudopotential were based on empirical approaches. The pseudopotentials were determined from fitting to experimental data such as the Fermi surface geometry of metals and the optical spectral data of semiconductors and insulators. Another characteristics of the early pseudopotential studies is that the electronic part of the potential was not self-consistently determined. Instead, the ionic pseudopotentials were screened with certain dielectric functions. Since the electron-electron interaction was not treated self-consistently, these pseudopotentials determined from fitting the bulk properties were not accurate enough to be used to study systems with different chemical environments (e.g., molecules, surfaces). Earlier work on pseudopotentials and their applications have been discussed extensively in the reviews of Heine, Cohen and Heine, and Heine and Weaire [19] and in the texts by Harrison [20] and Phillips [21].

The development of the density functional formalism (see Sec. 1 of this chapter) allows the interaction between the valence electrons to be determined from the electron charge density. Within the DFF, ionic pseudopotentials can be deduced from self-consistent calculations for a given atom, without recourse to any experimental data (thus the term *ab initio* pseudopotential). There exist several

schemes of constructing *ab initio* pseudopotentials [22–25]. A method introduced by Hamann, Schlüter, and Chiang [24,26] is described in the following.

One starts with a reference state of an atom for which an all-electron calculation is performed in the local-density functional formalism. Assuming spherical symmetry of the electronic potential, the electronic orbitals are of the form

$$\Psi_{nlm}(r,\theta,\phi) = \frac{U_{nl}(r)}{r} Y_{lm}(\theta,\phi). \tag{2.9}$$

To find the radial wave function, one must solve the following self-consistent Kohn-Sham equations

$$\left(-\frac{\partial^2}{\partial r^2} + \frac{l(l+1)}{r^2} - \frac{2Z}{r} + V_{\rm hxc}[\rho(r)]\right) U_{nl}(r) = \epsilon_{nl}\, U_{nl}(r), \tag{2.10a}$$

$$\rho(r) = \sum_{n,l} f_{nl}\, \frac{U_{nl}^2(r)}{4\pi r^2}, \tag{2.10b}$$

where $V_{\rm hxc}[\rho(r)]$ is the sum of Hartree, exchange and correlation potentials, $\rho(r)$ is the electron density, and f_{nl} is the number of electrons occupying the orbital nl. We want to replace the nuclear potential $(-\frac{2Z}{r})$ with some ionic pseudopotentials, $V_{\rm ps}^l(r)$, which would reproduce the eigenenergies of the *valence* orbitals to a certain accuracy. That is, the pseudopotentials must satisfy

$$\left(-\frac{\partial^2}{\partial r^2} + \frac{l(l+1)}{r^2} + V_{\rm ps}^l(r) + V_{\rm hxc}[\tilde{\rho}(r)]\right) \chi_{nl}(r) = \epsilon_{nl}\, \chi_{nl}(r), \tag{2.11a}$$

$$\tilde{\rho}(r) = \sum_{n,l} f_{nl}\, \frac{\chi_{nl}^2(r)}{4\pi r^2}, \tag{2.11b}$$

where $\tilde{\rho}(r)$ is the pseudo-valence charge density and the summation runs over all the *valence states* [27]. As for the pseudo-wave-functions, $\chi_{nl}(r)$, one requires that

(1) they should be nodeless because they are the lowest-energy states of the pseudo-hamiltonian among those that have the same angular momentums.

(2) when normalized, they should be identical to the corresponding true wave functions beyond some core radius R_c.

To find pseudopotentials with the above properties, an inverse procedure is used. First the pseudo-wave-functions satisfying the above two conditions are generated by modifying the corresponding true eigenfunctions inside the core. This is done by making a smooth continuation of the true wave function at a chosen core radius to small values of r. The radial Schrödinger equation, Eq. (2.11a), is then inverted for each valence state to determine the pseudopotentials with the above pseudo-wave-functions as its eigenstate at the correct eigenvalue.

$$V_{ps}^{l}(r) = \frac{1}{\chi_{nl}} \frac{\partial^2 \chi_{nl}}{\partial r^2} + \epsilon_{nl} - \frac{l(l+1)}{r^2} - V_{hxc}[\tilde{\rho}(r)]. \tag{2.12}$$

Because of condition (2) for the pseudo-wave-functions, the pseudopotentials are called *norm-conserving* pseudopotentials.

The pseudopotentials thus generated are obviously identical to the full potential beyond the core radius R_c and correctly simulate the scattering properties of the full potential in the core region at the eigenvalue energies and for the particular angular-momentum values under discussion. In order for the pseudopotentials to be transferable to other chemical environment, e.g., molecules and solids, they must also simulate well the scattering for configurations of the atom other than the reference state. An important transferability criterion can be shown to be satisfied by the norm-conserving pseudopotentials [24,26].

The construction of any pseudopotential is naturally based on the assumption of a frozen core charge. This assumption is valid for solids because (i) the cores do not overlap with each other except for under very high pressures and (ii) the valence electrons and core electrons occupy separate spatial regions. Thus the

core-core interaction is simply the Coulomb interaction. The change in the core wave functions due to potentials of the valence electrons and adjacent ions is negligible. Since the pseudopotentials represent the effective potential exerted by the core on the valence electrons, the pseudopotentials must also be unchanged if the core states are unchanged. The error in the total energy associated with the frozen core approximation has been shown to be of the second order in the change in the valence charge density [28]. Combined with the norm-conserving property, the pseudopotentials do not lead to any first-order transferability error.

3. Electronic Structure and Total Energy Calculations

In the pseudopotential approach, it is customary to use plane waves as basis functions [29]. A Bloch wave function at the wave vector $\mathbf{k}_i$ in the Brillouin zone (BZ) is written as

$$\psi_i(\mathbf{r}) = \sum_{\mathbf{G}} \psi_i(\mathbf{G})\, e^{i(\mathbf{G}+\mathbf{k}_i)\cdot\mathbf{r}}, \tag{2.13}$$

where the summation runs over the reciprocal lattice vectors $\mathbf{G}$. The ionic pseudopotential of an atom is from the previous section,

$$V_{\rm ps} = \sum_l V^l(r)\, P_l, \tag{2.14}$$

where P_l projects out the part of a wave function with angular quantum number l. In practice, it is convenient to separate out a local pseudopotential,

$$\begin{aligned} V_{\rm ps} &= V(r) + \sum_l [\, V^l(r) - V(r)]\, P_l \\ &= V(r) + \sum_l W^l(r)\, P_l, \end{aligned} \tag{2.15}$$

The local part of the pseudopotential, $V(r)$, is usually chosen to be the pseudopotential, $V^l(r)$, for some l [30]. It then has the correct long-range Coulomb

behavior, i.e., $-2Z_c/r$ with Z_c being the valence charge. The nonlocal potentials, $W^l(r)$, are short-ranged. With the above definitions, the single-particle KS equation (Eq.(2.5)) becomes in the reciprocal space,

$$\sum_{\mathbf{G}'} \left((\mathbf{k}_i + \mathbf{G}')^2 \, \delta_{\mathbf{G}\mathbf{G}'} + V^i_{\mathbf{G}\mathbf{G}'} \right) \psi_i(\mathbf{G}') = \epsilon_i \psi_i(\mathbf{G}), \tag{2.16a}$$

where

$$\begin{aligned} V^i_{\mathbf{G}\mathbf{G}'} = & V_{\mathrm{H}}(\mathbf{G}' - \mathbf{G}) \; + v_{\mathrm{xc}}(\mathbf{G}' - \mathbf{G}) \; + V_{\mathrm{L}}(\mathbf{G}' - \mathbf{G}) \\ & + V_{\mathrm{NL}}(\mathbf{k}_i + \mathbf{G}, \mathbf{k}_i + \mathbf{G}'). \end{aligned} \tag{2.16b}$$

The first three terms in Eq. (2.16b) are the Fourier transforms of the Hartree potential, the exchange-correlation potential, and the local pseudopotential, respectively. The last term, due to the nonlocal pseudopotentials, depends on $\mathbf{k}_i$, and on $\mathbf{G}$ and $\mathbf{G}'$ separately. The Hartree and the exchange-correlation energy are calculated from the electron charge density distribution (see Section 1), which is obtained by summing over a finite number of k-points as an approximation to the integration over BZ,

$$\rho(\mathbf{r}) = \sum_i |\psi_i(\mathbf{r})|^2, \tag{2.17}$$

The solutions to Eq. (2.16) and (2.17) are obtained via iteration.

The total static energy (not including lattice vibrations) of a crystal is the sum of the ion-ion interaction energy (E_{ion}), electron-ion interaction energy, and the electronic energy as given by Eq. (2.2). We thus have

$$\begin{aligned} E_{\mathrm{total}} = E_{\mathrm{ion}} + & \sum_i \int \psi_i^*(\mathbf{r}) V_{\mathrm{ps}} \psi_i(\mathbf{r}) \, d\mathbf{r} - \sum_i \int \psi_i^*(\mathbf{r}) \nabla^2 \psi_i(\mathbf{r}) \, d\mathbf{r} \\ & + \frac{1}{2} \int \rho(\mathbf{r}) V_{\mathrm{H}}(\mathbf{r}) \, d\mathbf{r} + \int \rho(\mathbf{r}) \epsilon_{\mathrm{xc}}(\mathbf{r}) \, d\mathbf{r}, \end{aligned} \tag{2.18}$$

where V_{ps} is the total (nonlocal) ionic pseudopotential. As in Eq. (2.17), the sum over i is an approximation to the integration over BZ. The evaluation of the

long-range Coulomb interactions requires special consideration since the individual terms are divergent. The Coulomb energy of a system consisting of point ions of charges $Z_c^{(j)}$ at the atomic sites immersed in a uniform average electron density is called Ewald energy and is given by

$$\gamma_{\text{Ewald}} = E_{\text{ion}} - \frac{1}{\Omega}\int \frac{Z^2}{r}\,d\mathbf{r}, \tag{2.19}$$

where Ω is the unit cell volume and $Z = \sum_j Z_c^{(j)}$ is the total number of valence electrons per unit cell. Eq. (2.19) is evaluated using the Ewald summation technique. The total energy per unit cell can now be written in the reciprocal space,

$$\begin{aligned} E_{\text{total}} = \Omega\Bigg[&\sum_{i,\mathbf{G}} |\psi_i(\mathbf{G})|^2(\mathbf{k}_i+\mathbf{G})^2 + \sum_{\mathbf{G}\neq\mathbf{0}} \rho(\mathbf{G})V_{\text{L}}(\mathbf{G}) \\ &+ \sum_{i,\mathbf{G},\mathbf{G}'} \psi_i^*(\mathbf{G}')\psi_i(\mathbf{G})V_{\text{NL}}(\mathbf{k}_i+\mathbf{G}',\mathbf{k}_i+\mathbf{G}) \\ &+ \frac{1}{2}\sum_{\mathbf{G}\neq\mathbf{0}} \rho(\mathbf{G})V_{\text{H}}(\mathbf{G})\Bigg] + E_{\text{xc}} + \alpha_1 Z + \gamma_{\text{Ewald}}\,. \end{aligned} \tag{2.20}$$

The terms in the brackets are the kinetic energy, electron-ion interaction energy (local and nonlocal terms), and the electron Coulomb energy, respectively. Note that $\rho(\mathbf{G}=\mathbf{0})$ (a uniform electron charge background) is not included in the summations because it is included in the Ewald term. The exchange and correlation energy, E_{xc}, is calculated in real space since ϵ_{xc} is nonlinear in $\rho(\mathbf{r})$. The term $\alpha_1 Z$, where

$$\alpha_1 = \frac{4\pi}{\Omega}\sum_j \int [V^{(j)}(r) + \frac{2Z_c^{(j)}}{r}]r^2\,dr, \tag{2.21}$$

with j running over all atoms in a unit cell, is due to deviations of the local pseudopotentials from the potentials of the point ions. Eq. (2.20) contains a double sum (the nonlocal potential term), whose computation is time-consuming.

Thus a different formula is used for calculating the total energy. From Eq. (2.20) and (2.16), we have

$$E_{\text{total}} = \sum_i e_i - \Omega \sum_{\mathbf{G}\neq\mathbf{0}} \rho(\mathbf{G}) \left[\frac{1}{2} V_{\text{H}}(\mathbf{G}) + v_{\text{xc}}(\mathbf{G})\right] + E_{\text{xc}} + \alpha_1 Z + \gamma_{\text{Ewald}}\,, \tag{2.22}$$

where the first term is the band-structure energy.

References for Chapter II

[1] O. Gunnarsson and R. O. Jones, Phys. Scr. **21**, 394 (1980).

[2] W. Kohn and P. Vashishta, in *Theory of the Inhomogeneous Electron Gas*, edited by S. Lundqvist and N. H. March (Plenum, New York, 1983), p. 79.

[3] A. R. Williams and U. von Barth, in *Theory of the Inhomogeneous Electron Gas*, edited by S. Lundqvist and N. H. March (Plenum, New York, 1983), p. 189.

[4] U. von Barth 1984, in *The Electronic Structure of Complex Systems*, edited by P. Phariseau and W. M. Temmerman (Plenum, New York, 1984), p. 67.

[5] W. Kohn, in *Highlights of Condensed Matter Theory*, edited by F. Bassani, F. Fumi, and M. P. Tosi (North-Holland, New York, 1985), p. 1.

[6] See N. H. March, in *Theory of the Inhomogeneous Electron Gas*, edited by S. Lundqvist and N. H. March (Plenum, New York, 1983), p. 1.

[7] P. Hohenberg and W. Kohn, Phys. Rev. **136**, B864 (1964).

[8] M. Levy, Phys. Rev. A **26**, 1200 (1982).

[9] W. Kohn and L. J. Sham, Phys. Rev. **140**, A1133 (1965).

[10] J. C. Slater, *The Self-Consistent Field for Molecules and Solids* (McGraw-Hill, New York, 1974), vol. 4, p. 12.

[11] M. Gell-Mann and K. Brueckner, Phys. Rev. **106**, 364 (1957).

[12] E. Wigner, Phys. Rev. **46**, 1002 (1934). See also, D. Pines, *Elementary Excitations in Solids* (Benjamin, New York, 1963).

[13] L. Hedin and B. I. Lundqvist, J. Phys. C 4, 2064 (1971).

[14] O. Gunnarsson, B. I. Lundqvist, and J. W. Wilkins, Phys. Rev. B **12**, 1257 (1975).

[15] D. M. Ceperly and B. J. Alder, Phys. Rev. Lett. **45**, 566 (1980); J. P. Perdew and A. Zunger, Phys. Rev. B **23**, 5048 (1981).

[16] U. von Barth and L. Hedin, J. Phys. C **5**, 1629 (1972).

[17] C. Herring, Phys. Rev. **57**, 1169 (1940).

[18] J. C. Phillips and L. Kleinman, Phys. Rev. **116**, 287 (1959).

[19] V. Heine, in *Solid State Theory*, edited by H. Ehrenreich, F. Seitz, and D. Turnbull (Academic, New York, 1970), Vol. 24, p. 1; M. L. Cohen and V. Heine, *ibid.*, p. 37; V. Heine and D. Weaire, *ibid.*, p. 249.

[20] W. A. Harrison, *Pseudopotentials in the Theory of Metals* (Benjamin, New York, 1966).

[21] J. C. Phillips, *Bonds and Bands in Semiconductors* (Academic, New York, 1973).

[22] A. Zunger, J. Vac. Sci. Technol. **16**, 1337 (1979).

[23] P. A. Christiansen, Y. S. Lee, and K. S. Pitzer, J. Chem. Phys. **71**, 4445 (1979).

[24] D. R. Hamann, M. Schlüter, and C. Chiang, Phys. Rev. Lett. **43**, 1494 (1979).

[25] G. P. Kerker, J. Phys. C **13**, L189 (1980).

[26] G. B. Bachelet, D. R. Hamann, and M. Schlüter, Phys. Rev. B **26**, 4199 (1982).

[27] A modification has been proposed to alleviate the error due to the linearization of the exchange-correlation potential. See S. G. Louie, S. Froyen, and M. L. Cohen, Phys. Rev. B **26**, 1738 (1982).

[28] U. von Barth and C. D. Gelatt, Phys. Rev. B **21**, 2222 (1980).

[29] J. Ihm, A. Zunger, M. L. Cohen, J. Phys. C **12**, 4409 (1979).

[30] In reality, only finite number of l's are summed over. There is then a difference in choosing different forms for the local potential which also represent the potential for all larger l's. However, the difference is negligible as long as the nonlocal part contains $V^l(r)$ for all l's which are important.

Chapter III

Metal Hydrides

In this chapter, we present detailed electronic structure calculations and analyses of two light metal hydrides — a binary compound (magnesium hydride) and a ternary compound (lithium beryllium hydride). In Sec. 1, structural and electronic properties of magnesium hydride (MgH_2) are presented and discussed. The calculated properties include equilibrium lattice parameters, cohesive energy, selected elastic constants, bulk modulus, a zone-center phonon frequency, electronic band structure, and charge density distribution. Possible superconductivity by doping is proposed. The results on lithium beryllium hydride ($LiBeH_3$) are given in Sec. 2. The structure of $LiBeH_3$ is not yet known. Two perovskite structures are studied. Equilibrium lattice parameters and relative stability of the two structures are determined. The electronic band structures are calculated under normal and high-pressure conditions.

1. Magnesium Hydride

There have been many studies on metal hydride systems [1,2], stimulated by both the fundamental interests and various applications. Metal hydrides exhibit a number of interesting effects, among them is superconductivity [1]. Potential applications of metal hydrides include using them as storage media for hydrogen. Electronic structure studies of metal hydrides have concentrated on the transition metal hydrides and rare earth hydrides [3]. On the other hand, first-principles calculations of simple metal hydrides are rare. Magnesium hydride [4] is considered

one of the most important candidates for the reversible storage of hydrogen because of its high weight percentage of hydrogen. However, its usefulness is impeded by the slow rate of reaction and dissociation [4]. In order to improve on its performance, an understanding of the electronic and structural properties of magnesium hydride is essential.

A number of theoretical investigations on magnesium hydride have been reported. Lindner and Berggren [5] studied the stability of different structures using a nearly-free-electron model. The charge density distribution was investigated by Krasko [6] in which exchange-correlation effects are described within the density functional formalism. The method of solution to the Kohn-Sham equations (Eq. (2.4)), however, seems questionable since the calculated binding energy implied that MgH_2 cannot be formed from Mg metal and H_2 gas in contrast to experiments. Empirical pseudopotentials were used in both studies. In another work, Felsteiner *et al.* [7] used the orthogonalized-plane-wave (OPW) method and the linear combination of atomic orbitals (LCAO) method to calculate the Compton profile. There have been empirical arguments for covalent bonding in MgH_2. For instance, Stander and Pacey [8] performed a Born-Mayer type of calculation of the lattice energy of MgH_2 assuming that it is purely ionic. Their theoretical value was greater in magnitude than the experimental value by a sizeable amount. This difference was interpreted as evidence of an appreciable covalent contribution to the bonding in the crystal. The nature of electronic bonding is still not clear from the above mentioned work. Further results such as the band structure can enhance the understanding of the electronic properties.

In view of the above situation, we have performed a first-principles study on the electronic and structural properties of magnesium hydride [9]. The

pseudopotential approach [10] within the density functional formalism [11] is used. The calculated structural parameters and the cohesive energy are in better agreement with experiments than those of the previous calculations. We also investigated the bonding nature of MgH_2. Although the electrons are found to be localized around the H sites in general, the hydrogen ion is not H^-. There is appreciable amount of charge in the interstitial region. We found no evidence of covalent bond from the charge density distribution. Our results indicate that the Mg potentials have little effect on the dispersion of the valence bands. Based on our calculated band structure and charge density, we suggest that magnesium hydride doped with a monovalent element could be a superconductor. In the following, the calculational detail is first described. The calculated structural and electronic properties are then presented and discussed. Comparison with experimental results are made wherever they are available. The possible superconductivity in doped MgH_2 will be discussed.

1.1 Calculational Details

The calculation is based upon the pseudopotential method [10] within the density functional formalism [11]. The Wigner interpolation formula [12] is used for the correlation functional in this calculation. For comparison, other forms of exchange-correlation potential [13,14] are also used. The *ab initio* pseudopotentials are generated using the method of Hamann, Schlüter and Chiang [15]. The Mg potential is generated from the atomic configuration $(Mg)3s^1 3p^1$. In order to insure that the potentials accurately simulate the interaction between the core and valence electrons, calculations are done for several electronic (atomic and ionic) configurations of Mg atoms with the pseudopotentials (pseudoatom calculation).

The calculated eigenvalues and excitation energies are then compared with the results of all-electron calculations (Table I); there is good agreement between the two results. For hydrogen, only the s-potential is generated. Since there are no core electrons for hydrogen, the potential that the valence electron experiences should be strictly that of the proton. However, the pseudopotential and the protonic potential produce almost the same eigenenergy (total energy) since the potentials are appreciably different only near the nucleus. The difference between the total energies of the pseudoatom calculation and the all-electron calculation for H atom is less than 10^{-4} Ry with various forms of exchange and correlation, spin-polarized and non-spin-polarized.

The most convenient scheme for a crystal band structure calculation is to expand the wave functions in terms of plane waves [16]. This approach has proved to be very successful in the study of a wide variety of materials [17–22]. Due to the localized nature of the hydrogen $1s$ orbital, a large number of plane waves are required for the satisfactory convergence of the total energy. We choose a kinetic-energy cutoff of 30 Ry for calculation of all properties. This corresponds to about 1200 plane waves for the equilibrium lattice parameters. Extrapolation to infinite cutoff energy yielded a small decrease of 0.9 eV per unit cell (0.15 eV/atom) in the total energy. Diagonalization of the large Hamiltonian matrices is carried out using a block version of the 'residual minimization/direct inversion in the iterative subspace' method due to Bendt and Zunger [23].

The integrations over the Brillouin zone are performed using a uniform grid of k-points,

$$\mathbf{k} = \frac{l+s_1}{N_1}\mathbf{b}_1 + \frac{m+s_2}{N_2}\mathbf{b}_2 + \frac{n+s_3}{N_3}\mathbf{b}_3, \qquad (3.1)$$
$$l = 1,\ldots,N_1; \quad m = 1,\ldots,N_2; \quad n = 1,\ldots,N_3,$$

where $\mathbf{b}_1, \mathbf{b}_2, \mathbf{b}_3$ are primitive vectors in the reciprocal space. The values 0 and $\frac{1}{2}$ are often used for s_1, s_2, s_3 [24]. The k-points are mapped back to the irreducible part of the Brillouin zone (IBZ) using symmetry operations. For high-symmetry structures, a small set of special k-points [25] may be used. For the present work, we use a set of six k-points in the IBZ, which is equivalent to letting $N_1, N_2, N_3 = 4$ and $s_1, s_2, s_3 = \frac{1}{2}$. The special k-points should work relatively well for insulators, where there is no partial occupation of bands. The convergence with respect to the number of k-points is tested; the difference between the total energies calculated with the six special k-points and with 50 k-points over the IBZ generated by the uniform grid method is less than 1 mRy.

The calculation is done self-consistently; the solution is iterated until an accuracy of 10^{-4} Ry in the self-consistent potential is achieved. The corresponding tolerance of the total energy is less than 10^{-5} Ry.

1.2 Structural Properties

Lattice Parameters

Under ambient conditions, MgH_2 crystallizes in the tetragonal phase of the rutile type [26], which belongs to the space group $P4_2/mnm$ (D_{4h}^{14}). Fig. 1 shows the Mg and H atoms in the unit cell. The primitive cell contains two Mg atoms and four H atoms. The Mg atoms are located at the corner and the center of the cell. A parameter x describes the position of the four H atoms (Fig. 1). Each Mg atom is octahedrally coordinated to six H atoms and each H atom has three neighboring Mg atoms in the same plane. This structure has three independent structural and lattice parameters; they are a, c and x (or a, c/a, and x). The tetragonal structure is assumed in our calculations.

The total energy is calculated for different values of the three parameters. The calculated energies are fitted to the following quadratic expression,

$$\begin{aligned} E_{\rm tot} = E_0 &+ a_{11}(a-a_0)^2 + a_{22}(c-c_0)^2 + a_{33}(x-x_0)^2 \\ &+ a_{12}(a-a_0)(c-c_0) + a_{13}(a-a_0)(x-x_0) \\ &+ a_{23}(c-c_0)(x-x_0)\,. \end{aligned} \tag{3.2}$$

The equilibrium lattice parameters are found to be $a_0 = 8.604$, $c_0 = 5.747$ and $x_0 = 0.304$, where a_0 and c_0 are given in units of Bohr radius, a_B. The coefficients of the terms in Eq. (3.2) are determined to be

$$\begin{aligned} &a_{11} = 0.044, \qquad a_{22} = 0.042, \qquad a_{33} = 34.72, \\ &a_{12} = 0.035, \qquad a_{13} = -0.003, \qquad a_{23} = -0.460 \end{aligned} \tag{3.3}$$

in atomic units. We have calculated the total energy at 27 points in the neighborhood of the equilibrium parameters. The rms energy deviation of the fit from the calculated points is 5×10^{-5} Ry. Very similar results are obtained when c/a is treated as an independent variable instead of c in the quadratic fit. The equilibrium lattice parameters are compared with the experimental results in Table II. The differences with the experimental values are given in parentheses. Lindner and Berggren [5] have computed the equilibrium lattice parameters for alkaline-earth hydrides using empirical pseudopotentials and a nearly-free-electron approach. The stable structure of MgH_2 was predicted correctly. More recently, Krasko [6] used empirical pseudopotentials and an iteration-perturbation approach of covalent bonding to determine the equilibrium volume, fixing the parameters c/a and x to the experimental values. The results of these two calculations are also given in Table II. Our calculated structural and lattice parameters are in better

agreement with experiment [26]. The maximum difference is 2.2% between our calculated and the experimental unit cell volume.

For crystals with the rutile structure, each cation are surrounded by six anions forming an octahedron. This octahedron is irregular and the distances between the cation and the anions could take two values. If we demand these two separations to be equal, the parameter x is then related to c/a ratio by $x = \frac{1}{8}[2 + (c/a)^2]$. This is true to within about 1.5% for most crystals for which the x value is known (Table IV,3 of Ref. 27, except FeF_2). For MgH_2, the value of x calculated from the experimental c/a using the above expression is 0.306, which is the same as the experimental result. The experimental values of the c/a ratio of most crystals falls within the range of about 0.65 to 0.7. To correlate this with an approximate theoretical prediction, we can examine the variation of the Madelung energy with respect to c/a. Since the Madelung energy alone does not give a stable structure, we need to constrain the other parameters. From the above discussion, it seems reasonable to let the six nearest-neighbor Mg—H distances equal. Another reasonable constraint is to fix the unit cell volume. With these two conditions, we obtain an energy minimum at $c/a \simeq 0.67$. If we keep the nearest-neighbor Mg—H distances constant instead of the cell volume, the Madelung energy then minimizes at $c/a \simeq 0.71$. Thus the crude considerations of the Madelung energy seems to give the c/a ratios which coincide with the range of the experimental values. However, one should not conclude from the above results that these crystals are fully ionic.

Cohesive Energy

The cohesive energy is taken to be the difference between the total energy of the crystal and those of the isolated atoms. We performed a spin-polarized calculation for the H atom with the Ceperly-Alder exchange-correlation potential

as parametrized by Perdew and Zunger [14]. The calculated total energy of the H atom is −0.958 Ry. The total energy of the pseudo Mg atom is −1.688 Ry. The crystal energy calculated with the cutoff energy of 30 Ry is −8.209 Ry per unit cell. Hence the cohesive energy is 13.6 eV per unit cell. Taking into account the 0.9 eV decrease of the total energy of MgH_2 as the cutoff energy is extrapolated to infinity, the calculated cohesive energy becomes 14.5 eV per unit cell. This result does not include the vibrational energy of the solid. Since the Debye temperature for MgH_2 is fairly high, the zero point energy may not be neglected. At the present, there is no experimental value available for the complete phonon spectrum or the Debye temperature. Following Stander and Pacey [8], we use as the Debye frequency the maximum frequency at which the infrared absorption peak occurs, which is 3.48×10^{13} sec^{-1}. This corresponds to a Debye temperature, Θ_D, of 1670 K. The zero point energy is approximated by $\frac{9}{8}k_B\Theta_D$ per atom using the Debye model [28]. The corrected cohesive energy is 13.5 eV per unit cell. One may argue that the exact total energy of the H atom, −1.0 Ry, should be used. The cohesive energy will then be 11.2 eV per unit cell. If the Gunnarsson-Lundqvist-Wilkins expression [29] for the spin-polarized exchange and correlation potential is used, the total energy of the H atom is −0.984 Ry and the cohesive energy of MgH_2 is 12.1 eV per unit cell. We consider that the theoretical value for the cohesive energy ranges from 11.2 eV to 13.5 eV per unit cell. We evaluated the experimental cohesive energy from the heat of formation of magnesium hydride (0.70 eV/molecule), the cohesive energy of Mg solid (1.52 eV/atom), and the bonding energy of H_2 molecule (4.48 eV/molecule) [30]. The experimental cohesive energy is 13.4 eV per unit cell. The difference between our theoretical value and the experimental value ranges from ∼0.0 to 0.37 eV/atom. This difference is on the same order of magnitude as that obtained in other local density calculations for

metals [17,18]. We also calculated the total crystal energy at the above equilibrium parameters using different forms of exchange and correlation potential. The Hedin-Lundqvist [13] expression gives a cohesive energy greater than the result with Wigner interpolation formula by 0.14 eV/atom. The Ceperly-Alder form for the exchange and correlation as parametrized by Perdew and Zunger [14] gives almost the same cohesive energy as the Wigner interpolation formula.

Elastic Constants and Bulk Modulus

From the quadratic fit, Eq. (3.2), some elastic constants can be obtained. There are six nonvanishing elastic constants for a tetragonal crystal. Four of these, C_{11}, C_{12}, C_{13}, and C_{33}, are related to the variation of the parameters a and c. Since the strain e_1 is always equal to e_2 in our calculation, C_{11} is coupled to C_{12} and they cannot be determined individually. The potential energy density of the crystal under strains of e_1 $(=e_2)$ and e_3 is

$$U = \frac{1}{2}[2(C_{11} + C_{12})e_1e_1 + 4C_{13}e_1e_3 + C_{33}e_3e_3]. \tag{3.4}$$

Comparing this expression with the quadratic fit, we obtained the following values for the elastic constants.

$$C_{11} + C_{12} = 1.1, \qquad C_{13} = 0.3, \qquad \text{and} \qquad C_{33} = 1.0 \tag{3.5}$$

in units of 10^{12} dyn/cm^2. No experimental results are available to our knowledge. These elastic constants can be used to determine the bulk modulus. Assuming the c/a ratio is unchanged with volume, the strains e_1, e_2, and e_3 are equal. From the above equation for the energy density, it is readily shown that the bulk modulus is then given by

$$B_0 = \frac{1}{9}[2(C_{11} + C_{12}) + 4C_{13} + C_{33}]. \tag{3.6}$$

Substitution of the elastic constants (3.5) in the above equation gives $B_0 = 4.9 \times 10^{11}$ dyn/cm^2.

To make a more accurate determination of the bulk modulus and to also determine the pressure derivative of the bulk modulus, we calculated the total energy for larger volume variations. Because of the complexity of a full calculation, we fixed the two parameters x and c/a at their respective equilibrium values. The volume was allowed to vary within 10% of the equilibrium value. The calculated energy-versus-volume curve is plotted in Fig. 2. The squares are the calculated values and the solid line is the best fit to the Murnaghan equation of state [31] which assumes a linear pressure dependence of the bulk modulus,

$$E(V) = \frac{B_0 V}{B_0'(B_0'-1)}\left(B_0'\left(1-\frac{V_0}{V}\right)+\left(\frac{V_0}{V}\right)^{B_0'}-1\right)+E_0, \qquad (3.7)$$

where E is the energy and V is the volume. The root-mean-square difference between the fit and the calculated values is 2.5×10^{-5} Ry. From the fit, we obtain a bulk modulus, B_0, of 5.0×10^{11} dyn/cm^2. The pressure derivative of the bulk modulus, B_0', is found to be 4.9. This bulk modulus differs only by 2% from what we derived above from the elastic constants. The experimental value for the bulk modulus is not available for comparison. We note that our calculated bulk modulus is greater than that of the Mg metal (3.54×10^{11} dyn/cm^2). The addition of the H atoms thus increases the stiffness of the material.

We have not taken into account the effect of relaxing c/a and x in the above calculations of the bulk modulus. The relaxation of these two parameters would result in a smaller value. The change in the result can be estimated from Eq. (3.2). For a given hydrostatic pressure, the exact structural parameters are determined by requiring

$$\delta E + P\delta V = 0 \qquad (3.8)$$

for any variation of the parameters. The value of the parameters, and thus the crystal volume, are determined as a function of pressure. The bulk modulus is then derived from the linear relation between the volume and pressure. It is found to be 4.8×10^{11} dyn/cm^2. Thus the bulk modulus decreases by only 2% if the variations of the parameters c/a and x are taken into account.

Zone-Center Phonon

Since there are six atoms in the primitive cell, there are 15 optical phonon modes. There is one optical mode at the center of the Brillouin zone (Γ) which is consistent with the symmetry of the crystal. The optical mode Γ_1^+ involves the motion of the four hydrogen atoms in such a way that it corresponds to the oscillation of the parameter x; the unit cell and the crystal symmetry are unchanged. By displacing the four hydrogen ions up to 0.1 Å, the total energy is calculated as before. In the adiabatic (Born-Oppenheimer) approximation, the variation of the total energy is the potential energy for this mode of oscillation. The calculated phonon frequency is 3.81×10^{13} Hz by a quadratic least-squares fit. Similar values (within 2%) are also obtained from the fit, Eq. (3.2). No experimental value is available to our knowledge. However, our calculated frequency is comparable to the corresponding frequency in MgF_2, 12.7×10^{12} Hz (taken from Fig. 2 of Ref. 32), assuming the two frequencies are inversely proportional to the square root of the mass of the H and F atoms, respectively.

1.3 Electronic Properties

Band Structure and Density of States

The Brillouin zone of the tetragonal cell of MgH_2 is shown in Fig. 3. The symmetry points and symmetry lines are indicated. The calculated band structure

along several symmetry axes is shown in Fig. 4. In labelling the states, we have adopted the notations of Gay *et al.* [33]. The calculated density of states is shown in Fig. 5. The density of states was calculated from the computed eigenenergies at 50 k-points within the $\frac{1}{16}$ irreducible part of the Brillouin zone using the analytical linear tetrahedron method [34]. Four conduction bands are included in the density of states calculation. The energy reference for the band structure and density of states is arbitrary. Since the unit cell contains 8 valence electrons, the four valence bands are completely filled and the conduction bands are empty. Thus magnesium hydride is an insulator. An indirect gap is found for the present system. The minimum of the conduction band is along S at about 20% of the way from A_1 toward Z_1. The maximum of the valence band is not well distinguished. There are several maximum energies close to each other within the range of 0.1 eV along different symmetry axes. We find that the maximum energy is half way between Γ_4^+ and X_1 along Δ. These close maximum energies of the valence band result in high density of states and a sharp cutoff of the density of states at the valence band edge. The calculated energy gap is 3.06 eV. The calculated width of the valence band is 6.75 eV. The density of states curve exhibits two main peaks in the valence band. These two peaks comes from the states near A and R from the first two degenerate bands and the degenerate third and fourth bands, respectively. A UV-absorption experiment by Genossar [35] gives an absorption edge of 5.16 eV. Thus our calculated band gap is smaller than this experimental value by 2.1 eV. This underestimation of the band gap by about 40% is typical of the calculations for semiconductors and insulators using the local-density theory [36].

It is interesting to investigate how the electronic structure depends on the potentials of the two types of atoms. A hypothetical system in which the H

atoms are located as in MgH_2 but the Mg atoms are removed was examined. Self-consistent calculation was repeated, the band structure was obtained and is shown in Fig. 6. We see that the four lowest bands resemble very much those calculated for MgH_2 (Fig. 4). This indicates that the Mg atoms are not very influential on the valence bands of MgH_2. Quantitative differences do exist. The bottom four bands span an energy range of 5.78 eV, which is slightly smaller than the width of the valence band of MgH_2 (6.75 eV). This difference could be due to the contribution of the Mg potentials to the energy overlap integrals in part and also the larger electron-electron Coulomb repulsion in MgH_2 because there are twice as many electrons in MgH_2 than in this hypothetical H crystal. The most significant difference between this hypothetical system and MgH_2 is in the fifth band where the state Γ and the states near A becomes almost equal in energy. The "energy gap" increases to 5.0 eV compared to 3.06 eV calculated for MgH_2. We expect the conduction band level (and thus the band gap) to be sensitive to the presence (or absence) of the Mg potentials. The wave function of the state at the conduction-band edge near the symmetry point A has a large probability distribution around the Mg atoms.

From the variation of the bands with k-vector, we could roughly separate the valence bands into two different regimes. Fig. 4 shows that the bottom of the valence bands is free-electron-like. In fact, by fitting the eigenenergies to a quadratic dispersion, we obtain a fairly isotropic effective mass at Γ of about 1.1 times the free-electron mass. This effective mass can be understood from the $\mathbf{k}\cdot\mathbf{p}$ perturbation theory, in which the inverse effective mass tensor of the n-th band at $\mathbf{k}_0$ is given by [37] (in Rydberg atomic units),

$$\left(\frac{1}{m^*}\right)_{\alpha\beta} = \delta_{\alpha\beta} + 2\sum_j{}' \frac{(p^\alpha_{nj}p^\beta_{jn} + p^\beta_{nj}p^\alpha_{jn})}{E_n(\mathbf{k}_0) - E_j(\mathbf{k}_0)}, \tag{3.9}$$

where the prime means the exclusion of the term $j = n$ in the sum and p^{α}_{nj} is the α-th component of the vector

$$\mathbf{p}_{nj} = \int \psi^{*}_{n}(\mathbf{k}_0, \mathbf{r})(-i\nabla)\psi_j(\mathbf{k}_0, \mathbf{r})\, d\mathbf{r}. \tag{3.10}$$

In the present case, $n = 1$ and $\mathbf{k} = 0$. The non-diagonal elements of the inverse mass tensor vanish identically due to the symmetry of the crystal; there is a mirror symmetry which takes $k_x \rightarrow -k_x$ and there is a 90° rotation which takes $k_x \rightarrow k_y$, and $k_y \rightarrow -k_x$. The latter also requires that $m_{11} = m_{22}$. According to our angular momentum decomposition, all states at Γ shown in Fig. 4 are symmetric with respect to the reflection about the xy plane. The z-component of the momentum matrix elements, $\mathbf{p}_{1j}$, vanishes. Thus m_{33} is simply the electron mass, neglecting high-lying bands. Symmetry considerations also limit the non-vanishing x-component of Eq. (3.10) to the element between the first state (Γ_1^+) and the doubly degenerate Γ_5^+ states among all those in Fig. 4. The (negative) correction to the inverse effective mass is very small (less than 1%). The correction due to higher bands is likely to be a few percent. By inverting the effective mass tensor, we should obtain an effective mass tensor with the diagonal terms greater than but close to the free electron mass.

The upper part of the valence bands is very narrow. Examination of the wave functions shows that the states are fairly localized on the H atoms. One would thus expect to use a simple tight-binding model to describe the bands. We have attempted this by including only the s-like orbitals on the H sites and five different overlap integrals. Although the general features of most part of the bands are reproduced, there are some basic differences. Felsteiner *et al.* [7] fitted the Compton profile with a LCAO calculation. They found that the calculated Compton profile did not converge until the overlaps of 162 ions were considered.

Charge Distribution and Bonding

The valence charge density is obtained directly from the self-consistent calculation. Two contour plots of the valence charge distributions in the (001) plane (perpendicular to the c axis) and in the (110) plane (parallel to the c axis), are shown in Fig. 7. Both planes include the nearest-neighbor Mg—H bonds, with slightly different bond distances. The contour lines are in intervals of 5.0 electrons per unit cell volume. The average charge density is 8 electrons per unit cell volume. The charge density plots show the ionic character of the crystal, the charges are localized around the hydrogen sites in both projections. The highest charge density is 95.0 electrons per unit cell volume at the hydrogen sites. Following the common practice with ionic crystals, we can assign ionic radii to Mg and H ions assuming the nearest neighbor ions are in contact with each other. In our case, the ionic radius of H is determined by the nearest neighbor H—H distance and the radius of Mg is determined by the nearest neighbor Mg—H distance. We then obtain a radius of 1.26 Å for the H ions and 0.69 Å for the Mg ions. To estimate how ionic the crystal is, we calculated the valence charges within the spheres of ionic radii. We find 0.05 electrons around the Mg ions and 1.6 electrons around each H ion. Ionic charges obtained by Krasko [6] are similar to our result. Since the valence electrons of Mg decreased to 0.05 from the atomic value of 2.0, Mg can be considered to be in the form of Mg^{++}. However, the H ions do not acquire ionic charge close to -1 and there is about 1.5 electrons per unit cell (19% of the total number of valence electrons) in the interstitial region. The crystal as a whole should not be taken as purely ionic. A covalent bond is normally reflected by some closed contour between the atoms. We have made contour plots with smaller increment (1.0). No closed contour lines between the nearest-neighbor H

and Mg sites were observed. The covalent bonding that was presumed to exist [2,8] may thus be negligible in this crystal. The ionic radius of H ion we obtained above is 1.26 Å, which is different from 2.08 Å, the value given by Pauling [38] for H^- while the radius of Mg^{++} (0.69 Å) is close to Pauling's value (0.65 Å). The difference between Pauling's radius for H^- and the smaller value of the H ion in the present system is compatible with the charge of the H ions. The hydrogens in this crystal are not H^- but approximately $H^{-0.6}$.

1.4 Superconductivity

Based on our calculations of the band structure and the charge density, we suggest that magnesium hydride substitutionally doped with a monovalent element could become a superconductor. This conclusion is drawn from the following observations:

(1) The valence band of magnesium hydride is determined predominantly by the H—H interaction, the cation has very little influence on the valence band structure (see Fig. 4 and 6). To the first order of approximation, a rigid band model is valid. Hence, magnesium hydride can be made metallic if it is doped substitutionally with a monovalent element. The carriers will be of the hole type.

(2) The Fermi level will be right below the valence-band edge for this doped magnesium hydride, where the density of states is high (See Fig. 5).

(3) The orbitals of the carrier will be mainly of the character of hydrogen orbital. That is, the carrier will interact strongly with the hydrogen potential.

There exist metal hydride systems which are superconductors, a noted example is PdH_x ($x \simeq 0.8$) with $T_c \simeq 9$ K [1]. In this case, the superconductivity is believed to arise from the coupling of electrons with the hydrogen optical mode.

Superconductivity also correlates with the density of hydrogen states at the Fermi level. One of the reasons that T_c is only 9 K for PdH_x could be that the electronic structure of PdH_x is dominated by the Pd states and the hydrogen exerts only a small effect on the band structure. The electronic structure of magnesium hydride, on the other hand, is dominated by hydrogen. One may think of magnesium hydride as a metallic hydrogen system which is stabilized by magnesium. However, magnesium hydride is not metallic. By doping it with a monovalent element, we are compromising between metallic behavior and stability.

What should we dope MgH_2 with? Lithium seems to be a good candidate because Li^+ has a similar size as Mg^{++} (ionic radius of Li^+ is 0.68 Å [39]). It is not certain that magnesium hydride can be doped sufficiently for superconductivity and yet remain structurally stable in the rutile structure. However, hydrides of $Mg_{0.8}Li_{0.1}X_{0.1}$ (X = Ni, Zn, Sn, Si, Cu) alloys have been reported in connection with a hydrogen storage study [40]. No conductivity measurements nor structural analyses were reported for these alloys. How much lithium is needed? It is difficult to predict the optimal dopant level. If we draw a comparison with the oxide superconductors, we would estimate a dopant level of 10 to 20%. Since MgH_2 is an ionic system, charge compensation implies that there will be hydrogen vacancies. It may be necessary to anneal the sample under a hydrogen atmosphere.

2. Lithium Beryllium Hydride

The idea of metallic hydrogen being a high-temperature superconductor has attracted much interest [41,42]. The realization of metallic hydrogen via pressurization has not been possible because of the extremely high pressures necessary [43]. Extensive work have been done on incorporating hydrogen in

transition metals to achieve high superconducting transition temperature (T_c) [44]. Thus far, the highest T_c in metal hydrides is below 20 K in these systems [44]. This is far below the anticipated T_c of solid atomic hydrogen [42] ($\sim$ 250 K). One of the reasons for the low value of T_c in the transition metal hydrides could be that the electronic states at the Fermi level are not strongly interacting with the hydrogens. This idea has lead to the recent proposals [9,45] that light metal hydrides may be better candidates for superconductivity study, since the states at the Fermi energy interact strongly with the hydrogen in these materials.

However, the light metal hydrides are usually ionic or covalent in character and are insulators. Doping would be one way to induce metallic behavior [9]. There may also be (complex) light metal hydrides that are intrinsically metallic. Overhauser [45] suggested that lithium beryllium hydride may be a metal with a valence-electron density close to that of metallic hydrogen and a good candidate for a high-temperature superconductor. By analyzing the X-ray diffraction data of Bell and Coates [46], Overhauser [45] proposed tentative structures for $LiBeH_3$ and Li_2BeH_4. We will concentrate only on $LiBeH_3$. From the powder diffraction lines, Overhauser deduced that $LiBeH_3$ has a face-centered cubic structure with a lattice constant of 5.09 Å. After unsuccessful attempt to come up with a cubic unit cell which contains four formula units, Overhauser proposed that the cubic unit cell contains eight formula units, specifically, eight small cubes of the perovskite-type (H at face centers and Li and Be at cube center and corner). The Li and Be are, however, placed alternately at the corner sites and at the center sites. The rationalization of such a structure requires strong metallic bonding, as argued by Overhauser. This possible metallic behavior has not been examined experimentally because only powdered samples have been prepared so far [47].

In taking the first step toward understanding this system, we have performed first-principles total energy and electronic band structure calculations on $LiBeH_3$ in two structures of the perovskite type. In the first structure (Fig. 8(a)), the Be is located at the center site (with 6 H-coordination) and Li at the corner site (with 12 H-coordination). In the second structure (Fig. 8(b)), the positions of Be and Li are interchanged (this is also called an inverse perovskite structure). The hydrogens reside at the face centers in both cases. We shall refer to the first structure as I and the second as II. The structure proposed by Overhauser [45] can be considered as a "mixture" of I and II. We have determined the equilibrium lattice parameters for both structures. According to the energy band structure obtained, I is a semiconductor while II is a metal. Unfortunately, I is more stable than II. We also find that the calculated valence electron density under ambient pressure is about half of that suggested by Overhauser. Metallization of the systems under external pressure is also investigated.

2.1 Calculational Details

We use the Hedin-Lundqvist formula [13] for the exchange-correlation potential. The pseudopotentials of Li, Be, and H are generated in the configurations (Li)$2s^{0.5}2p^{0.5}$, (Be)$2s^12p^1$, and H$1s^{0.5}$, respectively. Partial core corrections [48] are used, which increases the transferability of the pseudopotentials. The potentials are tested against all-electron results for atoms and ions. The basis for solving the Schrödinger equation consists of plane waves which satisfy $(\mathbf{k}+\mathbf{G})^2 \leq E_{\max}$. We choose $E_{\max} = 30$ Ry. The dimension of the Hamiltonian matrices is approximately 600×600. Previous work [9] on magnesium hydride using the same $E_{\max}$ yielded results which agree well with available experimental results. Four

special k-points [25] are used in obtaining the self-consistent charge density in the calculations for both structures.

2.2 Equilibrium Properties

Structural Properties

The total energy of the two structures, I and II, were calculated for different values of the lattice constant a. The calculated equilibrium lattice constants, cohesive energy, the bulk modulus, and its pressure derivative for both structures are listed in Table IV. These parameters are determined by fitting the calculated energies with the Murnaghan equation of state (Eq. (3.5)). The cohesive energy is defined as the difference between the total energy of the crystal and that of the individual atoms. The energies of H and Li atoms are obtained from the spin-polarized calculations using the Ceperly-Alder correlation potential as parametrized by Perdew and Zunger [14]. Comparison of the cohesive energy shows that I is more stable. The energy difference between the two structures at their calculated equilibrium lattice constants is 0.77 eV/atom. We may attempt to interpret this energy difference in terms of the difference in Madelung energy (i.e., the interaction energy between the ions). Assuming full ionic charges at the sites, the difference in Madelung energy is 1.1 eV/atom, which is only 0.3 eV/atom greater than the calculated total-energy difference.

Electronic Properties

The calculated band structure of I at the equilibrium volume is shown in Fig. 9. The bands are labelled according to the notations of Bouckaert, Smoluchowski, and Wigner [49]. There is no overlap between the third and fourth bands; this system is insulating because the electrons fill up the three valence

bands. The band structure has an indirect gap from the valence band edge, X_2, to the conduction band edge, R_1. This band gap is fairly small (0.8 eV), indicating a low ionicity for the material. The density functional theory, however, underestimates the energy gaps of semiconductors by about 50% [36]. We thus expect the actual energy gap to be about 1.6 eV. The valence band width is found to be 11.2 eV.

When the positions of Li and Be atoms are switched, we find a metallic phase. The electronic band structure of II at the calculated equilibrium lattice constant is shown in Fig. 10. Comparing with the band structure of I (Fig. 9), it is seen that the metallic behavior comes from the lowering of the conduction band state M_3. The energy overlap from M_3 to X_2 is 3.2 eV. The Fermi level is at about 8.06 eV which corresponds to an occupied bandwidth of 9.9 eV. The Fermi surface intersects with the second, third, and fourth band. Except for a small and nearly spherical hole pocket around the zone center Γ, the second band is completely filled, thus this band will contribute little to the metallic property. The metallic behavior will be determined mainly by the third and fourth band. We note that the triply degenerate R'_{25} state is very close to the Fermi energy; it is 0.14 eV above the Fermi energy. The exact value should not be taken too seriously since our calculation uses the four special k-point summation for the charge density. In Fig. 11, the density of states for II is shown. The density of states at the Fermi energy is approximately 0.75 states/eV per unit cell.

It is worthwhile to understand the character of the states at M and R since they are responsible for the conversion from an insulator (I) to a metal (II). We have performed angular momentum decompositions of the wave functions [17] around the different atoms. We found that the wave function of the M_3 state is

mainly s-character at the corner site, viz., Li in I and Be in II, and p-character around the hydrogens. This explains why the band overlap occurs in II. Since the Be pseudopotential is much more attractive than the Li pseudopotential, the energy of the M_3 state is lower when Be is at the cube corner. The triply degenerate R'_{25} state is mainly p-character at the corner and face-center sites. Again the energy is lower when Be is located at the corner.

Although the I structure is an insulator, there is still a fair amount of hybridization of the Be-2s states with the hydrogen states in the valence bands. The hybridization is illustrated by the M_1 state. Angular momentum decomposition shows a large s-component around the center site in this state. The change of the occupation of the center site by Be to that by Li results in the upward shift of the energy (Fig. 9 to Fig. 10). This shift is actually responsible for the dip in the density of state of II slightly below 5.0 eV, which is absent in the density of states of I. Another example is offered by the X_1 state, which is also shifted upward as Be is replaced by Li (from I to II). Unlike Be, Li has little effect on the valence band states of the perovskite structure (I).

2.3 Pressurization

From the above result, the more stable of the two structures is an insulating one (I). Assuming that the two perovskite structures in Fig. 8 are relevant to the real crystal, it is of practical interest to investigate whether a metallic phase exist under external pressure. From our structural parameters listed in Table IV, a pressure-induced phase transition between I and II is not likely to occur at any presently realizable pressure. We examine instead the possibility of pressure-induced metallization of the insulating structure (I). We calculate the

band structure at a = 3.07 Å, which corresponds to 94 kbar according to the Murnaghan equation of state [31] and the parameters listed in Table IV. The band gap in I is found to increase to 1.1 eV. If this trend continues at higher pressure, the structure would not metallize. The calculations at 94 kbar, however, does not apply to higher pressure. The increase in the band gap at low pressure is because the R_1 state, which is the conduction band edge at zero pressure (Fig. 9), moves up. On the other hand, the R'_{25} state comes down with the increase of pressure. At a lattice constant of 2.72 Å (62% of equilibrium volume), which corresponds to a pressure of about 0.7 Mbar, we find that band-overlap occurs. The R'_{25} state is lowered in energy to ~0.2 eV below that of the X_2 state. Another calculation is done for the unit cell volume being half of the normal value (which corresponds to a pressure of ~1.5 Mbar). The band-overlap increases from 0.2 eV to 1.4 eV. The density of states at the Fermi level is on the order of 0.1 states/eV per unit cell. We should mention that the calculated pressure at small volumes using the Murnaghan equation of state depends strongly on the value of B'_0. An increase in B'_0 by 20% could change the pressure to 0.8 Mbar at 62% of equilibrium volume and to 1.9 Mbar at 50% of the equilibrium volume.

2.4 Discussions and Conclusions

From the results of our calculation, the structure proposed by Overhauser [45] is incorrect for two reasons. First, we found that the perovskite structure (I) is far more stable than the inverse perovskite structure (II). In the structure proposed by Overhauser [45] for $LiBeH_3$, the Li and Be are alternately placed at the body centers and at the corners of the cubic unit cells. Such an arrangement is not stable compared to the perovskite structure (I). Second, our calculated equilibrium lattice

constants of I and II are approximately the same (about 3.18 Å). The valence electron density calculated from this lattice constant is $\sim 1.85 \times 10^{23}$ cm^{-3}. Since the proposed structure of Overhauser is a "mixture" of I and II, its valence charge density should be close to this value. However, his proposed structure has a valence charge density of 3.64×10^{23} cm^{-3}. We thus conclude that its density is too high, and hence his proposed structure is not correct.

The bonding in the materials is mainly ionic, although Be orbitals hybridize with H-1s orbital. Thus the perovskite is more stable than the inverse perovskite structure since the former has a lower Madelung energy. The real structure is likely to have still lower Madelung energy.

The stable perovskite structure is found to be insulating. If high pressure is applied, the crystal can metallize. However, the density of states at the Fermi level is small. In view of this, other mechanisms may be preferred to induce a metallic phase. For example, it might be possible to put in an unequal amount of Li and Be in the crystal, that is, to make $Li_{1-x}Be_{1+x}H_3$ with $x > 0$. This may force some of the Be to occupy the corner sites and thus bring down the M_3 state, thereby inducing the overlap between the conduction and valence bands.

References for Chapter III

[1] *Electronic Structure and Properties of Hydrogen in Metals*, edited by P. Jena and C. B. Satterthwaite (Plenum, New York, 1983).

[2] T. R. P. Gibb, in *Progress in Inorganic Chemistry*, edited by F. A. Cotton (Interscience, New York, 1962), Vol. 3, p. 315.

[3] M. Gupta, in *The Electronic Structure of Complex Systems*, edited by P. Phariseau and W. M. Tammerman (Plenum, New York, 1984), p. 243.

[4] P. Selvam, B. Viswanathan, C. S. Swamy, and V. Srinivasan, Int. J. Hydrogen Energy **11**, 169 (1986).

[5] P. Lindner and K.-F. Berggren, Int. J. Quantum Chem. **7**, 667 (1973).

[6] G. Krasko, in *Metal-Hydrogen Systems*, edited by T. Nejat Veziroglu (Pergamon, New York, 1982), p. 367.

[7] J. Felsteiner, M. Heilper, I. Gertner, A. C. Tanner, R. Opher, and K.-F. Berggren, Phys. Rev. B **23**, 5156 (1981).

[8] C. M. Stander and R. A. Pacey, J. Phys. Chem. Solids **39**, 829 (1978).

[9] R. Yu and P. K. Lam, Phys. Rev. B **37**, 8730 (1988).

[10] M. L. Cohen and V. Heine, in *Solid State Physics*, edited by H. Ehrenreich, F. Seitz, and D. Turnbull (Academic, New York, 1970), Vol. 24, p. 37.

[11] P. Hohenberg and W. Kohn, Phys. Rev. **136**, B864 (1964); W. Kohn and L. J. Sham, *ibid.* **140**, A1133 (1965).

[12] E. Wigner, Phys. Rev. B **23**, 5048 (1981).

[13] L. Hedin and B. I. Lundqvist, J. Phys. C **4**, 2064 (1971).

[14] D. M. Ceperly and B. J. Alder, Phys. Rev. Lett. **45**, 566 (1980); J. P. Perdew and A. Zunger, Phys. Rev. B **23**, 5048 (1981).

[15] D. R. Hamann, M. Schlüter, and C. Chiang, Phys. Rev. Lett. **43**, 1494 (1979).

[16] J. Ihm, A. Zunger, and M. L. Cohen, J. Phys. C **12**, 4409 (1979).

[17] P. K. Lam and M. L. Cohen, Phys. Rev. B **24**, 4228 (1981); **27**, 5986 (1983).

[18] M. Y. Chou, P. K. Lam, and M. L. Cohen, Phys. Rev. B **28**, 4179 (1983).

[19] M. T. Yin and M. L. Cohen, Phys. Rev. Lett. **45**, 1004 (1980).

[20] J. Ihm and J. D. Joannopoulos, Phys. Rev. B **24**, 4191 (1981).

[21] S. Froyen and M. L. Cohen, Phys. Rev. B **26**, 3770 (1981).

[22] K. J. Chang and M. L. Cohen, Phys. Rev. B **30**, 4774 (1984).

[23] See D. M. Wood and A. Zunger, J. Phys. A **18**, 1343 (1985).

[24] H. J. Monkhorst and J. D. Pack, Phys. Rev. B **13**, 5188 (1976); J. D. Pack and H. J. Monkhorst, Phys. Rev. B **16**, 1748 (1977).

[25] D. J. Chadi and M. L. Cohen, Phys. Rev. B **8**, 5747 (1973).

[26] F. H. Ellinger, C. R. Holley, Jr., B. B. McInteer, D. Pavone, R. M. Potter, E. Staritzsky, and W. H. Zachariasen, J. Am. Chem. Soc. **77**, 2647 (1955).

[27] R. W. G. Wyckoff, *Crystal Structures*, 2nd ed. (Interscience, New York, 1963), Vol. 1, p. 250.

[28] M. Born and K. Huang, *Dynamical Theory of Crystal Lattices* (Oxford University, London, 1956).

[29] O. Gunnarsson, B. I. Lundqvist, and J. W. Wilkins, Phys. Rev. B **12**, 1257 (1975).

[30] *Handbook of Chemistry and Physics*, 66th ed. (CRC Press, Boca Raton, Florida, 1985).

[31] F. D. Murnaghan, Proc. Natl. Acad. Sci. USA **30**, 244 (1944); O. L. Anderson, J. Phys. Chem. Solids **27**, 547 (1966).

[32] R. Almairac, J. L. Sauvajol, C. Benoit, and A. M. Bon, J. Phys. C **11**, 3157 (1978).

[33] J. G. Gay, W. A. Albers, Jr., and F. J. Arlinghaus, J. Phys. Chem. Solids **29**, 1449 (1968).

[34] G. Lehmann and M. Taut, Phys. Stat. Sol. (b) **54**, 469 (1972).

[35] J. Genossar, quoted in Ref. 6.

[36] M. S. Hybertsen and S. G. Louie, Phys. Rev. Lett. **55**, 1418 (1985).

[37] See, for example, J. Callaway, *Energy Band Theory* (Academic, New York, 1964).

[38] L. Pauling, *The Nature of the Chemical Bond*, 2nd ed. (Cornell University, Ithaca, New York, 1942).

[39] C. Kittel, *Introduction to Solid State Physics*, 6th ed. (Wiley, New York, 1986), p. 76.

[40] J. F. Nachman and D. A. Rohy, in *Metal-Hydrogen Systems*, edited by T. N. Veziroglu (Pergamon, New York, 1982), p. 557.

[41] N. W. Ashcroft, Phys. Rev. Lett. **21**,1748 (1968).

[42] T. Schneider, Helv. Phys. Acta **42**, 957 (1969); A. C. Switendick, in *Superconductivity in d- and f-Band Metals*, edited by D. H. Douglass (Plenum, New York, 1976), p. 593; D. A. Papaconstantopoulos, L. L. Boyer, B. M. Klein, A. R. Williams, V. L. Morruzzi, and J. F. Janak, Phys. Rev. B **15**, 4221 (1977); D. A. Papaconstantopoulos and B. Klein, Ferroelectrics **16**, 307 (1977).

[43] Attempts have been made to achieve metallic hydrogen by applying pressure in excess of 1 Mbar. See H. Shimizu, E. M. Brady, E. K. Mao, and P. M. Bell, Phys. Rev. Lett. **47**, 128 (1981); K. H. Weil and V. Nardi, Int. J. Hydrogen Energy **10**, 859 (1985). For recent theoretical predictions of phase transitions

of solid hydrogen, see B. I. Min, H. J. F. Jansen, and A. J. Freeman, Phys. Rev. B **33**, 6383 (1986); T. W. Barbee, A. Garcia, and M. L. Cohen, Phys. Rev. Lett. **62**, 1150 (1989).

[44] B. Stritzker, in *Electronic Structure and Properties of Hydrogen in Metals*, edited by P. Jena and C. B. Satterthwaite (Plenum, New York, 1983), p. 309. A $T_c \sim 17$ K can be achieved in hydrides of Pd-Cu alloys.

[45] A. W. Overhauser, Phys. Rev. B **35**, 411 (1987).

[46] N. A. Bell and G. E. Coates, J. Chem. Soc. A **1968**, 628 (1968).

[47] A. W. Overhauser, Int. J. Mod. Phys. B **1**, 279 (1987).

[48] S. G. Louie, S. Froyen, and M. L. Cohen, Phys. Rev. B **26**, 1738 (1982).

[49] L. P. Bouckaert, R. Smoluchowski, and E. Wigner, Phys. Rev. **50**, 58 (1936).

Table I. The pseudoatom eigenvalues and excitation energies for different electronic configuations of the Mg atom and the deviations (in parentheses) from the corresponding all-electron values. Pseudopotentials are generated with $r_c(s) = 1.6$ a.u. and $r_c(p) = 2.0$ a.u. using Wigner correlation. No core correction is used.

	Eigenvalues (Ry)		Excitation Energy (Ry)
Configuration	s	p	
$3s^2 3p^0$	−0.3600	−0.1119	0.0
	(−0.0014)	(0.0003)	(0.0)
$3s^1 3p^1$	−0.4304	−0.1671	0.2556
	(0.0000)	(0.0001)	(0.0010)
$3s^0 3p^2$	−0.4835	−0.2083	0.5254
	(0.0038)	(0.0006)	(−0.0002)
$3s^1 3p^0$	−0.8492	−0.5338	0.5992
	(0.0025)	(0.0017)	(0.0004)
$3s^{0.5} 3p^0$	−1.1025	−0.7611	1.0877
	(0.0135)	(0.0083)	(−0.0031)

Table II. Calculated and experimental structural properties and cohesive energy of MgH2. Differences are given in parentheses. Length is in units of Bohr radius and cohesive energy in eV per unit cell.

	Experiment	Calculation		
		Present work	Lindner *et al.* (1973)	Krasko (1982)
x	0.306[a]	0.304 (+0.002)	0.306 (0.0)	
a	8.536[a]	8.604 (+0.068)	8.62 (+0.084)	8.746 (+0.21)
c	5.709[a]	5.747 (+0.038)	6.18 (+0.471)	
c/a	0.669	0.668 (−0.001)	0.717 (+0.048)	
Cell Volume	416.0	425.5 (+9.5)	459.2 (+43.2)	447.5 (+31.5)
Cohesive Energy	13.4[b]	11.2 — 13.5[b] (−2.2 — +0.1)		6.4 (−7.0)

[a]Ellinger *et al.* (1955). [b]See text.

Table III. Calculated elastic constants, bulk modulus, pressure derivative of the bulk modulus, and frequency of a zone-center optical mode of MgH_2. No experimental values exist for comparison. The elastic constants and the bulk modulus are in units of 10^{12} dyn/cm^2. The phonon frequency is in units of 10^{13} Hz.

$C_{11}+C_{12}$	1.1	Bulk modulus B_0	0.50
C_{13}	0.3	B_0'	4.9
C_{33}	1.0	Γ_1^+ optical mode	3.81

Table IV. Calculated equilibrium lattice constant, cohesive energy, bulk modulus, and its pressure derivative for the two assumed perovskite structures of $LiBeH_3$.

	a (Å)	Cohesive energy (eV/atom)	B_0 (Mbar)	B_0'
I	3.19	2.84	0.69	2.8
II	3.18	2.07	0.60	3.2

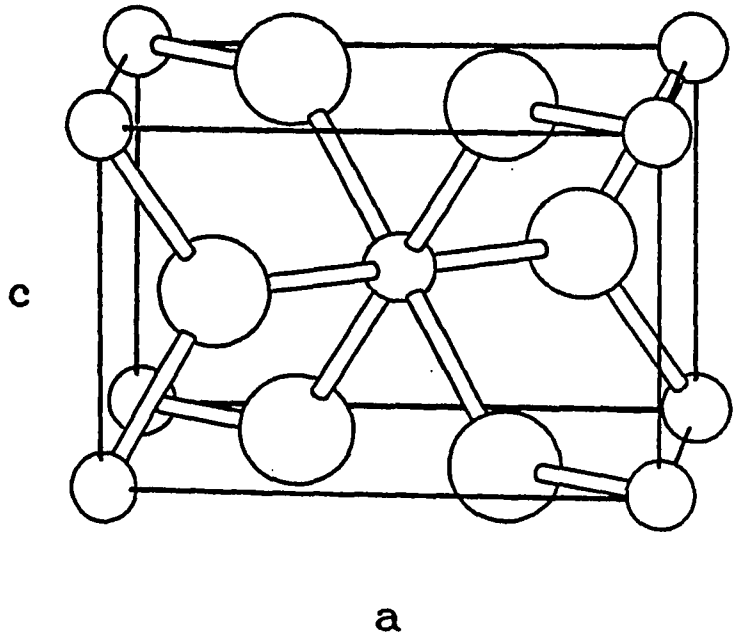

Fig. 1. The rutile type tetragonal unit cell of MgH_2. The small spheres are Mg atoms and the large spheres H atoms. Two Mg atoms are located at $(0,0,0)$ and $(\frac{1}{2},\frac{1}{2},\frac{1}{2})$ and four H atoms are located at $(x,x,0)$, $(1-x,1-x,0)$, $(\frac{1}{2}+x,\frac{1}{2}-x,\frac{1}{2})$ and $(\frac{1}{2}-x,\frac{1}{2}+x,\frac{1}{2})$ in units of the lattice constants.

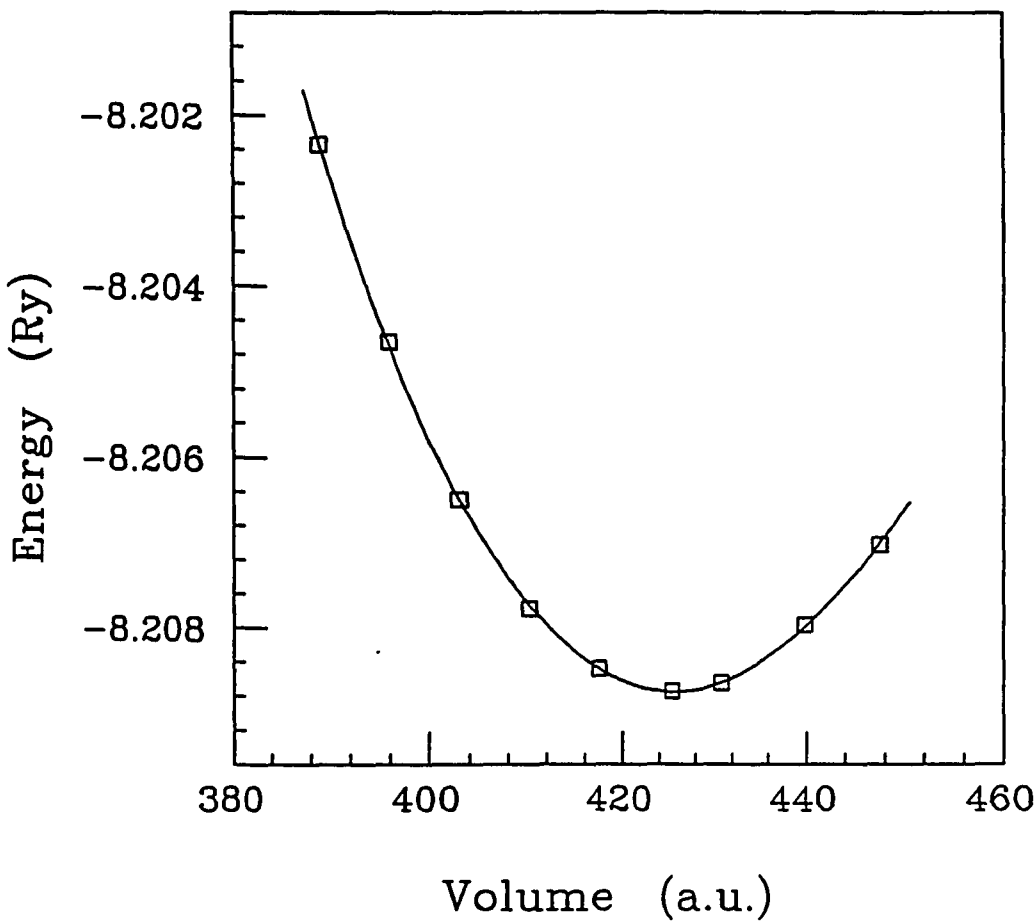

Fig. 2. The total energy of MgH_2 at different unit cell volumes. The parameters c/a and x are fixed at their respective equilibrium values. The squares are the calculated values, and the curve is a fit to the Murnaghan equation of state.

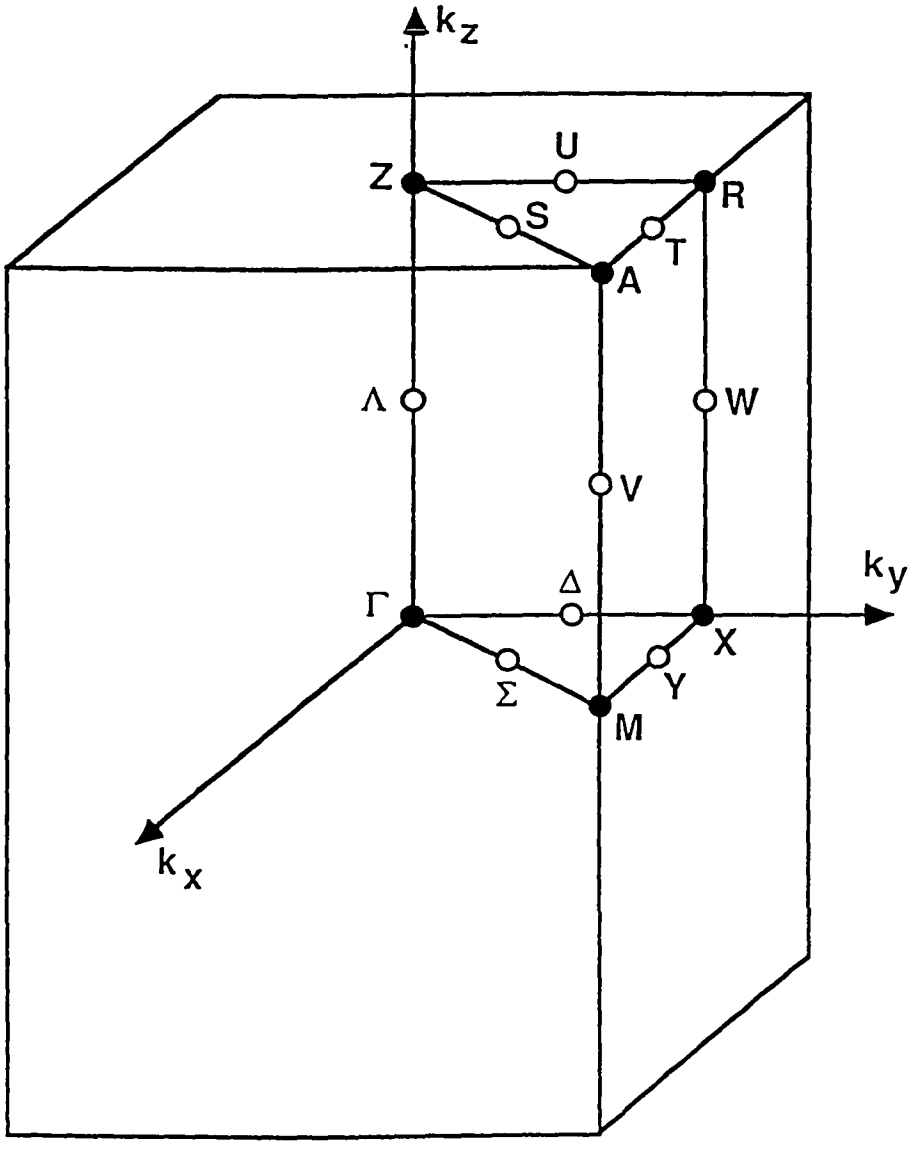

Fig. 3. Brillouin zone of the tetragonal structure of the rutile type (space group $P4_2/mnm$) and its symmetry points and lines.

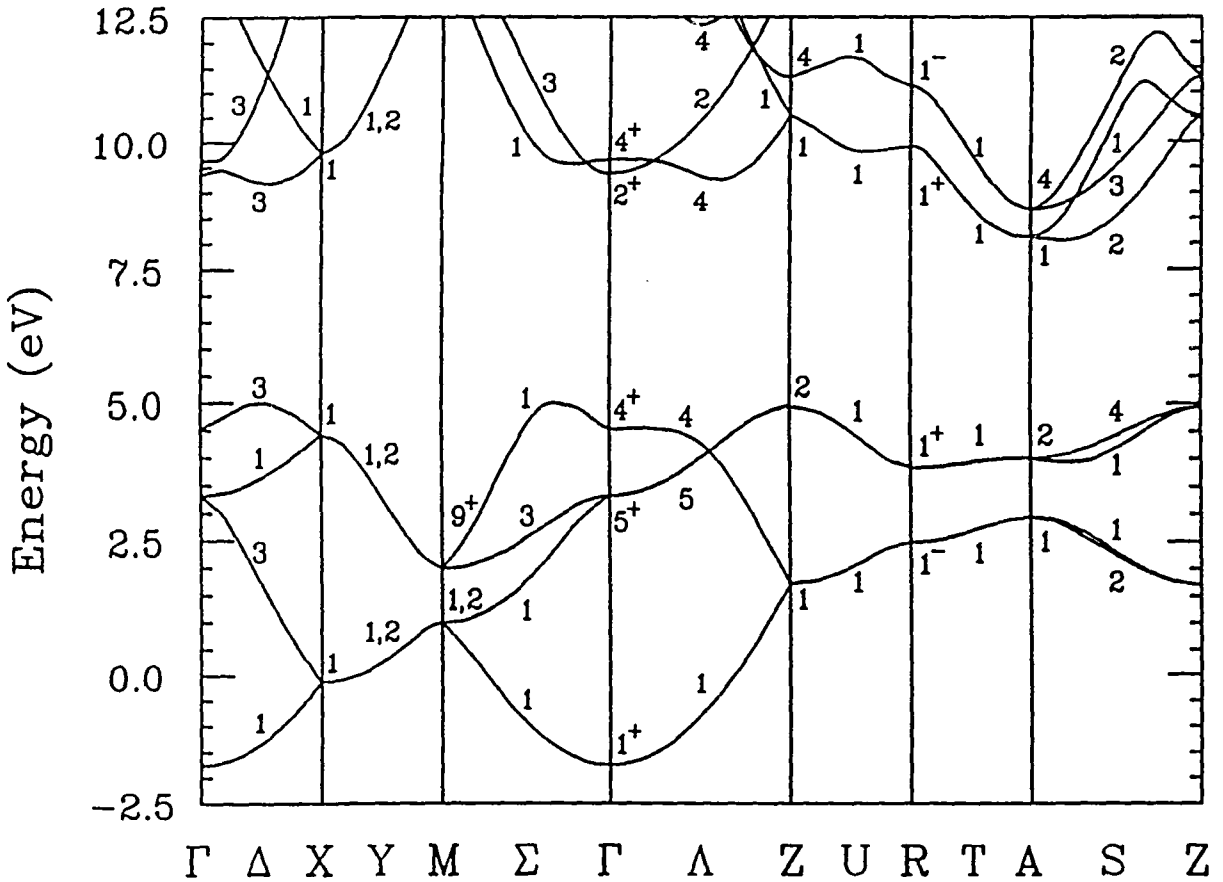

Fig. 4. Calculated electronic band structure of MgH_2 plotted along several high-symmetry directions. Symmetry labelling of Gay *et al.* (1968) is used.

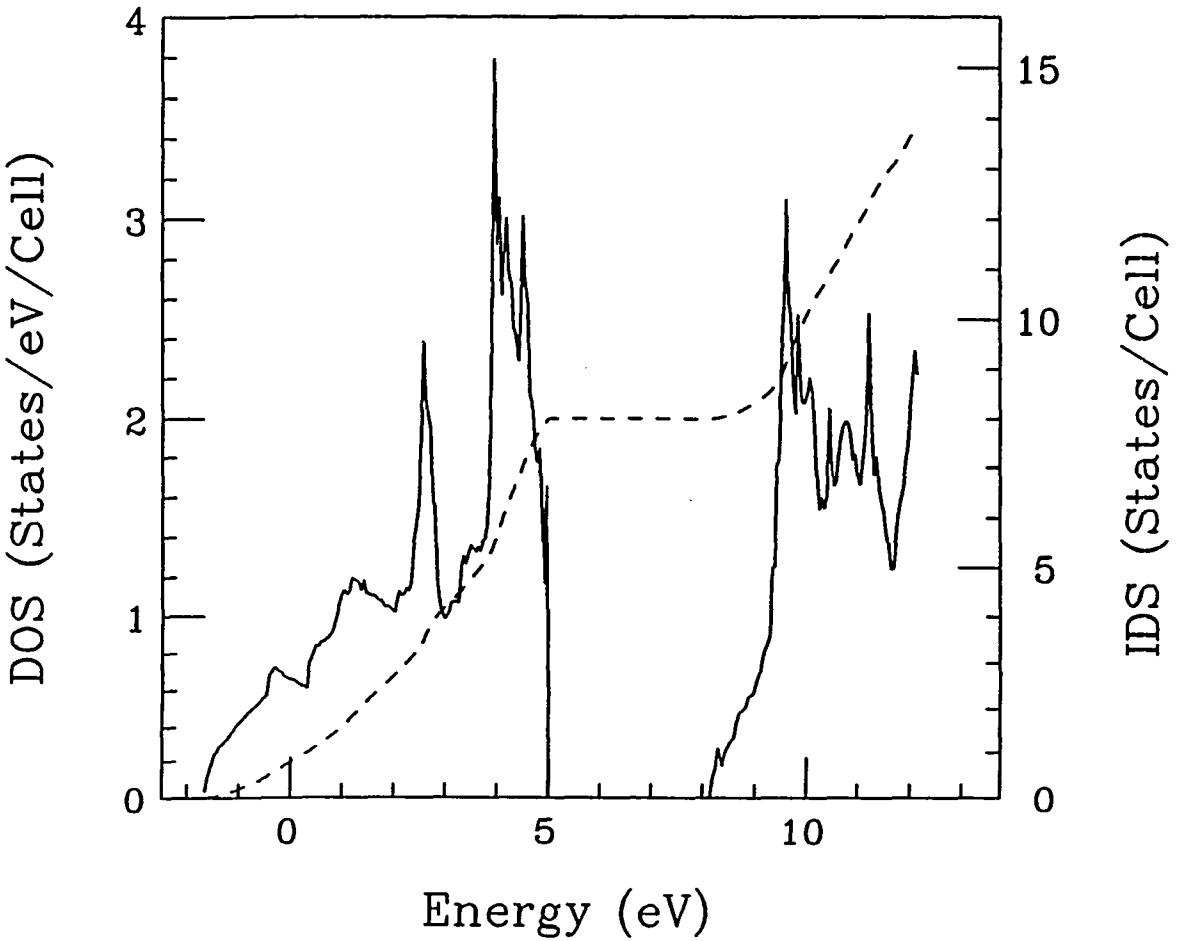

Fig. 5. Calculated electronic density of states (solid line, left scale) and the integrated density of states (dashed line, right scale) of MgH_2.

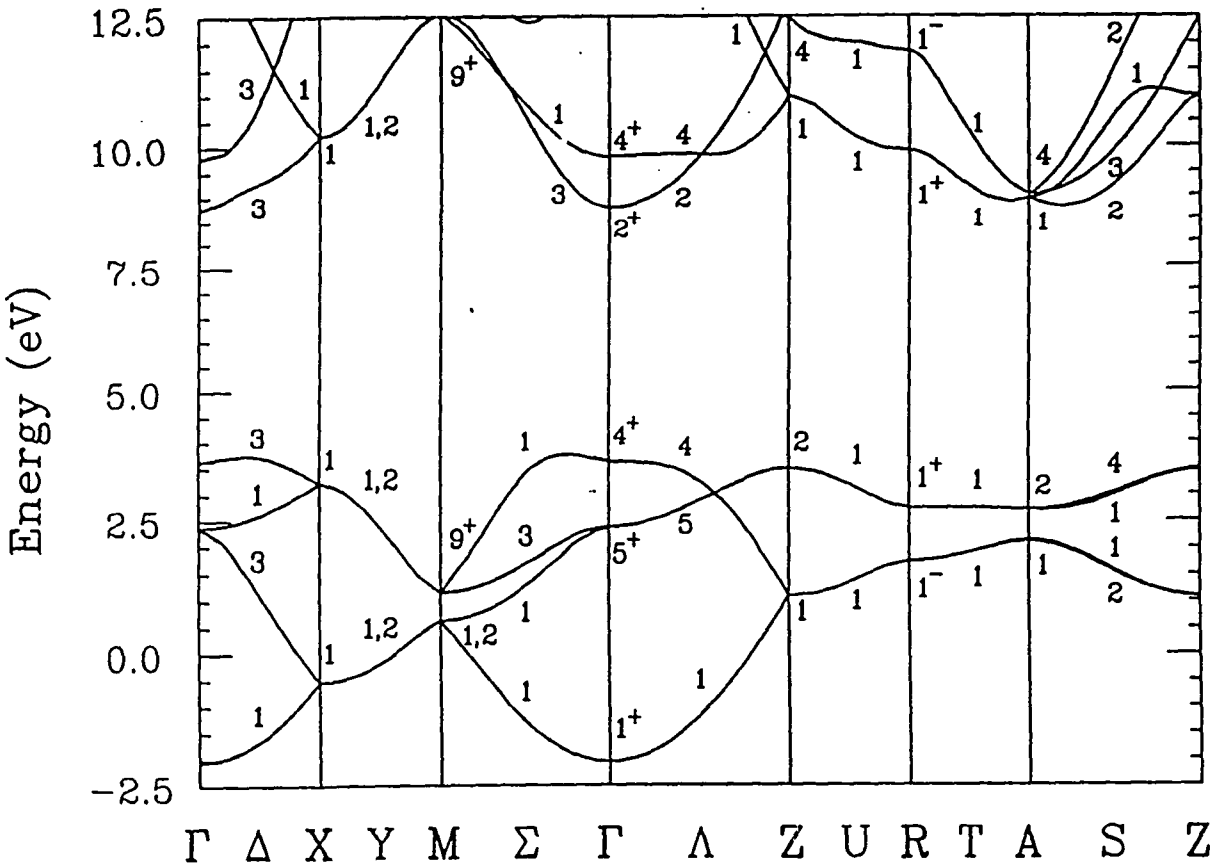

Fig. 6. Calculated electronic band structure of the hypothetical tetragonal crystal without the Mg atoms, but otherwise is the same as $\dot{M}gH_2$.

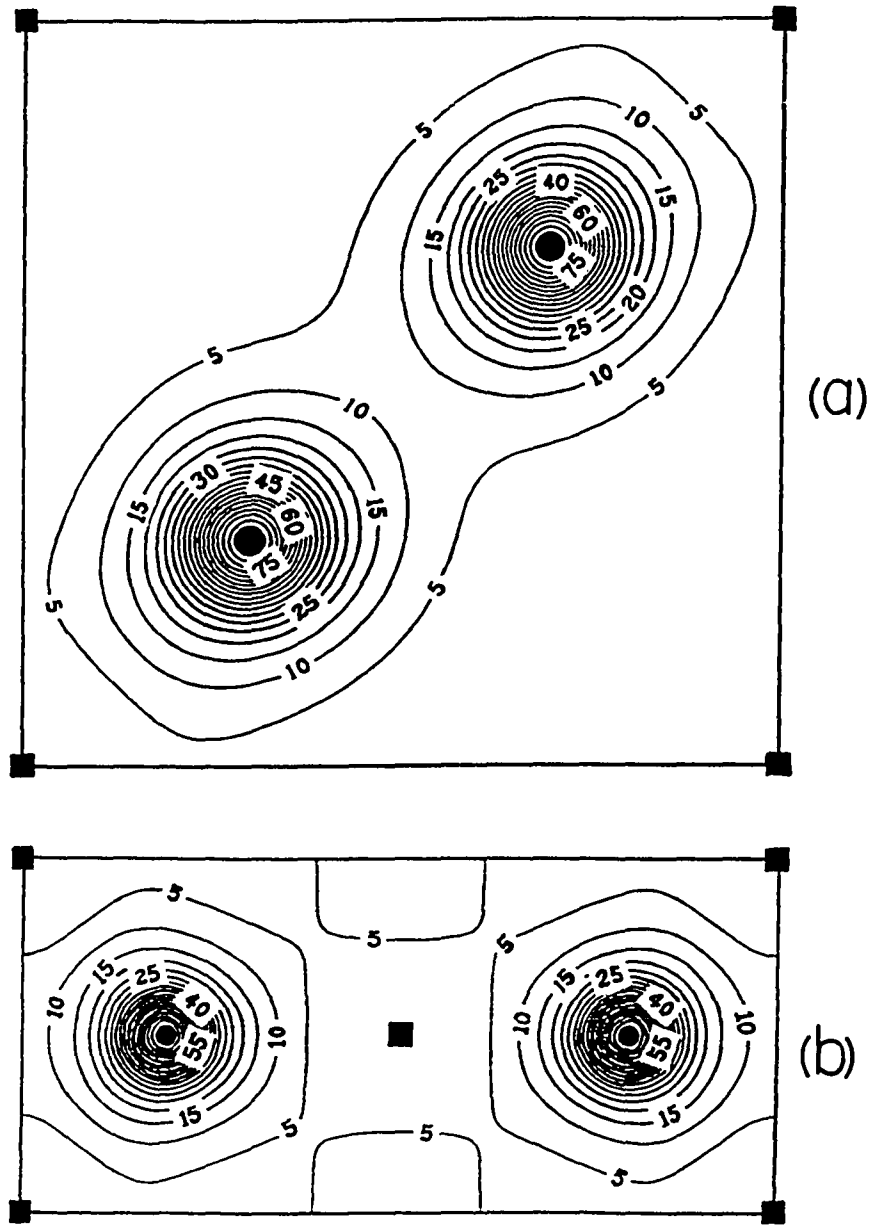

Fig. 7. Contour plots of valence electron charge density of MgH_2 in (a) (001) plane and (b) (110) plane. The solid squares indicate the positions of Mg ions and the solid circles the positions of H ions. The charge density is in units of electrons per unit-cell volume (425.5 a.u.).

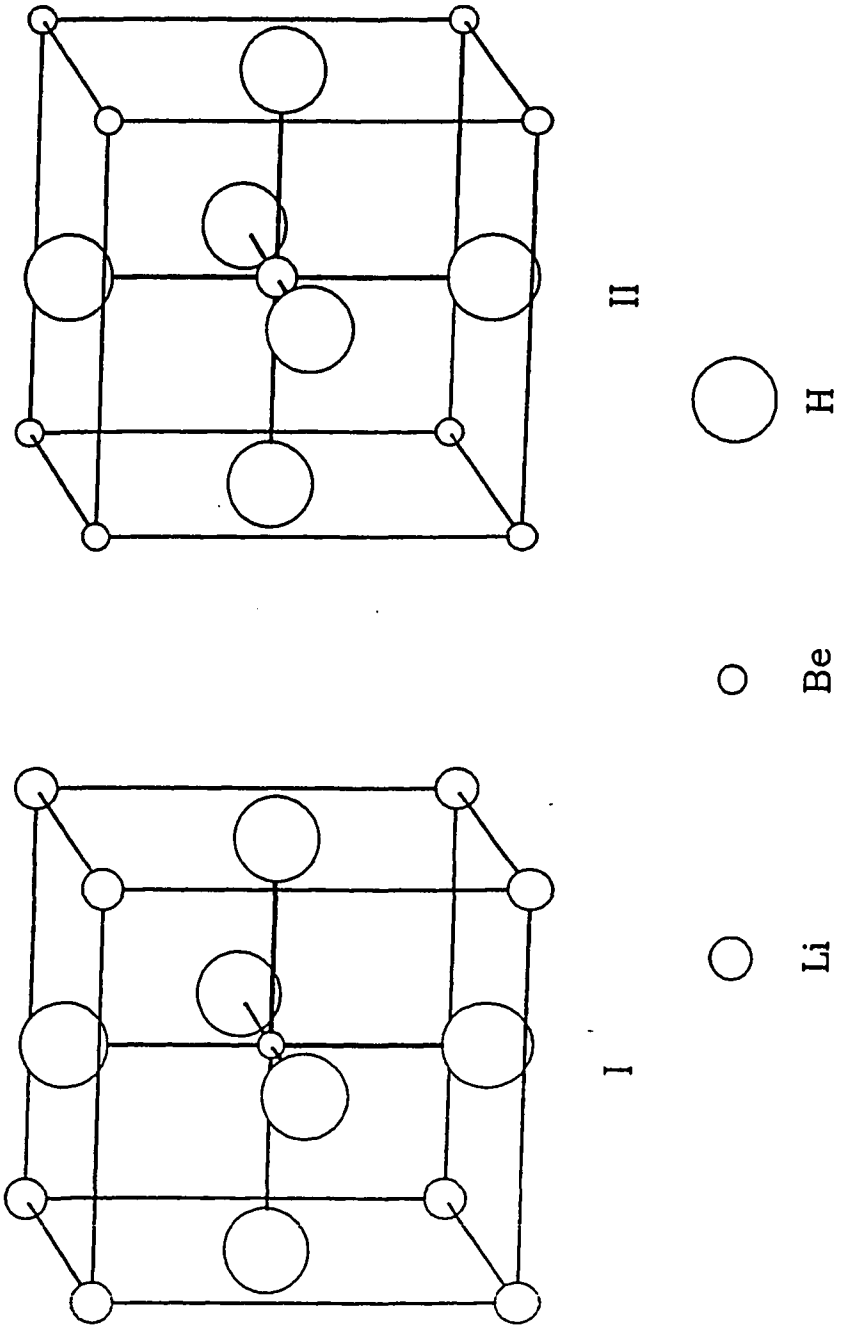

Fig. 8. Two assumed cubic perovskite structures of $LiBeH_3$.

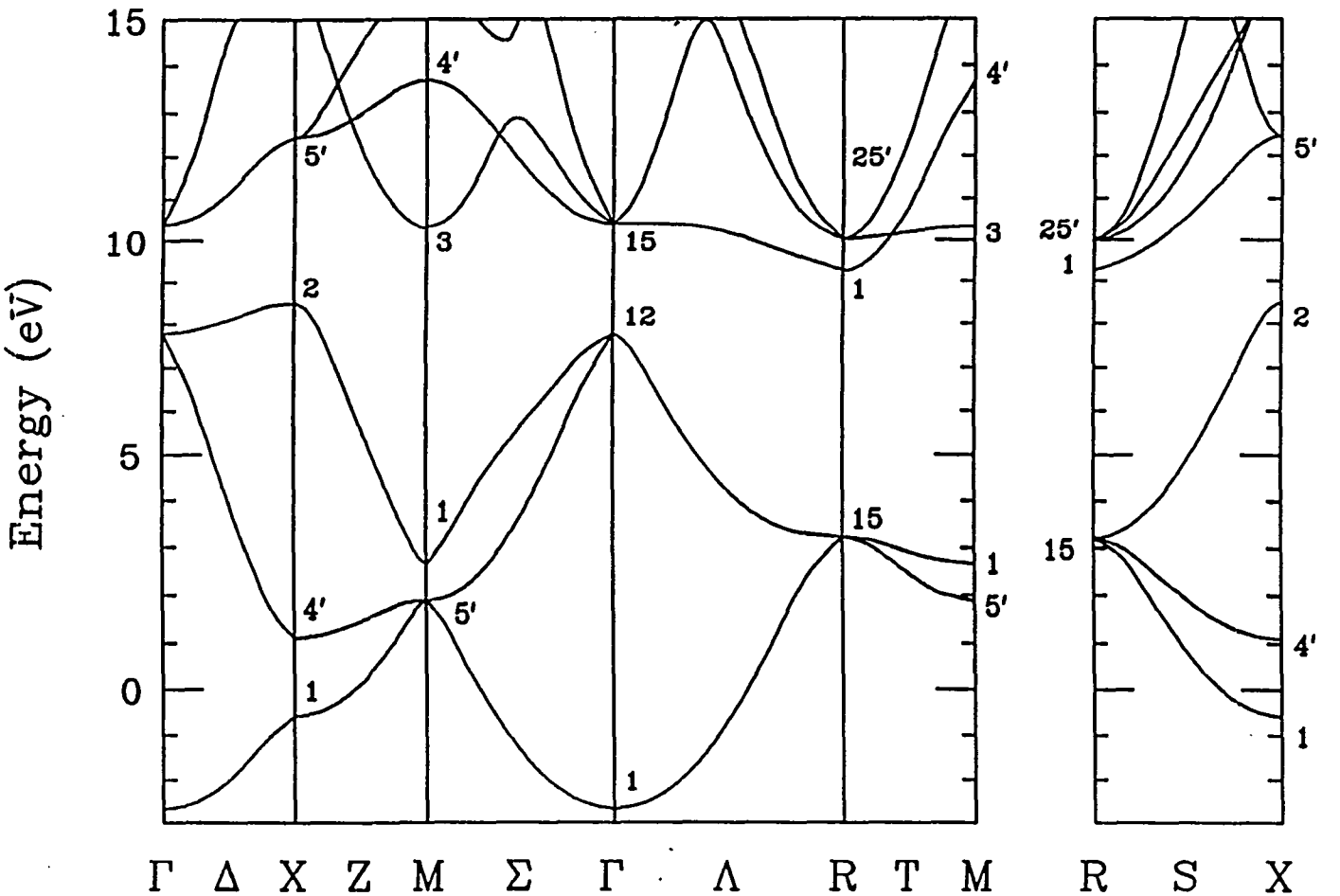

Fig. 9. Calculated electronic band structure of $LiBeH_3$ in the perovskite structure (I).

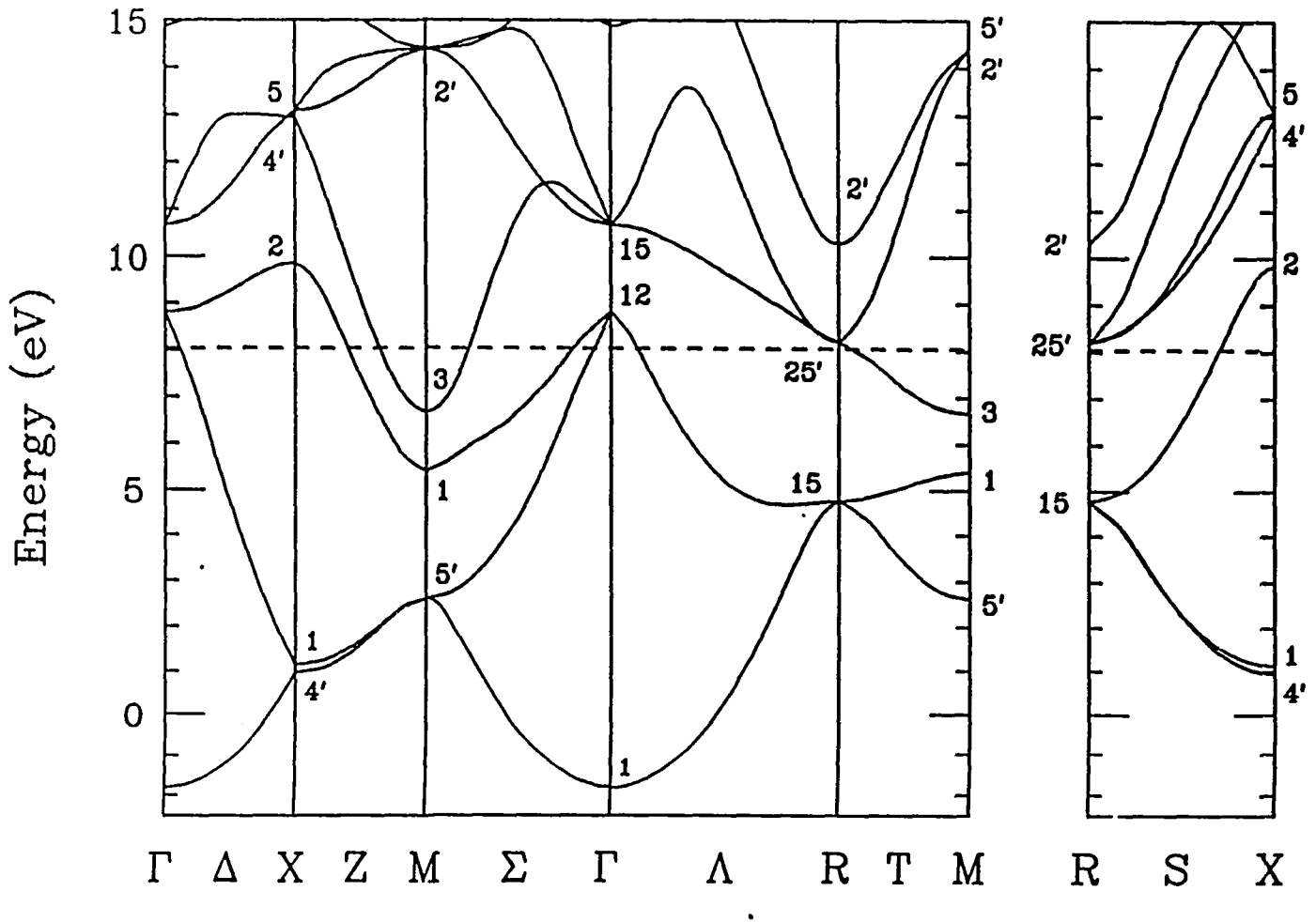

Fig. 10. Calculated electronic band structure of $LiBeH_3$ in the inverse perovskite structure

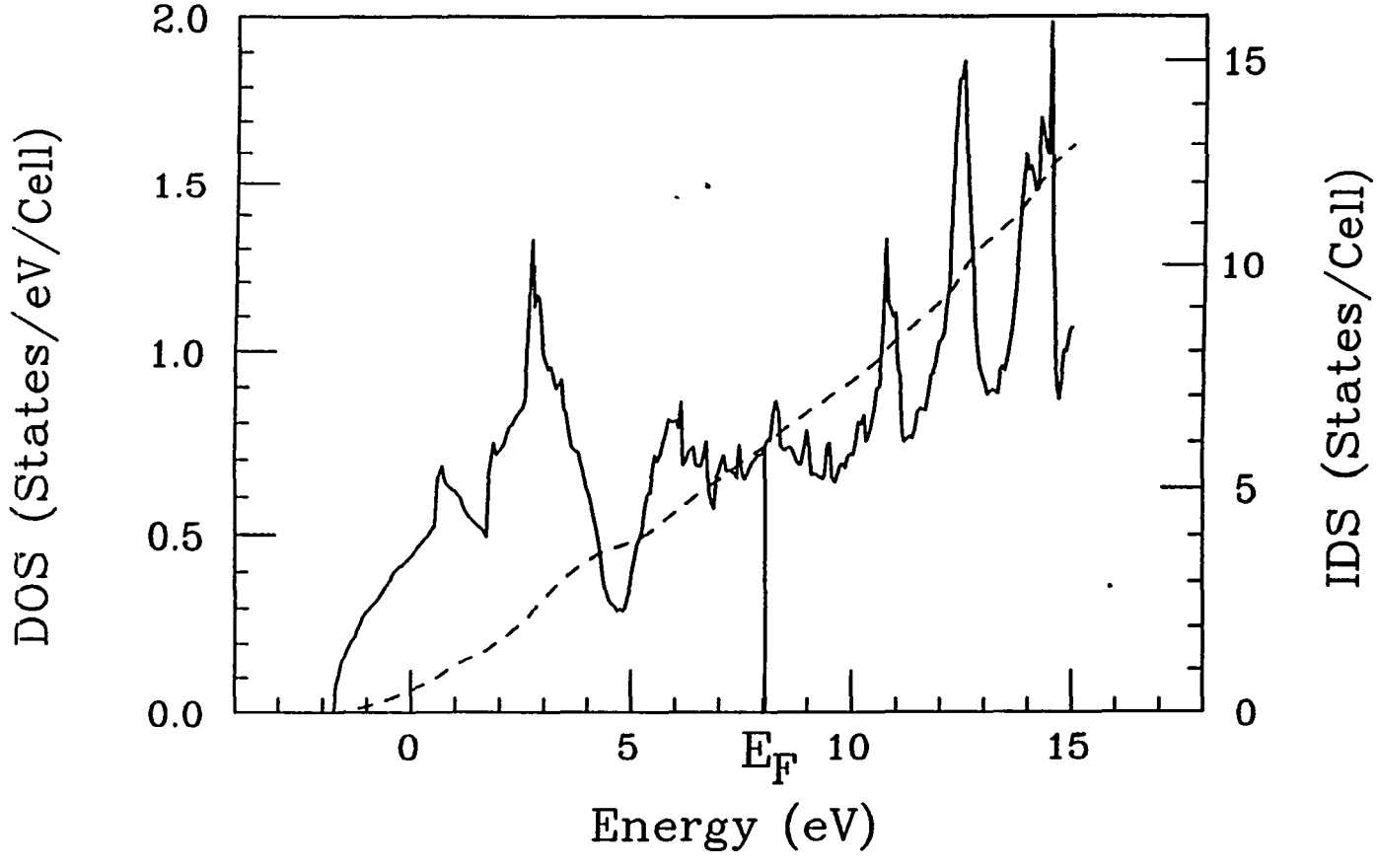

Fig. 11. Calculated density of states (solid line, left scale) and the integrated density of states (dashed line, right scale) of the inverse perovskite structure (II). The vertical line indicates the Fermi energy.

Chapter IV

Hydrogen on Metal Surfaces

1. Introduction

The study of the adsorption process has continually received intensive experimental and theoretical attention [1–6]. The adsorption of hydrogen on a metal surface presents a particularly simple physical system for theoretical investigation of substrate-adsorbate interaction because of the simple electronic structure of the hydrogen atom. Up until recently, the experimental and theoretical hydrogen adsorption study have been focused on transition metal surfaces. Realistic first-principles calculations have been performed for hydrogen on surfaces of various transition metals (metal substrates for which hydrogen adsorption have recently been studied include W [1], Ni [2], Pd [3], and Ru [4]). The focus on transition metals is partly owing to the technological importance of these systems; the transition metals are used in processes such as catalysis. The study of hydrogen adsorption on simple (*sp*) metals is also important. For example, light weight metals are ideal as hydrogen storage media because of their high concentration of hydrogen per unit weight. It is desirable to have good absorption and desorption kinetics, processes which are influenced by the metal-hydrogen interaction at the surface. However, few experimental adsorption studies on simple metal surfaces were performed until recently [5,6]. Theoretically, hydrogen adsorption on *free-electron-like* metals such as Na, Mg, and Al [7] has been studied using the jellium model for the metal substrate, where the effect of the lattice potential (pseudopotential) has been included via first-order perturbation theory. On the other hand, a non-perturbative

approach is needed to treat a metal substrate of first-row elements such as Li and Be, because they have relatively strong pseudopotentials.

In this chapter, we study adsorption of hydrogen on the (0001) surface of hexagonal-close-packed (hcp) simple metals, Be and Mg. Total energy results such as the stable adsorption site, adsorption energy, and H vibrational frequency are obtained. The energetics for H to go into the subsurface octahedral site is also investigated. The charge density distributions and the change in the work function upon adsorption of H are studied. The energy band structure is obtained for the clean and H-covered Be(0001) surface. Experimental results have recently become available for H adsorption on Be(0001) [6], with which we will compare our calculations. No detailed experimental data is available on H/Mg(0001). However, model calculation has been performed [7]. Comparisons are thus made with this model calculation [7]. The surface energy and work function of the clean surfaces are also obtained. This chapter is organized as follows. In Sec. 2, total energy results on clean and H-covered Be(0001) [8] are reported and compared with experimental results [6]. In Sec. 3, the electronic band structure, character of the surface states, the valence charge density and self-consistent potential for the clean and H-covered Be(0001) surface are described. The work function change due to the adsorption of H is obtained. Sec. 4 deals with the clean and H-covered Mg(0001) surface [9]. Discussions of the results and concluding remarks are made in Sec. 5.

2. H on Be(0001): Total Energy Results

Although the electronic configuration of Be atom is simple, Be crystal exhibits some unusual physical properties [10]. Its electronic band-structure and density

of states are quite different from the free-electron-like metals. The interaction between Be and H is also quite unusual. Beryllium hydride (BeH_2) was thought to consist of chains of Be bridged by hydrogen, and was postulated to have covalent bonding [11]. However, a recent experiment deduced that the structure is body-centered orthorhombic, in which each unit cell contains 12 corner-sharing BeH_4 tetrahedra [12]. The structure has no analog among other tetrahedra-forming materials such as BeF_2, SiO_2, and GeO_2 [12]. It is thus interesting to investigate the H—Be bonding. A direct theoretical study of the electronic bonding in this crystal, using a first-principles method, is difficult because of the large unit cell. The investigation of hydrogen adsorption on Be offers an opportunity to study some aspects of the bonding between hydrogen and beryllium.

There have been previous theoretical treatments of hydrogen on Be(0001) (the system is also denoted by H/Be(0001) in the following). Bagus and co-workers [13] have made extensive investigations using the cluster model. However, their calculated adsorption energy of hydrogen suffered large nonuniform variations from one cluster size to another [13]. The slab geometry commonly used in first-principles calculations was employed in the work of Angonoa *et al.* [14] using the self-consistent-field Hartree-Fock (SCF-HF) method. Although a few results were given for the adsorption energy and the bond length, their work focused on the electronic structure. No attempt was made to determine the stable adsorption site because a relaxed tolerance was used to reduce the computational cost, which severely limited the accuracy of their calculated total energy [15]. Ray and Plummer [6] have recently performed various experiments on chemisorbed atomic hydrogen on the Be(0001) surface. In particular, the vibrational frequencies of the adatom were measured using the electron energy-loss spectroscopy (EELS)

technique. Different vibrational modes were observed at low and high coverages. The low-coverage vibrational mode was tentatively assigned to the bridge site. The result of the cluster calculations of Bagus and co-workers [13] is in contradiction to this assignment.

We have calculated the adsorption energy of the hydrogen at different adsorption sites and found that the bridge site is indeed favored over the two hollow sites and the on-top site, in agreement with experiment [6]. We also obtain results for the equilibrium H—Be bond lengths and the frequencies of hydrogen vibration perpendicular to the surface. The energetics for the hydrogen to go into the subsurface octahedral site is also investigated; we find that it is highly unfavorable for the hydrogen to be in the subsurface octahedral site. By using a slab of Be thicker than used in previous calculations, we obtain a result for the surface energy of clean Be(0001) surface. We also calculate the work function of the Be(0001) surface and find it in good agreement with experiment.

2.1 Calculational Details

The Hedin-Lundqvist form [16] for the exchange-correlation potential is employed. The pseudopotential of the Be atom is generated in the electronic configuration of $1s^2 2s^1 2p^1$ and has been used previously in the calculation of bulk Be crystal [10]. By allowing both the a and c axes to relax, the calculated equilibrium lattice parameters of the Be crystal are found to be in agreement with experiments to within 2% [10]. The supercell method [17] is used to simulate the effect of the surface. In this method, slabs which comprise of layers of the substrate atoms are arranged periodically in the direction perpendicular to the surface being studied at a certain distance apart (Fig. 12). A surface calculation is thus treated on an

equal footing as a bulk calculation; the same computer code can be used for both calculations. Unless otherwise mentioned, the slabs will contain four Be layers and the vacuum space (space between the slabs) will have a thickness equivalent of six Be layers (the dimension of the supercell perpendicular to the surface is thus equivalent of ten Be layers). One hydrogen layer is "adsorbed" onto each surface of the Be slabs (Fig. 12). We assume that the Be atoms reside at their bulk positions, and we use the experimental values for the lattice constants [18]. Advantage is taken of the inversion symmetry associated with slabs which contain an even number of substrate layers. We have performed calculations with the hydrogen atoms in the four symmetry adsorption sites, i.e., the two hollow sites (hcp site, with a Be atom directly underneath; fcc site, without a Be atom underneath), the bridge site, and the on-top site (see Fig. 13(a)). With a kinetic-energy cutoff of 20 Ry for the plane-wave basis, the median size of the Hamiltonian matrices is $\sim 800 \times 800$. The result is considered self-consistent when the potentials in the last two iterations differ by about 1 mRy. We find that the total energy differ by less than 0.01 mRy in the last two iterations. Some convergence tests of our results are carried out with respect to various parameters which will be discussed along with the results below. Because of computational limitations, the calculations are performed in the high-coverage limit only, with one H per surface Be atom (unit coverage), where the adsorbed H atoms form a two-dimensional triangular $p(1 \times 1)$ lattice on the surface (Fig. 13(b)).

2.2 Clean Surface

The Be(0001) surface is known not to reconstruct and the surface relaxation is minimal [19]. No surface relaxation is thus considered in our calculations. Two

physical quantities of the clean Be(0001) surface are calculated, the surface energy, E_s, and the work function of the clean surface, ϕ.

The surface energy measures the amount of work necessary to split the solid into two semi-infinite parts along the surface in question. In a slab calculation, the surface energy per surface atom is given by

$$E_s = \frac{1}{N_s}(E_{\mathrm{slab}} - N_{\mathrm{slab}}\, E_{\mathrm{bulk}}), \tag{4.1}$$

where E_{slab} and N_{slab} are, respectively, the total energy and the number of atoms per unit cell in the supercell calculation, E_{bulk} is the total energy per atom from a bulk calculation of Be, and N_s is the number of surface atoms per unit cell in the supercell calculation. For the slab geometry described above, $N_s = 2$ (each slab has two surfaces) and $N_{\mathrm{slab}} = 4$. With 12 k-points within the $\frac{1}{12}$ irreducible part of the surface Brillouin zone (ISBZ), we obtain a surface energy of 0.60 eV per surface atom. Converting to surface energy per unit area, this is 2.1 J/m^2. Various convergence tests have been carried out. In Table V, the calculated surface energy is given for slabs consisting of different number of Be layers and vacuum sizes. The results show a variation of $\sim$ 0.02 eV per surface atom about the above value. When the number of k-points in the ISBZ is increased from 12 to 20, the surface energy lowers by only 0.005 eV per surface atom. The cutoff energy of 20 Ry is sufficient for the clean surface, since the bulk calculation is already well-converged at a cutoff energy of 10 Ry [10]. In fact, we obtained an increase in the surface energy of only 0.001 eV when the cutoff energy is raised to 25 Ry. The surface energy obtained is thus accurate to within $\sim$3%.

To our knowledge, no experimental value for the surface energy of Be(0001) is available. First-principles theoretical evaluation of surface energies has been

performed for some transition metal surfaces [20]. The surface energy of the free-electron-like metals has been calculated using the jellium model [21]. For comparison, our calculated value for Be(0001) (2.1 J/m^2) is smaller than the calculated value for Ru(0001) [20] (3.0 J/m^2) by 30%, but is greater than the surface energy of other simple metals [21] (e.g., ~ 1.2 J/m^2 for Al(111)). A rough estimate of the surface energy can be obtained from the cohesive energy of the crystal by viewing the formation of a solid from separate atoms in the following way [20]. Assume each atom is a sphere with the radius $R = [3V_a/(4\pi)]^{1/3}$ with V_a being the bulk atomic volume. When the atoms come together to form a solid, the surfaces of the atoms are eliminated and the surface energies released, giving rise to the cohesive energy. The surface energy per unit area is thus

$$\sigma = E_{\text{coh}}/(4\pi R^2), \tag{4.2}$$

where E_{coh} is the cohesive energy per atom in bulk Be. Using the experimental value 3.32 eV/atom [22] for E_{coh}, Eq. (4.2) gives a value of 2.7 J/m^2 for Be(0001), which is 29% larger than the calculated value. A similar estimate for Ru(0001) is 25% greater than the first-principles calculation [20].

Experiments have turned out a wide range of values for the work function of Be. An earlier standard reference [23] recommends a value of 3.92 eV. More careful experiments performed thereafter give 5.08 ± 0.08 eV and 4.98 ± 0.10 eV for polycrystalline films, and 5.10 ± 0.02 eV for a single-crystal surface [24]. The work function is given by

$$\phi = V(\infty) - E_F\,, \tag{4.3}$$

where $V(\infty)$ is the potential far away from the surface (vacuum level) and E_F is the bulk Fermi energy. In our calculation, $V(\infty)$ is taken to be the potential in the

middle of the vacuum region, averaged in the directions parallel to the surface. The work functions obtained using 12 k-points in the ISBZ and $E_{\max} = 20$ Ry are listed in Table V for different slab and vacuum sizes. The result is $\phi = 5.0 \pm 0.2$ eV. The work function shows a small dependence on the slab thickness and the vacuum size, but is on the same order as the uncertainty of 0.1 eV in determining E_F and $V(\infty)$. When the number of k-points is increased from 12 to 20, we obtain $\phi = 5.0$ eV. Our calculation agrees well with the more recent experimental values as quoted above.

There have been theoretical studies of monolayer and dilayer films of Be [25,26]. Since these films are not thick enough to simulate the bulk of the Be crystal, a total energy calculation can only give the cohesive energy for the particular films; the surface energy of the Be(0001) surface cannot be determined. On the other hand, the calculated work functions of the thin films are fairly close to the experimental value for the semi-infinite metal. The work of Boettger and Trickey [25], using a method that employs fitting of charge density and potential to Gaussian-type functions, gave 4.80 eV and 5.11 eV for the monolayer and dilayer films, respectively. The geometry of the films was determined by minimizing the total energy [25]. The linearized augmented-plane-wave calculation of Wimmer [26] obtained a value of 5.19 eV for a monolayer film ($a = 4.20$ a.u. instead of the experimental value of 4.32 a.u.). These are all local-density calculations employing the Hedin-Lundqvist [16] exchange-correlation potential. These values are in close agreement with each other and with the experimental value for the Be(0001) surface. The difference of 0.39 eV between the two monolayer results probably arises from the slightly different geometries and possibly a contribution due to different methodology.

2.3 Adsorption Site and Energy

To determine the minimum-energy site of the adsorbed hydrogen, the total energy is calculated for the hydrogen at the four high-symmetry sites (Fig. 13(a)) and for various vertical distances, h, from the surface Be layer. We define the adsorption energy with respect to isolated H atoms and the clean Be surface,

$$E_{\mathrm{ad}} = \frac{1}{2}(E_{\mathrm{H/Be}} - E_{\mathrm{Be}}) - E_{\mathrm{H}}\,, \tag{4.3}$$

where $E_{\mathrm{H/Be}}$ and E_{Be} are, respectively, the total energy per unit cell for H-covered and clean Be slab. E_{H} is the energy of an isolated H atom. The $\frac{1}{2}$ factor comes from the fact that H is adsorbed on both surfaces of each slab. We use the value -0.958 Ry for E_{H}, calculated with the Ceperly-Alder correlation potential as parametrized by Perdew and Zunger [27]. The dependence of the adsorption energies on the vertical distance is shown in Fig. 14. The curves are least-squares fits of the calculated points to polynomials in h,

$$E_{\mathrm{ad}} = E^0_{\mathrm{ad}} + \sum_n c_n(h - h_0)^n\,, \tag{4.4}$$

where h_0 is the equilibrium H-surface distance and E^0_{ad} the adsorption energy at $h = h_0$. The order of the polynomials ranges from 2 (for the on-top site) to 5. The values for both quantities obtained from the fit, Eq. (4.4), are summarized in Table VI. It should be pointed out that the absolute value of the calculated adsorption energy may not be accurate because the local-density approximation cannot simulate the exchange-correlation effects adequately in both the atomic and adsorbate limits. Hence, care must be exercised in comparing the absolute value of the calculated adsorption energy to the binding energy of the H_2 molecule so as to deduce whether the adsorption is dissociative or not [28]. Experimentally, only

atomic hydrogen is found to adsorb on the Be(0001) surface, i.e., the hydrogen molecule cannot be dissociated by the surface [29]. Despite the inaccuracy of the absolute values, the relative adsorption energies for different sites are expected to be good. From Fig. 14 and Table VI, the bridge site has the lowest adsorption energy and is thus the stable adsorption site. This result is consistent with the assignment by Ray and Plummer [6] of the adsorption at low coverages (see below). The fcc and hcp sites are next in order, the adsorption energy for the fcc site being approximately 0.1 eV more negative than that for the hcp site. A difference of the order of 0.1 eV between the two hollow sites seems to be typical for H adsorption on most close-packed metal surfaces [30]. The on-top site is the most unstable, with the adsorption energy being 0.5 eV higher than that for the hcp site. The distance between the adsorbed H and their nearest Be atoms, d, which is referred to here as bond length, are calculated and are also listed in Table VI. We observe that the bond length decreases from the hollow sites to the bridge site, and to the on-top site, viz., as the number of nearest neighbors decreases. For the fcc and hcp sites, the bond length is found to be $\sim$ 1.6 Å, which is about the same as that in $LiBeH_3$ (assuming a cubic perovskite structure) [31]. The calculated bond length for the on-top site is 1.42 Å, which is still slightly greater than the 1.34 Å of the BeH molecule [32], but coincides with the H—Be distances in crystalline BeH_2, which range from 1.38 Å to 1.44 Å [12].

It is important to check the result using a different cutoff energy for the plane-wave basis, since the presence of hydrogen requires a large cutoff energy to arrive at a good convergences. We have done this by repeating the calculation for the bridge site and the two hollow sites with a cutoff energy of 25 Ry. The hydrogen-substrate distances are fixed at the equilibrium values obtained with the

20-Ry cutoff energy [33]. The adsorption energy increases by 0.161, 0.175, and 0.173 eV for the bridge, fcc, and the hcp sites, respectively. Thus, the difference between the adsorption energies for the bridge site and for the fcc site decreased by only 0.014 eV. This is a small value compared to the adsorption energy difference itself indicating that the ordering of the adsorption energies will probably be the same when a larger cutoff energy is used. The change in the calculated adsorption energy with respect to the number of k-points in ISBZ is also found to be small ($\sim$ 0.01 eV). We have also calculated the adsorption energy for different slab and vacuum sizes using the same $E_{\max}$. The adsorption energies changes by as much as 0.03 eV, but the difference between the adsorption energies changes by only 0.01 eV.

2.4 Vibrational Frequency of H

With the fitted adsorption energy as a function of h, Eq. (4.4), the energy levels of the H vibration perpendicular to the surface are evaluated by diagonalizing the hamiltonian matrix for the H motion in the basis of the simple-harmonic-oscillator eigenfunctions. The calculated excitation energies are listed also in Table VI. The uncertainty in the frequency is about 2 meV, as inferred from using different fitting polynomials. The deviation from the harmonic frequencies due to the higher order terms is only 2—3 meV for the hollow sites and $\sim$ 5 meV for the bridge site.

The measurement of vibrational frequencies of H has been made using the electron-energy-loss spectroscopy (EELS) technique for different surface coverages by Ray and Plummer [6]. They observe a high frequency mode of 185 meV at low H coverages (the exact coverages are not known). As the coverage increases,

this mode disappears and two new vibrational modes of lower frequencies are observed at 158 and 170 meV. They have tentatively assigned the low-coverage mode to the bridge site and the high-coverage modes to a tilted bridge site. As discussed above, our calculated adsorption energies are consistent with the assignment of the bridge site at low coverages. But our calculated hydrogen vibrational frequency for the bridge site in the present calculation is 168 meV, which is smaller than the experimental value by 17 meV. This discrepancy can be resolved by recognizing two major differences between the experimental situation and our calculation. First, the dynamics of the Be substrate is not taken into account in our calculation. In reality, the hydrogen oscillation couples to the substrate. With mass ratio $m_H/m_{Be} \simeq 0.1$, the substrate motion is not negligible. We have simulated this effect by using pair-interactions between H and their nearest-neighbor Be atoms and between Be atoms. The force constant for nearest-neighbor H—Be interaction is 12.9×10^4 dyn/cm, chosen so that the vibrational frequency equals the value obtained from our first-principles calculation, 168 meV, when Be atoms are assumed to be stationary. The force constants between the substrate Be atoms are obtained from a previous study of the bulk Be phonon spectrum [34]. The result indicates that an increase of around 10 meV is obtained when the dynamics of the substrate is taken into account. Since the substrate force constants ($\sim 3 \times 10^4$ dyn/cm) are much smaller than the H—Be force constant, the 10 meV increase is due mainly to the reduced mass effect. Indeed, the resulting frequency changes very little when the Be—Be force constants are set identically to zero. The second factor which contributes to the difference between experiment and theory is that the experimental frequency is obtained at low coverages while our calculation is performed for a $p(1 \times 1)$ lattice corresponding to unit coverage. In the present system, the frequency is experimentally observed

to decrease with increasing hydrogen coverage; the 185-meV oscillation was seen to shift to 181 meV, as coverage increases, before it disappears [6]. This change in the frequency could arise from the redistribution of charge density around the hydrogen under consideration, due to the occupation of nearby sites. In the absence of any knowledge of hydrogen coverage in the experiment, we do not know what the shift would be at unit coverage. However, the theoretical result, 178 meV, taking into account the effect of the substrate, is sufficiently close to the experimental value of 181 meV, the frequency of this vibration mode before it disappears.

The calculated adsorption frequencies at the fcc and hcp sites are almost the same (they differ by only 3 meV). This is in agreement with other work on close-packed metal surfaces (see, e.g., Ref. 5). The two lower frequencies, 158 meV and 170 meV, which appear at high coverages, exhibit a splitting of 12 meV. Thus they are not likely to be associated with the hcp and fcc site adsorptions. These modes were assigned to a tilted bridge site by Ray and Plummer [6], which is not considered in the present work due to computational limitations.

2.5 H in Subsurface Site

There are two subsurface (between the surface layer and the second layer) symmetry sites: the octahedral site and the tetrahedral site (surrounded by six and four Be atoms, respectively). A likely route for hydrogen to go into the metal is from the fcc adsorption site to the subsurface octahedral site. In order to study the energetics for H to go into the bulk, the adsorption energy is calculated for several H positions along the straight line which connects the surface fcc site to the subsurface octahedral site. The result is shown in Fig. 15. The hydrogen has

to overcome a rather large energy barrier ($\sim$ 1.6 eV) to go into the subsurface octahedral site from the fcc site. The potential well around the octahedral site is relatively shallow (0.2 eV). There is a difference of 1.4 eV between the potentials at the octahedral site and at the fcc site. We note that the potential curve in Fig. 15 is derived by placing a layer of hydrogen parallel to the surface. When a single hydrogen atom moves beneath the surface, the lattice may distort around it; the energy barrier and the energy of hydrogen in the subsurface site with respect to the surface site will be slightly smaller than the calculated values given above. At much higher coverages, the repulsion between H on the surface may make it energetically favorable for some of the hydrogen to occupy the subsurface sites. A theoretical investigation of such a situation was recently performed for H/Ru(0001) by Chou and Chelikowsky [4].

3. H on Be: Electronic Properties

In this section, we present the calculated electronic properties of the clean and hydrogen-covered Be(0001) surface. The band structure, character of the surface states, charge density distribution, self-consistent potential, and work function will be covered.

3.1 Band Structure and Surface States

A surface terminates the periodicity of a crystal along the its normal. Since the quantum number k_z (along the normal of the surface) is no longer a good one, this will change the character of bulk-like states (extended states) near the surface. A more significant change, however, is the appearance of states which are localized near the surface. These are called *surface states* (SS). Two types

of SS exist: *bona fide* SS which are located in the energy gap of the bulk band structure and *surface resonances* which exist within the bulk band structure. In our supercell calculation (see subsection 2.1 of this chapter), each slab has two surfaces. Thus for each experimentally observable SS, there are two such states in a slab, one localized on each surface. Because of the finite extent (decaying length) of the SS, the two states localized near the surfaces interact. A pair of states, which in our case are symmetric and antisymmetric under inversion, results from this interaction. There is an energy splitting between this paired SS, which decreases as the slab becomes thicker. We will examine the surface band structure and the SS that exist on the clean and H-covered Be(0001) surfaces.

The surface Brillouin zone (SBZ) for Be(0001) is shown in Fig. 16(a). In Fig. 17, we show the bulk band structure projected onto the SBZ; the bands are calculated for $k_z = 0, 0.1, 0.2, 0.3, 0.4, 0.5$ in units of $2\pi/c$ (c is the lattice constant of the bulk Be along the hexagonal axis). The boundary between the allowed energies and the gap regions is for the most part determined by the $k_z = 0$ bands. This projected band structure (PBS) will be helpful in identifying SS since the *bona fide* surface states are located in the gaps of the PBS.

It is convenient for computational purposes to use a thin slab for surface calculations. However, some physical characteristics may not be simulated correctly if the slab is too thin. For instance, the (occupied) bandwidth of the bulk-like bands is likely to be smaller than the bulk value. Some surface states may also not appear in thin slab calculations or are not where they should be energetically even if they do appear. Calculations are thus carried out for slabs of different thickness. We find that a ten-layer slab provides a good representation of the bulk and the surface, as the results compare favorably with experiment (below). The

band structure for the clean surface as obtained from a ten-layer slab is shown in Fig. 18. We have used the dashed lines to mark the boundary of the PBS from Fig. 17. The energy is referenced with respect to the Fermi level (see below). Examination of the location of the states shows the following three SS pairs at the symmetry points: one within the gap of the PBS at $\overline{\Gamma}$, one deep in the gap of the PBS at $\overline{M}$ and another one at $\overline{M}$ which is very close to (within 0.1 eV of) the edge of the PBS. The averages of the Kohn-Sham eigenvalues of the SS pairs are summarized in Table VII (the energy splittings are 0.1 eV for the first SS pair and a few meV for the latter two). The experimental results of Karlsson *et al.* [35] and Bartynski *et al.* [36] are also tabulated. Our results are in good agreement with experiments. The band structure of Be(0001) as calculated with a ten-layer slab has been obtained by Chulkov *et al.* [37] using a similar approach. Calculations for thinner slabs has also been performed by Boettger and Trickey [38]. The results of Chulkov *et al.* and of Boettger and Trickey are also given in Table VII. Since the SS have been analyzed closely [37], we only mention some important features. The SS at $\overline{\Gamma}$ is p_z-like, the upper SS at $\overline{M}$ is $p_{x,y}$-like, while the lower one is of s and $p_{x,y}$ character. The SS at $\overline{\Gamma}$ has a longer decay length and thus larger energy-splitting between the symmetric and antisymmetric states. The upper SS at $\overline{M}$ is localized in the first (surface) and second Be layers while the lower one is localized in the second and third layers.

Since the stable adsorption site is the bridge site, we determine the band structure for a $p(1 \times 1)$ lattice of H in the bridge site of Be(0001). Both surfaces of the ten-layer substrate slab are covered with H atoms, which are located at the calculated equilibrium position (0.98 Å above the surface Be layer). The H overlayers reduce the symmetry of the slab (there is now only one reflection

operation). The new irreducible part of the Brillouin zone is shown in Fig. 16(b) (note that inversion is still a symmetry operation). In order to compare with the clean surface, we shall determine the band structure along the directions corresponding to the symmetry lines for the clean surface (Fig. 16(a)) (these are now not necessarily symmetry lines for the H-covered surface). There exist two sets of such directions, the second set we shall distinguish by a subscript 2 (see Fig. 16(b)). The calculated band structure along these lines are shown in Fig. 19(a) and (b). We first observe that the SS at $\overline{\Gamma}$ and the upper SS at $\overline{M}$ of the clean surface in the gap of the PBS have vanished. Two SS pairs exist in the gap of the PBS. One SS pair is found at $\overline{M}$ at a binding energy of 2.8 eV ($\sim$ 0.2 eV above the edge of the bulk bands). The position of this SS is thus similar to that of the lower SS at $\overline{M}$ of the clean surface. Another SS pair located in the gap of the PBS is at $\overline{M}_2$ and is unoccupied, at a binding energy of -1.0 eV. A new feature of this H-covered surface is the existence of H-induced split-off SS. From Fig. 19, the split-off SS exist in all directions shown except over portions of $\overline{\Sigma}$ and $\overline{T}'$ about the $\overline{M}$ point. At $\overline{\Gamma}$, the binding energy of the split-off SS is 11.4 eV, only 0.2 eV below the valence band edge of Be. The dispersion of the split-off SS bands is free-electron-like, as the bands follow closely the boundary of the PBS. Along $\overline{T}'_2$, the split-off SS are strongly bound. The binding energy is 5.98 eV at $\overline{M}_2$ and 3.78 at $\overline{K}$. In contrast, a resonance state occurs at $\overline{M}$ at a binding energy of 3.6 eV (6th and 7th states from bottom in Fig. 19(a)). The binding energies of the SS are tabulated in Table VIII.

The charge density of the surface states are shown in Fig. 20. Angular-momentum decomposition is also performed for the surface states to analyze their bonding characteristics. Wave functions are decomposed within spheres of radius

2.36 a.u. (Wigner-Seitz radius) at the Be sites and of radius 2.40 a.u. (ionic radius) at the H site. Components of s, $p_{x,y}$, and p_z orbitals around the surface Be atoms, second-layer Be atoms and H atoms are given in Table VIII for the SS (resonance). The charge density of the shallow split-off SS at $\overline{\Gamma}$ (Fig. 20(a)) is seen to be relatively extended at the H site, reminiscent of the lowest H state at Γ in simple metal-hydrides. Angular-momentum decomposition (Table VIII) indicates that only the Be-s orbital, which is located in the lower portion of the valence bands [10], is appreciable. The wave functions of the SS decays slowly into the bulk. The charge density of the split-off states at $\overline{M}_2$ and $\overline{K}$ are shown in Fig. 20(b) and (c), respectively. Unlike the deep SS pairs of the clean surface at $\overline{M}$, the charge distribution of these two states is well localized above and in the surface layer. Both Fig. 20(b) and (c) show clearly Be-p—H-s bonding. The states contain little s or p_z orbitals around the surface Be atoms according to angular-momentum decomposition (Table VIII). The split-off bands along $\overline{T}_2'$ are thus Be-$p_{x,y}$—H-s bonding states. The sum of the charge density of the 6th and 7th states at $\overline{M}$ in the ten-layer calculation are shown in Fig. 20(d). These states are apparently well-localized on H and surface Be atoms. Energetically, the states are located within the bulk bands. They are thus surface resonance states. These states have large s-component at the H sites as the Be—H bonding states at $\overline{M}_2$, but the $p_{x,y}$ component of surface Be is much smaller. In addition, there is a significant s component (0.12 electrons) at the surface Be site. The SS pair at $\overline{M}$ is mainly $p_{x,y}$ and p_z at the surface Be. The charge density is quite extended, which likens the states to the lower SS of the clean surface at $\overline{M}$. The wave function below the surface should not be expected to be the same since the potential is changed by the chemisorbed hydrogen (see below). Thus, these states has larger $p_{x,y}$ components in the first and second Be layers, whereas the SS of the clean surface has large

$p_{x,y}$ components in the second and third layers. Lastly, the unoccupied SS at $\overline{M}_2$, localized around H and in the first and second Be layers, consists of s and some d (0.08 electrons at surface Be and 0.02 electrons at second layer Be) orbitals of Be and s and p orbitals of H. This state may be viewed as a bonding state of H and the unoccupied Be states at $\overline{M}$.

The Be-s—H-s bonding state at $\overline{\Gamma}$ has a very small split-off energy. Such a split-off state has never been found experimentally or theoretically for chemisorbed hydrogen on metal surfaces. However, in the case of a hydrogen impurity in a bulk jellium with $r_s > 1.9$ a.u., a shallow bound state has been found [39]. The wave function of this bound state is rather extended [40]. Its binding energy increases as r_s becomes larger, but is always less than 0.3 eV. Other jellium-type calculations for chemisorption of H or H in vacancies [41] did not find such a bound state. Since the binding energy depends on the background electron density, the existence of such a split-off SS may well depend on which chemisorption site the hydrogen is in. Our preliminary calculation of the band structure on Be(0001) with a monolayer of H in the fcc site does not show any sign of such a split-off SS. The Be-$p_{x,y}$—H-s bonding along $\overline{T}_2'$ can be easily understood in terms of the direction and phase of the orbitals. Schematic diagrams of the bonding orbitals are shown in Fig. 21. The Be—H bond is along the x-axis (see Fig. 13(b)). At the $\overline{M}_2$ point, the direction of the Be-$p_{x,y}$ orbitals before the bonding (that is, orbitals of the clean surface) is at a 30° angle with the x-axis (Fig. 21(a)). The phase difference between two neighboring atoms of the same kind along the x-axis is exactly π. Thus the H-s and Be-p orbitals are always in phase with each other (Fig. 21(a)). Their overlap is large since the Be—H distance parallel to the surface is only 2.16 a.u. The bonding between these orbitals is strong judging from the large split-off energy.

The direction of the p orbital after the bonding is shown in Fig. 21(b). The p orbital is oriented closer to the Be—H bond direction which increases the orbital overlap. At $\overline{K}$ point, the bonding is more complicated since the phase difference between two atoms of the same kind along the x-axis is not π but $2\pi/3$. Despite this fact, the Be-p—H-s bonding can be still dominant. Here the surface Be-p orbital is much closer to H (at 15° with the x-axis) before bonding and is aligned exactly with the Be—H bond after the bonding (Fig. 21(c) and (d)). The bonding at any k-point between $\overline{M}_2$ and $\overline{T}$ along $\overline{T}_2'$ should be intermediate between the two cases. The situation is quite different at $\overline{M}$. In this case, the $p_{x,y}$ orbital of the clean surface is perpendicular to the Be—H bond and thus cannot produce strong bonding with H-s along the x-axis. It can, however, form bond with H along y-direction. This bonding is much weaker because of the longer distance between Be and H (see Fig. 13(b)). There could also be Be-s—H-s bonding along the x-axis. These types of bonding are present in the surface resonance at $\overline{M}$.

In finite-size slab calculations, the calculated Fermi energy for the slab may not be the same as the true bulk Fermi energy, which can only be approached as the slab becomes very thick. This finite-size effect can be pronounced if the bulk density of states near the Fermi level is low, which is the case for Be [10]. In fact, we find that the calculated Fermi energy for the twelve-layer slab (including the two H layers) is much too high. This is different from the clean surface where the calculated Fermi energy is found to be quite accurate. This is because the Fermi energy is pinned by the SS at $\overline{\Gamma}$ for the clean surface. (There are $(n+1)$ occupied states at $\overline{\Gamma}$ in a n-layer Be slab as opposed to n occupied states in the bulk Be.) As discussed above, this SS disappears as hydrogen is adsorbed on the surfaces, resulting in an upward shift in the Fermi energy in the slab calculation.

To determine the position of the bulk Fermi energy, we compare the calculated band structure with the PBS (Fig. 17). This is accomplished by matching the portion of the bulk-like bands below the Fermi level along $\overline{T}'$ and $\overline{T}_2'$ with the PBS (see Fig. 19). Since the width of the bulk-like bands are very close to that of the PBS, the Fermi energy can be accurately determined. We find that the Fermi energy has to be shifted downward by 0.7 eV. The binding energy of the states given above are with respect to this "bulk" Fermi level.

3.2 Charge Density, Potential and Work Function

Contour plots of the self-consistent charge density of the clean Be(0001) surface is shown in Fig. 22(a) in the $(1\bar{1}00)$ plane. The contour pattern is seen to change gradually from the surface to the bulk. This means that the charge density in the first few layers are different from that of the bulk. A clear sign of this difference is the deviation from the symmetric distribution with respect to the reflection operation in the (0001) planes containing the Be atoms, which is a valid symmetry operation in the bulk. This deviation is observed, e.g., in the contour lines between Be atoms in two neighboring layers in Fig. 22(a). The deviation is significantly reduced by covering the surface with a monolayer of H (Fig. 22(b)). The contour lines are now fairly symmetric about the third and fourth Be layers. Thus the charge distribution is partially restored to the variation in the bulk. This mechanism is better seen in Fig. 23(a), where we plotted the charge density averaged parallel to surface, as a function of the distance from the center of the slabs. While the variations in the average charge density in the first couple of layers and in the bulk layers (i.e., near the center of the slab) are quite different for the clean Be slab, they are quite similar for the H-covered slab. The difference between the average charge density for the clean and H-covered surfaces is shown

in Fig. 23(b). The change in the charge density as a result of H adsorption is oscillatory (Friedel oscillation) [42].

In Fig. 24, we show the local part of the self-consistent effective potential averaged parallel to the surface, as a function of the distance from the center of the slab. For the clean surface, we find a gradual increase in the potential near the surface. This is not surprising because the screening of the vacuum potential is inefficient due to the low density of states of bulk Be at the Fermi level [10]. This gradual potential increase disappears upon adsorption of the H overlayer. The average potential of the H-covered Be slab is very much bulk-like immediately below the first Be layer.

The work function of the H-covered Be(0001) is calculated using Eq. (4.3). We obtain a value of 2.7 eV before the adjustment of the Fermi energy discussed above. Taking into account the 0.7 eV adjustment, the work function of this H-covered surface is 3.4 eV, which is about 1.6 eV smaller than that of the clean surface. The work function change can also be obtained from Fig. 24. The average potential of the clean and H-covered surfaces are lined up at the center of the slabs. Since the Fermi level should be fixed with respect to the bulk potential, the difference in the potentials in the vacuum is then the change in the work function. This evaluation also gives us 1.6 eV. To our knowledge, such a large reduction in the work function due to hydrogen adsorption has never been found in other systems.

4. H on Mg(0001)

In this section, the results of our calculation on the clean and H-covered Mg(0001) surface are presented. Magnesium (and its alloys) are considered good

media for reversible storage of H, especially for vehicular applications [43]. A knowledge of the energetics of hydrogen near the Mg surface is important for understanding the adsorption and desorption kinetics of hydrogen. The energetics for hydrogen to go from the surface fcc site into the subsurface octahedral site is determined. We have also calculated the adsorption energy, H—Mg bond length, and the frequency of hydrogen vibration [9]. To our knowledge, there has been no detailed experimental result on hydrogen adsorption on Mg(0001) surfaces. However, the system has been studied theoretically using a jellium model, with the substrate potential included via first-order perturbation theory [7]. We will compare our results with the model calculation [7].

4.1 Calculational Details

The calculational procedure is similar to that described in subsection 2.1. The Wigner interpolation formula [44] is used here for the exchange and correlation potential. We employ a supercell geometry (see Fig. 12) with four Mg layers in the substrate slab. The vacuum space between the slabs is equivalent of four Mg layers (the interlayer distance in Mg is greater than that in Be). Adsorption of hydrogen on the surface will be treated at unit coverage. Plane-wave basis functions are used. The kinetic-energy cutoff is $E_{\max} = 12$ Ry, which amounts to about 850 plane waves at each k-point. The potential difference in the last two iterations is about 1 mRy.

4.2 Clean Mg(0001) Surface

The surface energy and the work function of the Mg(0001) surface are obtained. The surface energy is calculated according to Eq. (4.1). With 12 k-points in ISBZ, we obtain $E_s = 0.33$ eV per surface atom (or 0.59 J/m^2). The result

changes by about 0.01 eV with respect to the number of k-points in ISBZ. A decrease of 0.01 eV is also obtained for the slab which contains six atomic layers (with a vacuum space equivalent to two atomic layers). Surface energy of free-electron-like metals has been evaluated using perturbative and variational techniques [21]. For Mg(0001), a value of 0.66 J/m^2 [45] was obtained, using the Hedin-Lundqvist correlation potential [16]. The Hedin-Lundqvist form gives a greater value for the surface energy than the Wigner interpolation formula [44]. If we use the former, a surface energy of 0.36 eV per surface atom (0.64 J/m^2) is obtained. No direct measurement of the surface energy is available. Comparisons are usually made with the surface tension of the corresponding liquid metal. For Mg, a zero-temperature extrapolation of the experimental surface tension was calculated to be 0.72 J/m^2 [45]. Estimate from Eq. (4.2) with the experimental cohesive energy, $E_{\rm coh}$ = 1.51 eV [22], gives 0.61 J/m^2, in reasonable accord with the calculated values.

Work functions of 3.7—3.8 eV are obtained for Mg(0001) for the four-layer Mg slab with the vacuum space being equivalent of four Mg layers; the variation in the result calculated with the number of k-points in ISBZ from 12 to 25 is ~0.1 eV. The experimental work function for Mg is 3.66 eV [46]. The calculation agrees well with experiment.

4.3 H/Mg(0001): Total Energy Results

Equilibrium position and adsorption energy

Three adsorption sites are studied: the fcc, hcp, and bridge site. The on-top site is not investigated, since our preliminary results indicate it is the most unstable site. The adsorption energy is calculated using Eq. (4.3), with $E_{\rm H}$ = −0.958 Ry.

The calculated adsorption energy as a function of the hydrogen-to-surface distance (height) is shown in Fig. 25. The equilibrium height of H in each site and the adsorption energy at the equilibrium positions are obtained from the polynomial fits, Eq. (4.4). The results are summarized in Table IX. Our result shows that the order of stability of the adsorption sites is fcc > hcp > bridge. The sequence is different from that for H adsorption on Be(0001) (see subsection 2.3). The source of this difference will be discussed in Sec. 5. The calculated values of the adsorption energy is expected to be smaller than the actual values owing to the small E_{max} of 12 Ry. The adsorption of hydrogen on Mg(0001) has been treated theoretically by Hjelmberg [7] using a simplified approach. A single H near the jellium surface (uniform positive charge background abruptly terminated at the surface) was studied. First-order perturbation correction due to the discrete lattice ions (Ashcroft pseudopotential [47]) was then added to the adsorption energy. His results are also tabulated in Table IX. The adsorption energy he obtained for fcc, hcp, and bridge site are all greater than half of the binding energy of H_2, which means it is possible for H_2 to dissociate on the Mg(0001) surface. This question is yet to be resolved because no detailed experiment of hydrogen on magnesium surfaces exists [48]. Regarding the order of stability of the sites, his result is fcc > bridge > hcp. The order of the hcp and bridge site is reversed from ours. This reversed ordering may be unwarranted considering the other irregularities of his results (see below).

Bond length and vibrational frequency

The H—Mg bond lengths are calculated from the equilibrium heights and are tabulated in Table IX. As for H/Be(0001), the bond lengths for the fcc and hcp site are very close. The bond length for the bridge site is smaller by 0.15 Å. The

values are close to the H—Mg bond length in bulk MgH_2 (1.95 Å) [49] but much greater than that of MgH molecule (1.73 Å) [50]. The bond lengths obtained by Hjelmberg (Table IX) for the fcc and hcp site are different by 0.05 Å. They are also greater than our values, especially for the hcp site. Instead of being close to that for the fcc site as most studies have shown (see, e.g., Ref. 4 and 8), his equilibrium height for the hcp site is the same as for the bridge site.

The frequencies of hydrogen vibration perpendicular to the surface are calculated as in subsection 2.4. The frequency for the fcc and hcp site are very close (which is also true for Be [8] and Ru [4]), while it is greater by nearly 20 meV for the bridge site. The values are smaller than the corresponding result for H/Be(0001), which should be expected since H—Mg bond lengths are greater than H—Be bond lengths. The results obtained by Hjelmberg are quite different from ours. His calculation shows that the frequency for the fcc and hcp site differs by 30 meV. The frequency for the bridge site is much (50%) greater than our value. The different result on the bond lengths (equilibrium heights) and the hydrogen vibrational frequencies suggest certain inadequacy of the jellium model [7] in quantitative predictions.

Subsurface octahedral site

The adsorption energy of hydrogen is calculated for a monolayer of hydrogen along the straight line connecting the fcc site and the subsurface octahedral site. The variation of the adsorption energy is shown in Fig. 26. The energy minimum under the surface layer occurs near the six-fold octahedral site (indicated by the arrow in Fig. 26). The subsurface site is unstable compared to the surface fcc site, but the energies differ by 0.26 eV only, much smaller than that for H/Be(0001) (1.4 eV, see subsection 2.5). The energy barrier for hydrogen to go below the surface

is 0.65 eV, which is also much smaller than that for H/Be(0001) (1.6 eV). The energy barrier for hydrogen to move to the surface from the subsurface octahedral site is 0.4 eV.

Hjelmberg [7] again derived results very different from ours. The energy is at a maximum near the subsurface octahedral site in his calculation (Fig. 5 of Ref. 7). On the other hand, a minimum was obtained near the tetrahedral site. The potential well near the subsurface octahedral site has been found in other studies (e.g., Refs. 4 and 8).

4.4 Charge Density and Work Function

Contour plots of the self-consistent charge density in the $(11\bar{2}0)$ plane is shown in Fig. 27(a) for the clean surface. The results are for the slab containing four Mg layers. The charge density is in units of e/Ω, where e is the electronic charge and $\Omega = 186$ Å^3 is the supercell volume. The valence charge distributes smoothly over the clean surface. The charge distribution in the second layer closely resembles that of the bulk [51]. The self-consistent charge density for the surface covered with a monolayer of H at the calculated equilibrium position in the fcc site is shown in Fig. 27(b). Fig. 27(c) is a plot of the charge-density difference between the H-covered and clean Mg(0001) surface, subtracting the charge density of an isolated monolayer of H in the fcc adsorption position, which is calculated with the same parameters as for the clean and H-covered surface. Since the charge-density difference is positive around the H atoms, it indicates that H pulls charge from its surroundings. To give an estimate of the charge acquired by H on its adsorption, we calculate the charge within an "ion sphere" of radius 2.4 a.u. (1.27 Å), which roughly covers all closed contour lines around H (Fig. 27(b)). The charge

within the sphere is 1.50 e for H in the fcc site. (A charge of 1.49 e is obtained for H in the hcp and bridge site if the same sphere is used.) We calculated the charge within the same sphere around the fcc site on the clean surface and obtain 0.50 e (0.51 e at the hcp site and 0.44 e at the bridge site). We also performed self-consistent calculations for an isolated hexagonal monolayer of H (a = 3.21 Å as for the substrate) using the same parameters. The charge within a sphere of radius 2.4 a.u. around H is 0.73 e. This means that the charge within the sphere around the H increases by 0.27 e as the H is adsorbed in the fcc site. We note that the charge of an exact H-1s orbital within a sphere of radius 2.4 a.u. is 0.86 e (slightly smaller value is obtained in local-density approximation), greater than the value for H monolayer (0.73). The increase in the charge around H is thus 0.14 e if comparison is made with the clean surface and H atom. In Fig. 28(a), the charge density averaged parallel to the surface is shown as a function of the distance perpendicular to the surface, for the clean and H-covered surface (fcc site). The charge difference (Fig. 28(b)) shows an oscillatory behavior along the normal of the surface. Such density oscillations are due to electronic screening of the H potential and have been found in case of H impurity in jellium and simple metals [39–41].

The work function for Mg(0001) covered with a monolayer of H at the calculated equilibrium positions are determined. Calculations are carried out using different k-point sets. The change in the work function from the clean surface is summarized in Table IX. Our results show slight decrease in the work function for monolayer of H in fcc and hcp site, and a slight increase for a H monolayer in the bridge site. We have also calculated the work function changes from the changes in the surface dipole moment, using a double-layer model. Although it may not

be very accurate because of the oscillatory behavior (Fig. 28(b)), values of similar magnitude are obtained.

5. Discussions and Conclusions

We would first like to discuss some total-energy results in terms of the effective medium theory [52,53]. At the present, first-principles calculation for surfaces is still quite difficult computationally. The effective medium theory, although approximate, is a simple approach and can help to understand some results, at least qualitatively. To the first approximation, the adsorption energy of an adsorbate is obtained by considering the adsorbate in a homogeneous electron gas (jellium) whose density is equal to some average of the substrate charge density around the adsorbate. For H, this energy is minimized at an effective charge density of 0.01 a.u. [53]. In our first-principles calculation, we find the clean Be(0001) charge density at the equilibrium H adsorption positions to be 0.015 a.u. at the fcc and hcp site, 0.014 a.u. at the bridge site, and 0.006 a.u. at the on-top site. The charge density at the lowest energy equilibrium positions are thus quite similar ($\sim$ 0.015 a.u.), which indicates that H seeks a position at which the substrate charge density has a particular value. But this preferred charge density value is quite different from 0.01 a.u. Since the on-top site has too low a charge density, it is generally unstable compared to the other three surface adsorption sites according to the effective medium theory. The density at the subsurface octahedral and tetrahedral site is found to be 0.031 and 0.042 a.u., respectively. These values are much greater than those at the surface sites. Thus the subsurface sites are unstable compared to the surface sites. For H/Mg(0001), we obtain 0.008 a.u. at the surface fcc and hcp site, 0.007 a.u. at the bridge site, and 0.010 and 0.015 a.u.

at the subsurface octahedral and tetrahedral site, respectively. Here the preferred charge density ($\sim$ 0.008 a.u.) is closer to the predicted 0.01 a.u. We note that the charge density at the subsurface octahedral site is slightly larger than the surface site values; the energy difference between the subsurface octahedral site and surface site should thus be smaller in comparison with H/Be(0001), which agrees with our first-principles result. Notice that for both Be(0001) and Mg(0001), the subsurface tetrahedral site has a higher charge density, and should thus be unstable compared to the octahedral site.

We have found that hydrogen prefers the bridge site to the fcc site on Be(0001) surface, while it prefers the fcc site to the bridge site on Mg(0001). Since Be and Mg are isoelectronic and crystallize in the same hcp structure, it is of interest to see how the different order of stability have come about. We first examine the effect of various energy components on the order of stability. The difference in energy components between hydrogen adsorption in the bridge site and in the fcc site are calculated. Results for H/Be(0001) and H/Mg(0001) are compared in Table X. We first look at the sum of electron-ion interaction energy, Hartree energy, and Ewald energy (see Chapter II). This term represents the electrostatic energy of the system (only the local part of ion potential included). Comparing this term for the two sites, we find that it favors the fcc site over the bridge site for both H/Be(0001) and H/Mg(0001). The kinetic energy is lower for the fcc site in case of H/Be(0001) and for the bridge site in case of H/Mg(0001). These favorable sites of the kinetic energy are opposite of the stable adsorption sites. The exchange-correlation energy is lower for the fcc site in both cases. The nonlocal energy (interaction between electrons and nonlocal part of the ionic potential) makes a significantly larger contribution to the total energy for the adsorption in

the bridge site than in the fcc site of Be(0001) and thus making the bridge site favorable over the fcc site. The nonlocal energy for the two sites of Mg(0001), on the other hand, is not different enough to do so. Thus the nonlocal energy is essential for the stability of the bridge site occupation in case of H/Be(0001). The nonlocal pseudopotential in both cases is the difference of the p-potential from the s-potential, $V_p - V_s$, of the substrate atoms. (The nonlocal d-potential is not generated since its effect is expected to be negligible.) Because of the lack of orthogonality with the core state (there is no p orbital in the Be core), the p-potential is very attractive. Magnesium, on the other hand, does have a $2p$ core state, resulting in a less attractive p-potential. The different pseudopotentials of Be and Mg are shown in Fig. 29. To substantiate the above analysis, we have repeated the calculations by using the local potential only (i.e., by letting $V_p = V_s$). With H in its original equilibrium positions at the bridge and fcc site, the total energy of H/Be(0001) is re-computed. The result shows that the fcc site is lower in energy (by 0.2 eV/atom) than the bridge site when the nonlocal potential is neglected, thus confirming the above conjecture that the p-potential is responsible for the bridge site being the stable adsorption site for H/Be(0001).

In subsection 3.1, we found a strong Be-$p_{x,y}$—H-s bonding band along $\overline{T}_2'$. From our discussions there, it is clear that the existence and the split-off energy of a bonding band depends strongly on which adsorption site hydrogens occupy. Thus from the band structure viewpoint, it can be said that the bonding band is significant in deciding which site is stable. In fact, we find the sum of eigenvalues for H in the bridge site of Be(0001) is lower than for H in the fcc site by 0.2 eV per H in the six-layer (four Be-layers and two H-layers) slab calculation. Our preliminary band structure for Be(0001) covered with a monolayer of H in the fcc site shows a

bonding band near the zone boundary with smaller split-off energy. This picture does not contradict the above energy analysis; both signify the involvement of the Be-*p* orbitals.

Beside the split-off band along $\overline{T}_2'$, another interesting feature which we have found in H/Be(0001) with H in the bridge site is the split-off state at $\overline{\Gamma}$. The state is only 0.2 eV below the valence band edge. Such a state has previously been found in theoretical calculation of H impurity in jellium [39,40] but not for H adsorption on metal surfaces [41]. Since this is not a strong H—Be bonding state, it is possible that it exists for H adsorbed on other simple metal surfaces such as Mg(0001).

In conclusion, we have performed total energy and electronic structure calculations on H adsorption on Be(0001) and Mg(0001) surfaces. The adsorption energy, H—Be and H—Mg bond lengths, frequency of H vibration normal to the surfaces are determined. Among the symmetry adsorption sites, the bridge site is found to be the stable adsorption site for H/Be(0001). This result and the calculated vibrational frequency of H agree well with an EELS experiment [6]. For H/Mg(0001), the fcc site is found to be the stable site. The different stable adsorption site in the two cases is the consequence of the different *p*-potentials. The energetics for H to go into the subsurface octahedral site is investigated. In both cases, we find that the subsurface site is higher in energy compared to surface sites. Our total energy results of H/Mg(0001) suggest that the jellium-type theory [7] may not give accurate results even for H on the surfaces of free-electron-like metals such as Mg. Electronic band structure is obtained for clean Be(0001) and Be(0001) covered with a monolayer of H in the bridge site. The band structure undergoes dramatic change upon the adsorption of hydrogen. The interesting and

important features of the H-covered surface are a shallow split-off state at $\overline{\Gamma}$ and a Be-$p_{x,y}$—H-s bonding band near parts of the zone boundary. The adsorption of H on Be(0001) tends to heal the Be(0001) surface and results in a large reduction. (1.6 eV) in the work function. Small change ($\sim$ 0.1 eV) in the work function is found upon adsorption of H on Mg(0001).

References for Chapter IV

[1] M. Weinert, A. J. Freeman, and S. Ohnishi, 1986, Phys. Rev. Lett. **56**, 2295 (1986); R. Biswas and D. R. Hamann, Phys. Rev. Lett. **56**, 2291 (1986).

[2] C. Umrigar and J. W. Wilkins, Phys. Rev. Lett. **54**, 1551 (1985).

[3] D. Tomanek, S. G. Louie, and C. T. Chan, Phys. Rev. Lett. **57**, 2594 (1986).

[4] M. Y. Chou and J. R. Chelikowsky, Phys. Rev. Lett. **59**, 1737 (1987).

[5] J. Paul, Phys. Rev. B **37**, 6164 (1988); R. B. Murphy, J. M. Mundenar, K. D. Tsui, and E. W. Plummer, Bull. Am. Phys. Soc. **33**, 655 (1988).

[6] K. B. Ray and E. W. Plummer, Bull. Am. Phys. Soc. **33**, 655 (1988).

[7] H. Hjelmberg, Surf. Sci. **81**, 539 (1979).

[8] R. Yu and P. K. Lam, Phys. Rev. B **39**, 5035 (1989).

[9] P. K. Lam and R. Yu, in *Proceedings of International Meeting on Advanced Materials, Symposium I: Hydrogen Absorbing materials*, Materials Research Society, Tokyo, 1988.

[10] M. Y. Chou, P. K. Lam, and M. L. Cohen, Phys. Rev. B **28**, 417 (1983); M. Y. Chou, P. K. Lam, and M. L. Cohen, Solid State Commun. **42**, 861 (1982).

[11] K. M. Mackay, *Hydrogen Compounds of the Metallic Elements* (Spon, London, 1966), Chapter 4.

[12] G. S. Smith, Q. C. Johnson, D. K. Smith, D. E. Cox, R. L. Snyder, R.-S. Zhou, and A. Zalkin, Solid State Commun. **67**, 491 (1988).

[13] P. S. Bagus, H. F. Schaefer, and C. W. Bauschlicher, J. Chem. Phys. **78**, 1390 (1983); C. W. Bauschlicher, P. S. Bagus, and H. F. Schaefer, IBM J. Res. Develop. **22**, 213 (1978).

[14] G. Angonoa, J. Koutecky, A. N. Ermoshkin, and C. Pisani, Surf. Sci. **138**, 51 (1984).

[15] G. Angonoa, J. Koutecky, and C. Pisani, 1982, Surf. Sci. **121**, 355 (1982).

[16] L. Hedin and B. I. Lundqvist, J. Phys. C **4**, 2064 (1971).

[17] M. L. Cohen, M. Schlüter, J. R. Chelikowsky, and S. G. Louie, Phys. Rev. B **12**, 5575 (1975); M. Schlüter, J. R. Chelikowsky, S. G. Louie, and M. L. Cohen, Phys. Rev. B **12**, 4200 (1975).

[18] K. J. H. Mackay and N. A. Hill, J. Nucl. Mater. **8**, 263 (1963).

[19] M. A. Van Hove and S. Y. Tong, *Surface Crystallography by LEED* (Springer, New York, 1979), p. 253.

[20] M. Y. Chou and J. R. Chelikowsky, Phys. Rev. B **35**, 2124 (1987), and references therein.

[21] See N. D. Lang, in *Theory of the Inhomogeneous Electron Gas*, edited by S. Lundqvist and N. H. March (Plenum, New York, 1983), p. 309.

[22] C. Kittel, *Introduction to Solid State Physics*, 6th ed. (Wiley, New York, 1986), p. 55.

[23] V. S. Fomenko, *Handbook of Thermionic Properties* (Plenum, New York, 1966), p. 6.

[24] A. K. Green and E. Bauer, Surf. Sci. **74**, 676 (1978).

[25] J. C. Boettger and S. B. Trickey, Phys. Rev. B **32**, 1356 (1985).

[26] E. Wimmer, J. Phys. F **14**, 681 (1984).

[27] J. P. Perdew and A. Zunger, Phys. Rev. B **23**, 5048 (1981).

[28] The experimental binding energy of a H_2 molecule is $E_b = 4.48$ eV. If our calculated E_{ad} is compared to this value, dissociation of H_2 would occur.

The calculated adsorption energy, however, is too sensative to the energy of H atom used for the comparison to be valid.

[29] J. J. Hurd, and R. O. Adams, J. Vac. Sci. Technol. **5**, 183 (1968); Ref. 6.

[30] J. P. Muscat, Phys. Rev. B **33**, 8136 (1986).

[31] R. Yu and P. K. Lam, Phys. Rev. B **38**, 3576 (1988). Calculation was performed for the perovskite structure. The actual structure has not yet been determined.

[32] R. Colin and D. DeGraf, Can. J. Phys. **53**, 2142 (1975).

[33] From our experience with previous calculations, the equilibrium distance is accurate within a few percent even at low cutoff energy. Furthermore, the change in the adsorption energy resulting from the change of equilibrium distance is small in this case. For instance, even if h_0 changes by 0.1 a.u., the energy changes only by 10 meV for the bridge site as estimated from the calculated frequency. Therefore, it is valid to compare the differnece in the adsorption energy between two sites calculated at these fixed positions only.

[34] B. Dutta, S. K. Sarkar, and D. Roy, Phys. Status Solidi **132**, 345 (1985). Three-body forces have to be included to explain the bulk phonen spectrum. However, based on our result, the resulting phonon frequency for the oscillation of the adsorbed hydrogen is insensitive to the two-body force constants, hence the three-body forces between the substrate Be atoms are not likely to make a large contribution to the frequency of hydrogen oscillation.

[35] U. O. Karlsson, S. A. Flodström, R. Engelhardt, and W. Gädeke, Solid State Commun. **49**, 711 (1984).

[36] R. A. Bartynski, E. Jensen, T. Gustafsson, and E. W. Plummer, Phys. Rev. B **32**, 1921 (1984).

[37] E. V. Chulkov, V. M. Silkin, and E. N. Shirykalov, Surf. Sci. **188**, 287 (1987).

[38] J. C. Boettger and S. B. Trickey, Phys. Rev. B **34**, 3604 (1986).

[39] C. O. Almbladh, U. von Barth, Z. D. Popovic, and M. J. Stott, Phys. Rev. B **14**, 2250 (1976); P. Jena and K. S. Singwi, Phys. Rev. B **17**, 3518 (1978).

[40] J. K. Norskov, Phys. Rev. B **20**, 446 (1979).

[41] See J. K. Norskov, Solid State Commun. **24**, 691 (1977).

[42] J. Friedel, Phil. Mag. **43**, 153 (1952).

[43] P. Selvam, B. Viswanathan, C. S. Swamy, and V. Srinivasan, Int. J. Hydrogen Energy **11**, 169 (1986).

[44] E. Wigner, Phys. Rev. **46**, 1002 (1934); D. Pines, *Elementary Excitations in Solids* (Benjamin, New York, 1963).

[45] See Table 2 of Ref. 21.

[46] H. B. Michaelson, J. Appl. Phys. **48**, 4729 (1977).

[47] N. W. Ashcroft, Phys. Lett. **23**, 48 (1966).

[48] An ultra-violet photoemission experiment on H on Mg performed at room temperature showed no sign of adsorption by either atomic or molecular hydrogen; see S. A. Flodström, L.-G. Petersson, and S. B. M. Hagström, J. Vacuum Sci. Technol. **13**, 280 (1976).

[49] F. H. Ellinger, C. R. Holley, Jr., B. B. McInteer, D. Pavone, R. M. Potter, E. Staritzsky, and W. H. Zachariasen, J. Am. Chem. Soc. **77**, 2647 (1955).

[50] D. E. Gray (ed.), *American Institute of Physics Handbook*, 3rd ed. (McGraw-Hill, New York, 1972).

[51] M. Y. Chou and M. L. Cohen, Solid State Commun. **57**, 785 (1986).

[52] J. K. Norskov and N. D. Lang, Phys. Rev. B **21**, 2131 (1980); J. K. Norskov, Phys. Rev. Lett. **48**, 1620 (1982); Phys. Rev. B **26**, 2875 (1982).

[53] P. Nordlander, Surf. Sci. **136**, 59 (1984).

Table V. Surface energy (eV per surface atom) and work function (eV) of Be(0001) surface calculated using different slabs (number of Be layers) and vacuum sizes (in units of the interlayer distance of the substrate). E_{max} = 20 Ry and 12 k-points in the irreducible Brillouin zone are used.

Be layers	Vacuum size	Surface energy	Work function
4	6	0.60	5.1
4	8	0.59	5.2
6	4	0.62	4.8
6	6	0.62	4.9

Table VI. Calculated hydrogen adsorption energy, equilibrium distance of hydrogen from the Be(0001) surface, the Be—H bond length, and the frequency of hydrogen.

adsorption site	E_{ad} (eV)	h_0 (Å)	d (Å)	$h\nu$ (meV)
bridge	−2.39	0.98	1.51	168 (178[a])
fcc	−2.30	0.93	1.61	140
hcp	−2.21	0.94	1.62	137
on-top	−1.67	1.42	1.42	197

[a] Effect of substrate motion included.

Table VII. Calculated and experimental binding energy (in eV) of the surface states of Be(0001). Our calculation and that of Chulkov *et al.* (1987) are performed on a ten-layer slab. Result of Boettger and Trickey (1986) is for a three-layer slab.

Surface states	$\overline{\Gamma}$	$\overline{M}$ (upper)	$\overline{M}$ (lower)
Experiment	2.8[a]	1.8 ± 0.1[b]	3.0 ± 0.1[b]
	2.8 ± 0.1[b]		
Present work	2.6	1.9	3.0
Chulkov *et al.* (1987)	2.6	1.9	2.9
Boettger and Trickey (1986)	2.0	—	—

[a] Karlsson *et al.* (1984).

[b] Bartynski *et al.* (1985).

Table VIII. Binding energy and angular-momentum components (in number of electrons) of the surface states of Be(0001) covered with a monolayer of H in the bridge site. Angular-momentum decompositions are made within spheres of radius of 2.36 a.u. (Wigner-Seitz radius) at the surface and second-layer Be atoms and within a sphere of radius 2.40 a.u. (ionic radius) at a H atom.

Surface State	E_b	Surface Be			Second-layer Be			H		
		s	$p_{x,y}$	p_z	s	$p_{x,y}$	p_z	s	$p_{x,y}$	p_z
$\overline{\Gamma}$	11.4	0.20	0.0	0.0	0.12	0.0	0.0	0.15	0.0	0.0
$\overline{M}_2$ (lower)	6.0	0.0	0.32	0.0	0.01	0.02	0.01	0.26	0.0	0.04
$\overline{K}$	3.8	0.01	0.25	0.0	0.0	0.02	0.01	0.32	0.0	0.03
$\overline{M}$ (resonance)	3.6	0.12	0.11	0.02	0.02	0.01	0.01	0.25	0.04	0.01
$\overline{M}$	2.8	0.01	0.07	0.08	0.04	0.12	0.0	0.14	0.03	0.0
$\overline{M}_2$ (upper)	−1.0	0.10	0.01	0.0	0.09	0.01	0.04	0.08	0.06	0.0

Table IX. Calculated adsorption energy, equilibrium distance from the Mg(0001) surface, the Mg—H bond length, vibrational excitation energy, and change in work function for hydrogen in the symmetry adsorption sites on Mg(0001). For comparison, results of jellium-model calculation of Hjelmberg (1979), where the substrate potential is included via first-order perturbation theory, are also given.

adsorption site	E_{ad} (eV)	h_0 (Å)	d (Å)	$h\nu$ (meV)	$\Delta\phi$
		Present work			
fcc	−1.9	0.91	2.07	91	−0.1
hcp	−1.8	0.94	2.08	92	−0.2
bridge	−1.7	1.08	1.93	109	0.1
		Hjelmberg's calculation			
fcc	−2.7	1.01	2.12	80	
hcp	−2.5	1.11	2.17	110	
bridge	−2.6	1.11	1.96	150	
on-top	−2.2	1.75	1.75	200	

Table X. Difference in energy components between bridge and fcc site adsorption for H on Be(0001) and Mg(0001) in eV per H atom (a negative value means bridge site has lower energy).

Energy components	H/Be(0001)	H/Mg(0001)
Ionic + Hartree + Ewald	0.18	0.21
Kinetic energy	0.28	−0.13
Exchange-correlation energy	0.05	0.13
Nonlocal energy	−0.59	−0.02
Total energy	−0.08	0.19

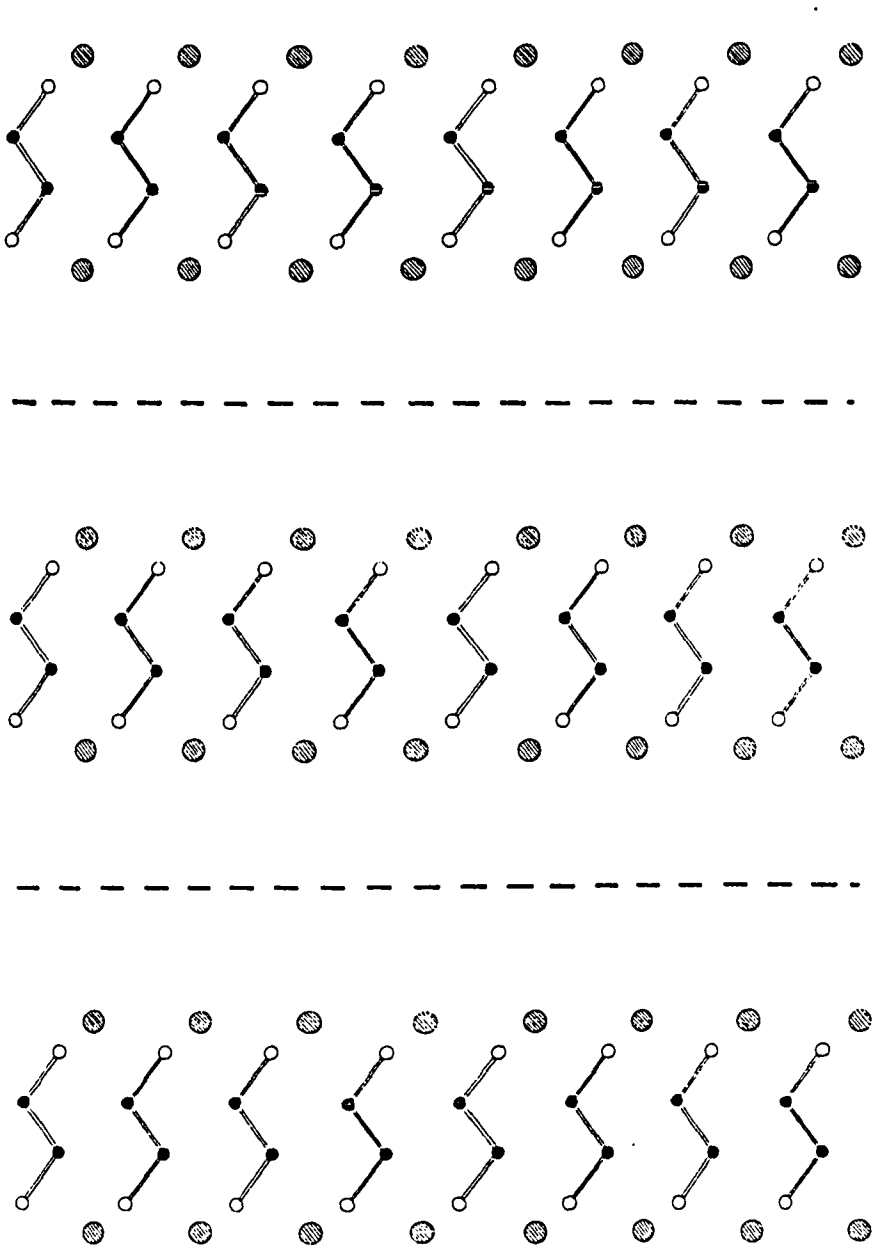

Fig. 12. Supercell geometry for surface calculations on (hydrogen adsorption on) the (0001) surface of hcp metals. The substrate slab consists of four layers of substrate atoms (open and darkened spheres) and one hydrogen layer (hatched spheres) is adsorbed on every surface. The atoms shown are in the $(11\bar{2}0)$ plane of the substrate (H is in the fcc site). The dimension of the unit cell perpendicular to the surface is the distance between the dashed lines.

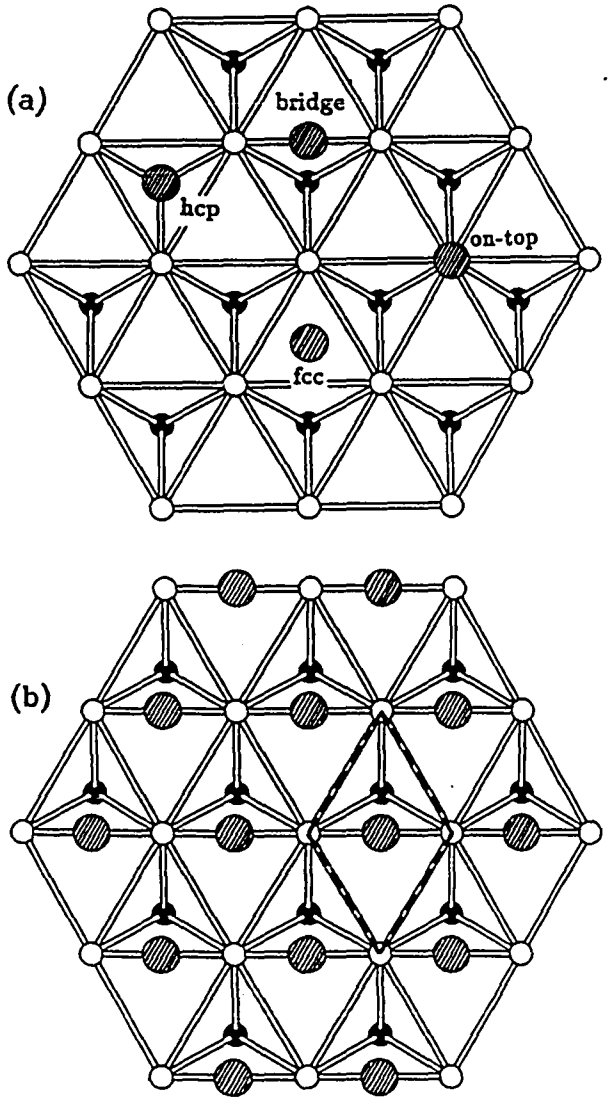

Fig. 13. (a) Top view of a section of the (0001) surface of a hcp metal and the high-symmetry adsorption sites. Open spheres are surface atoms and darkened spheres second layer substrate atoms. The H atoms are the hatched spheres, shown in different adsorption sites (above the surface atomic layer); (b) A $p(1 \times 1)$ H lattice with H in the bridge sites. The dashed lines along the surface Be—Be bonds indicate the two-dimensional unit mesh.

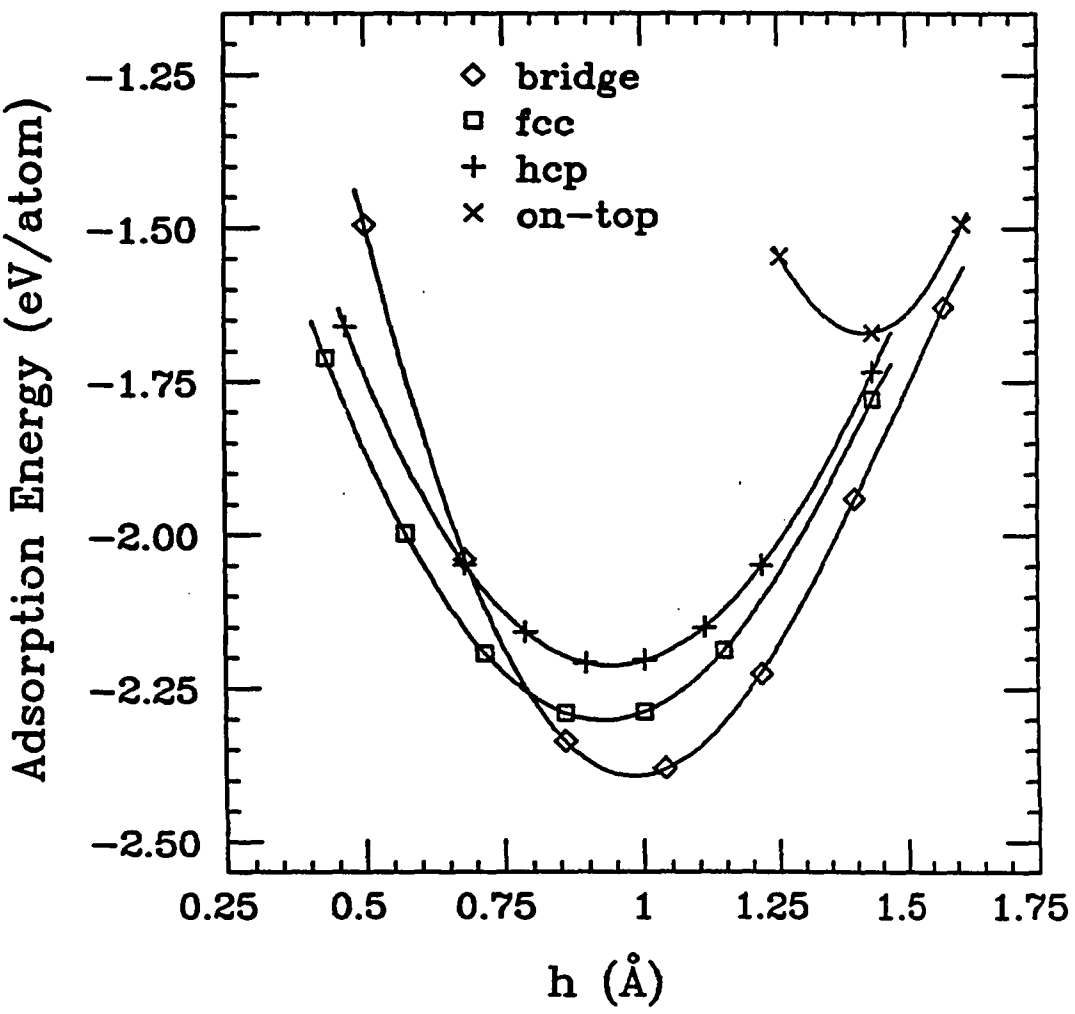

Fig. 14. Calculated adsorption energy of H at different surface sites on Be(0001) as a function of vertical distance between H and the surface Be layer.

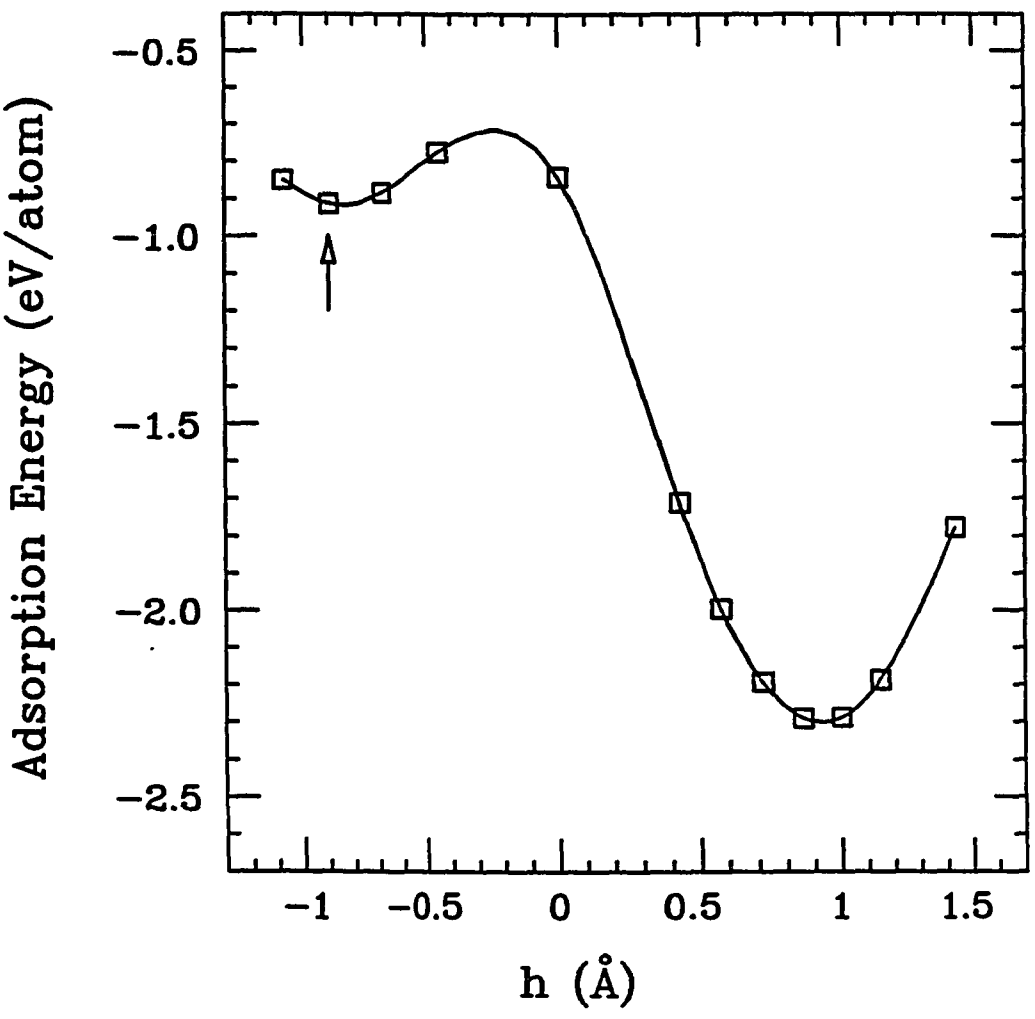

Fig. 15. Calcualted adsorption energy as a function of the coordinate of H perpendicular to the Be(0001) surface, for H along the path which connects the subsurface octahedral site (indicated by an arrow) and the surface fcc site. The origin is at the surface Be layer.

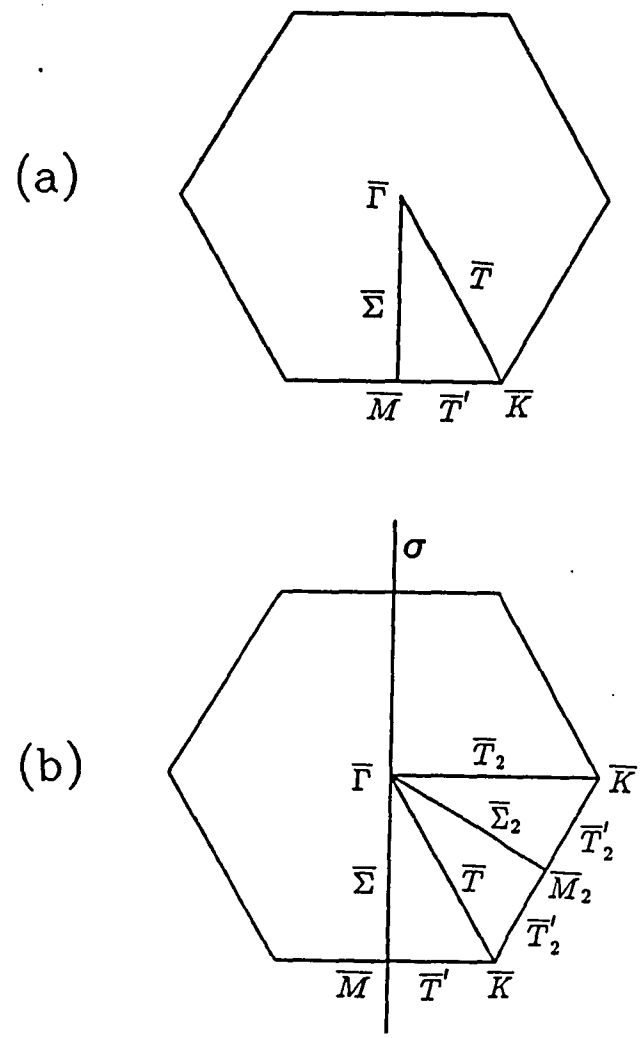

Fig. 16. Surface Brillouin zone for (a) clean Be(0001) surface and (b) Be(0001) surface covered with a monolayer of H in the bridge site. The labelled regions are the irreducible part of the Brillouin zone. The vertical line in (b) is the only existing reflection plane (perpendicular to the surface). The subscript 2 is used to differentiate from points and lines which are labelled without subscripts.

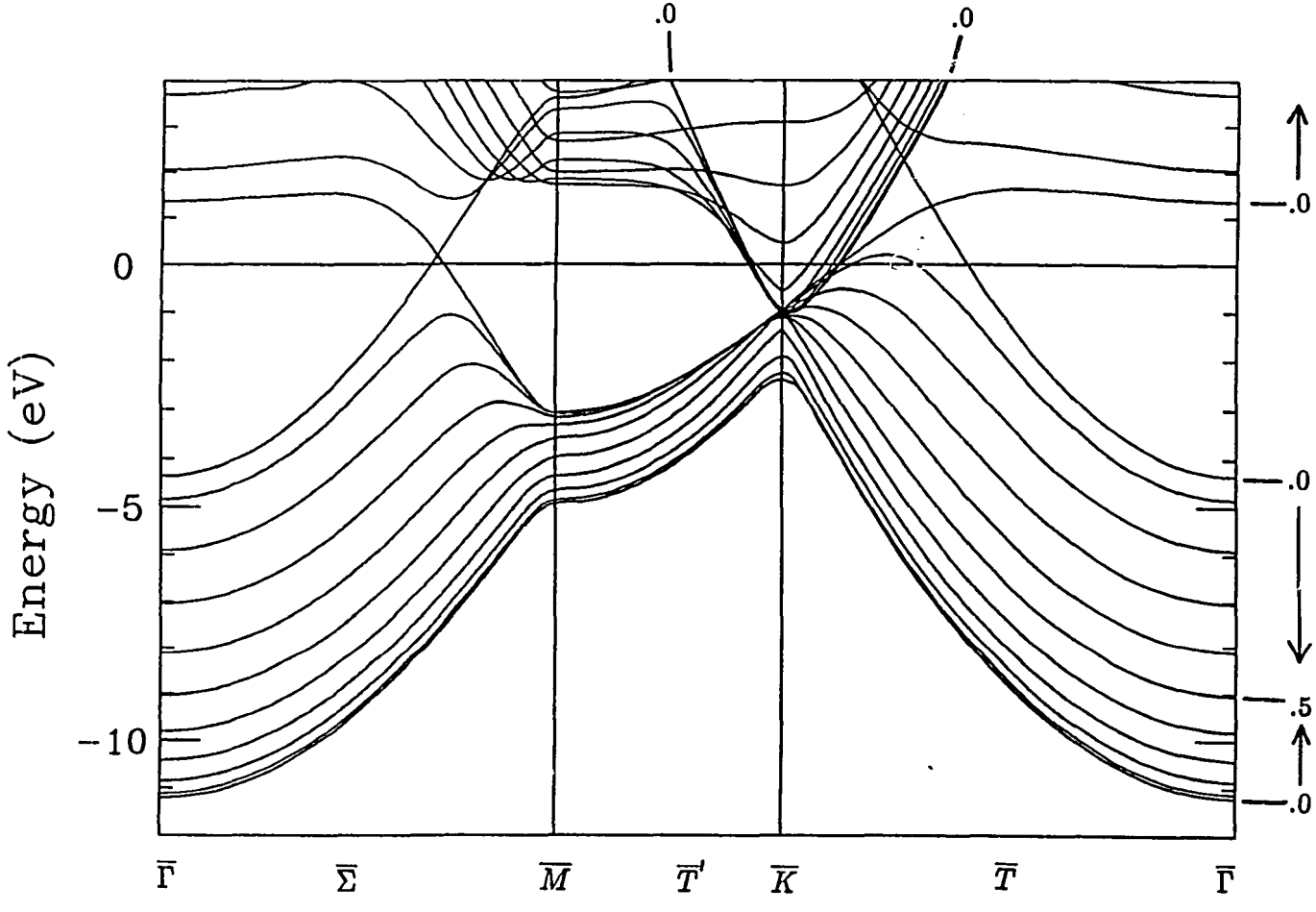

Fig. 17. Bulk band structure of Be projected onto the surface Brillouin zone of Be(0001). The bands are for $k_z = 0$, 0.1, 0.2, 0.3, 0.4, 0.5 in units of $2\pi/c$. The labels on the right and top are k_z values. The arrows point to increasing k_z values.

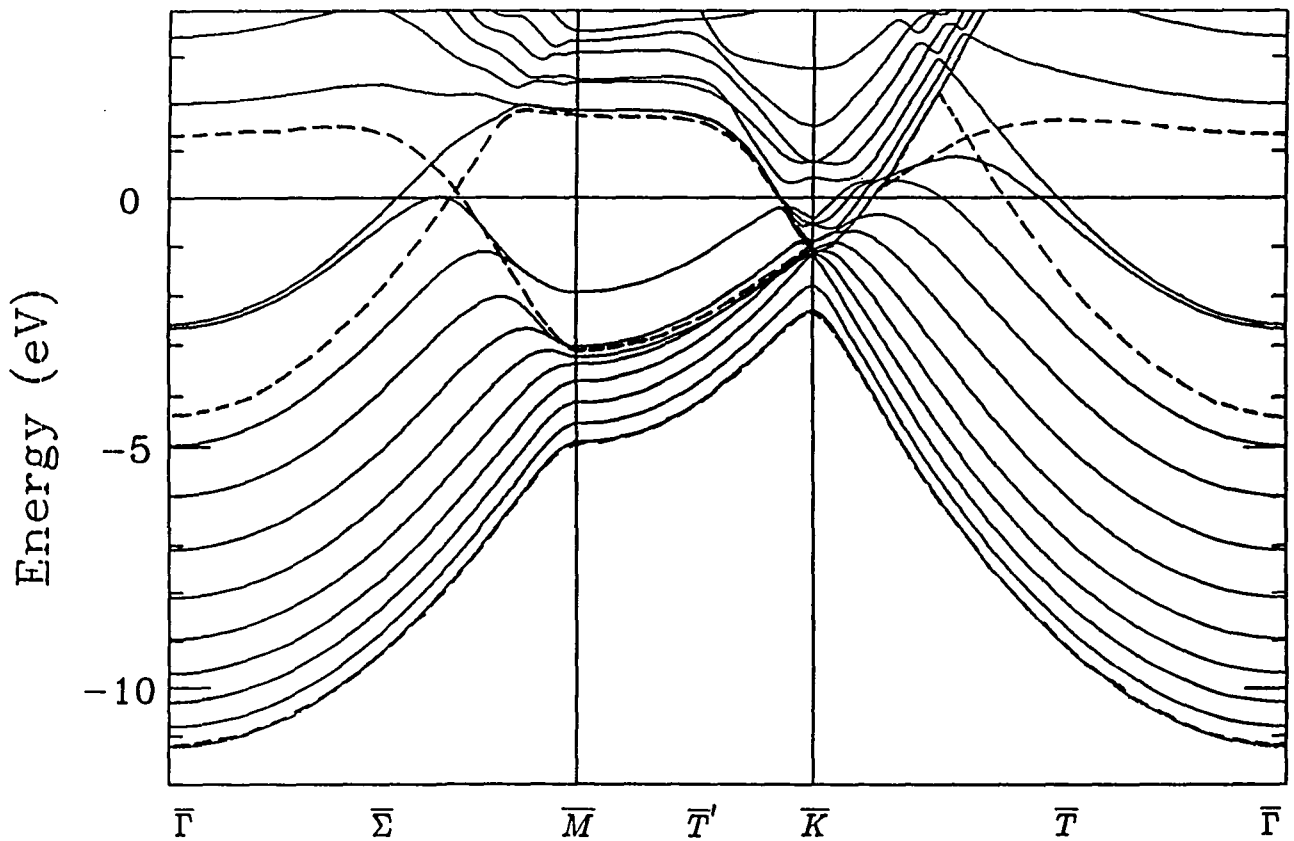

Fig. 18. Calculated band structure of clean Be(0001) surface. The dashed lines mark the boundaries of the bulk projected band structure.

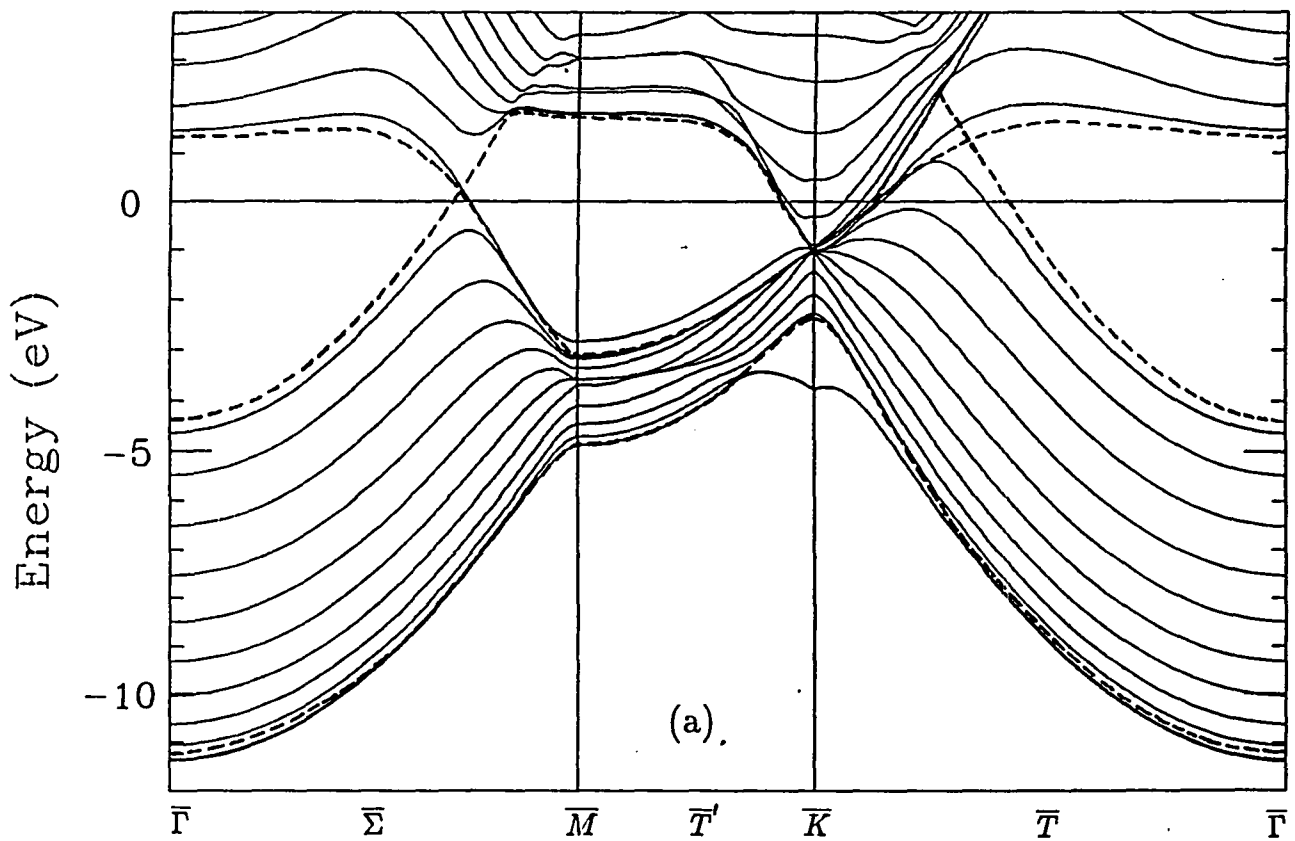

Fig. 19(a). Calculated band structure for the Be(0001) covered with a monolayer of H in the bridge site along $\overline{\Sigma}, \overline{T}', \overline{T}$.

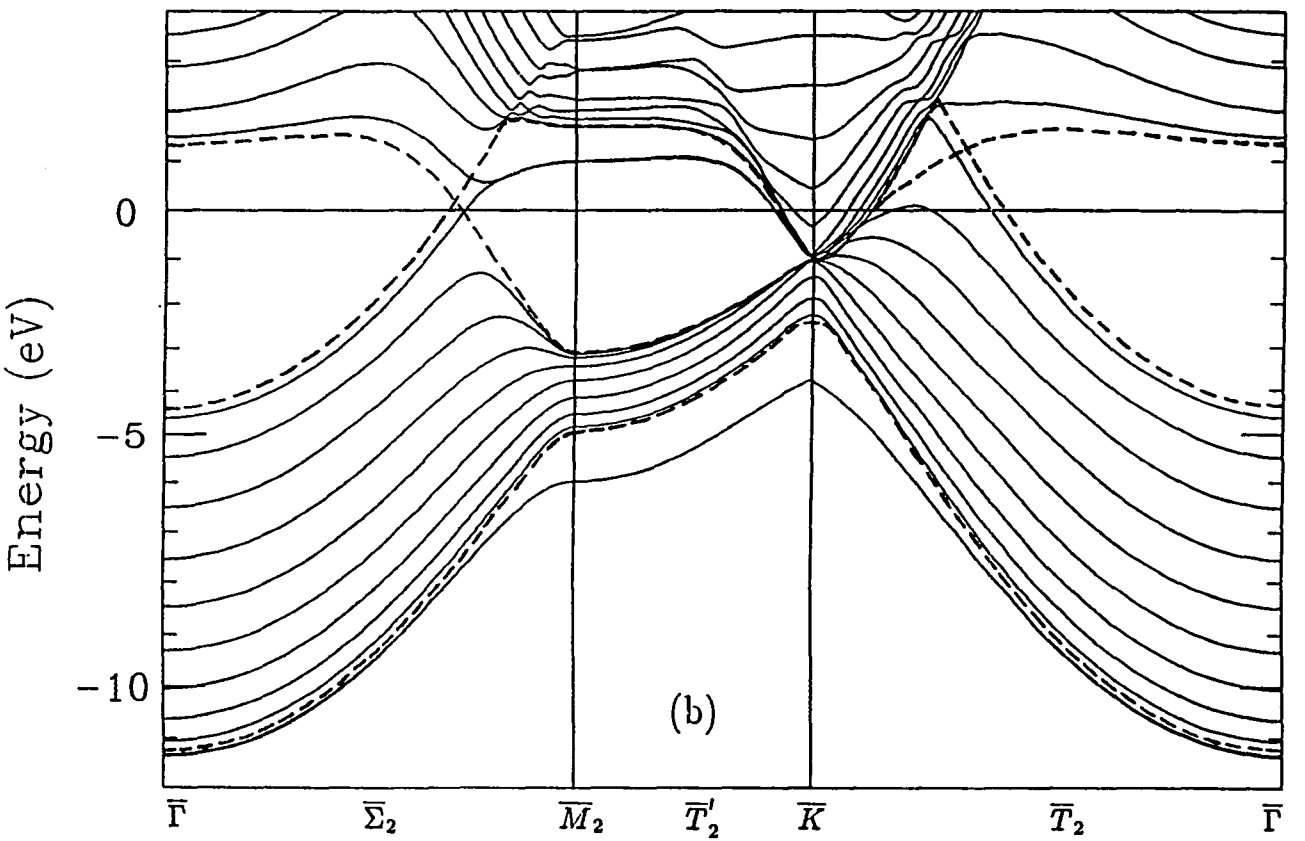

Fig. 19(b). Calculated band structure for the Be(0001) covered with a monolayer of H in the bridge site along $\overline{\Sigma}_2, \overline{T}_2', \overline{T}_2$.

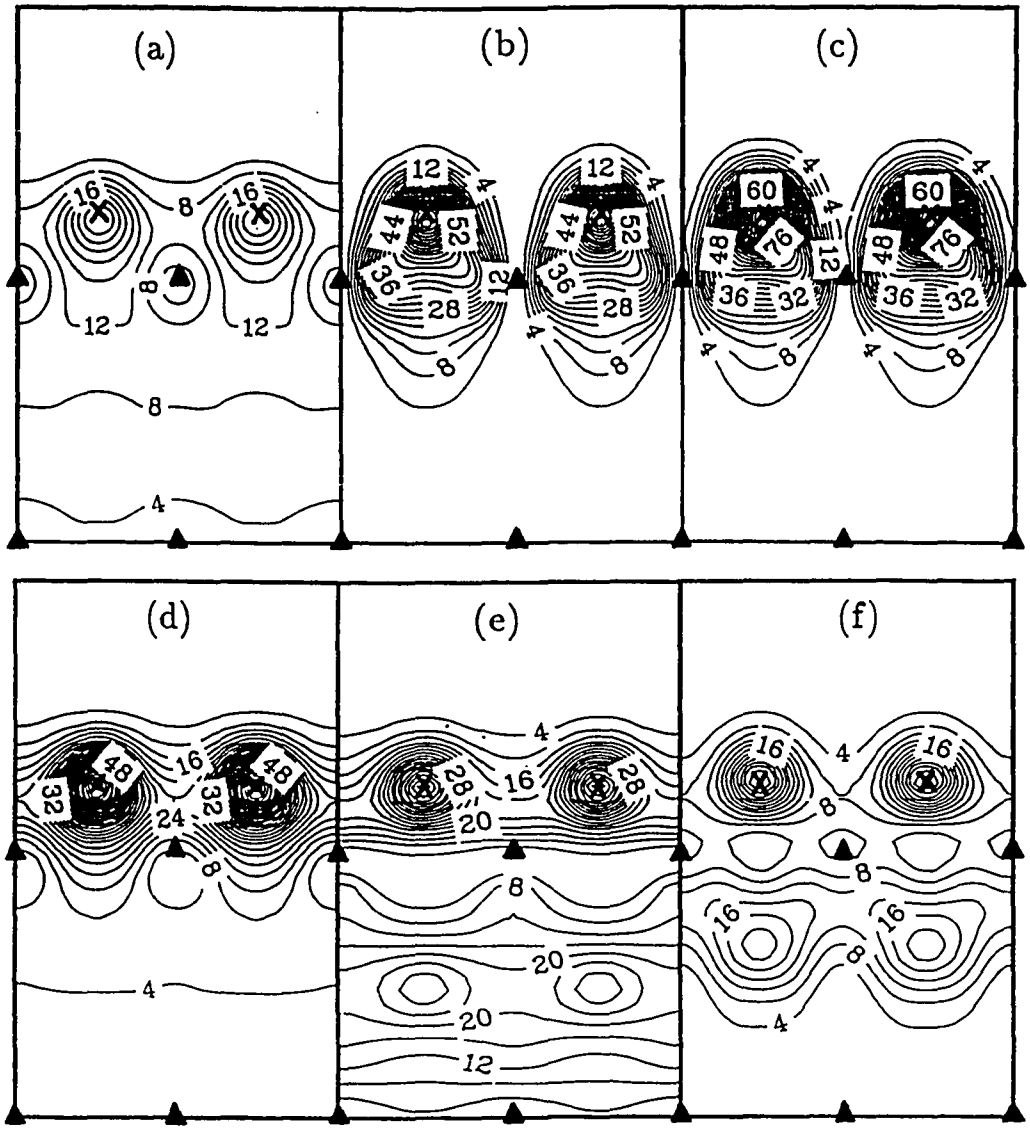

Fig. 20. Contour plot of charge density in $(1\bar{1}00)$ plane of the surface states of Be(0001) covered with a monolayer of H in the bridge site. The charge density shown is the sum of symmetric and antisymmetric states, in units of $8.8 \times 10^{-3}\ e/\text{Å}^3$. The solid triangles indicate the positions of Be atoms (in surface layer and the third layer) and crosses the positions of H atoms. (a) Surface state (SS) at $\overline{\Gamma}$, (b) lower SS at $\overline{M}_2$, (c) SS at $\overline{K}$, (d) resonance at $\overline{M}$, (e) SS at $\overline{M}$, and (f) SS at $\overline{M}_2$ (unoccupied).

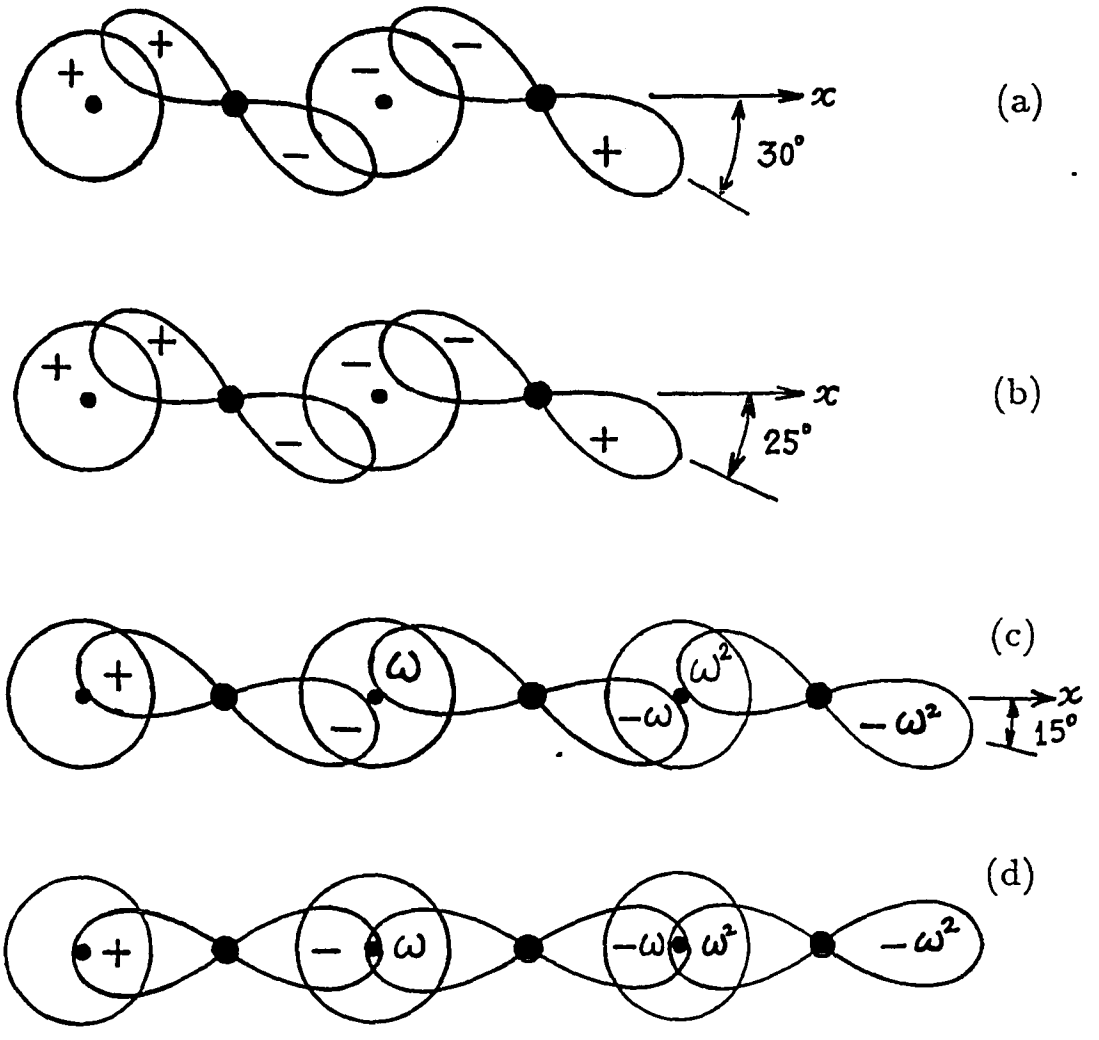

Fig. 21. Schematic diagrams of Be-$p_{x,y}$—H-s bonding. (a) $\overline{M}_2$-point Be-$p_{x,y}$ and H-s orbitals before bonding; (b) $\overline{M}_2$-point orbitals after bonding; (c) $\overline{K}$-point Be-$p_{x,y}$ and H-s orbitals before bonding; (d) $\overline{K}$-point orbitals after bonding. Plus and minus signs and ω ($= e^{i2\pi/3}$) give the phase of the orbitals. Hydrogens are about 1 Å above the surface Be layer.

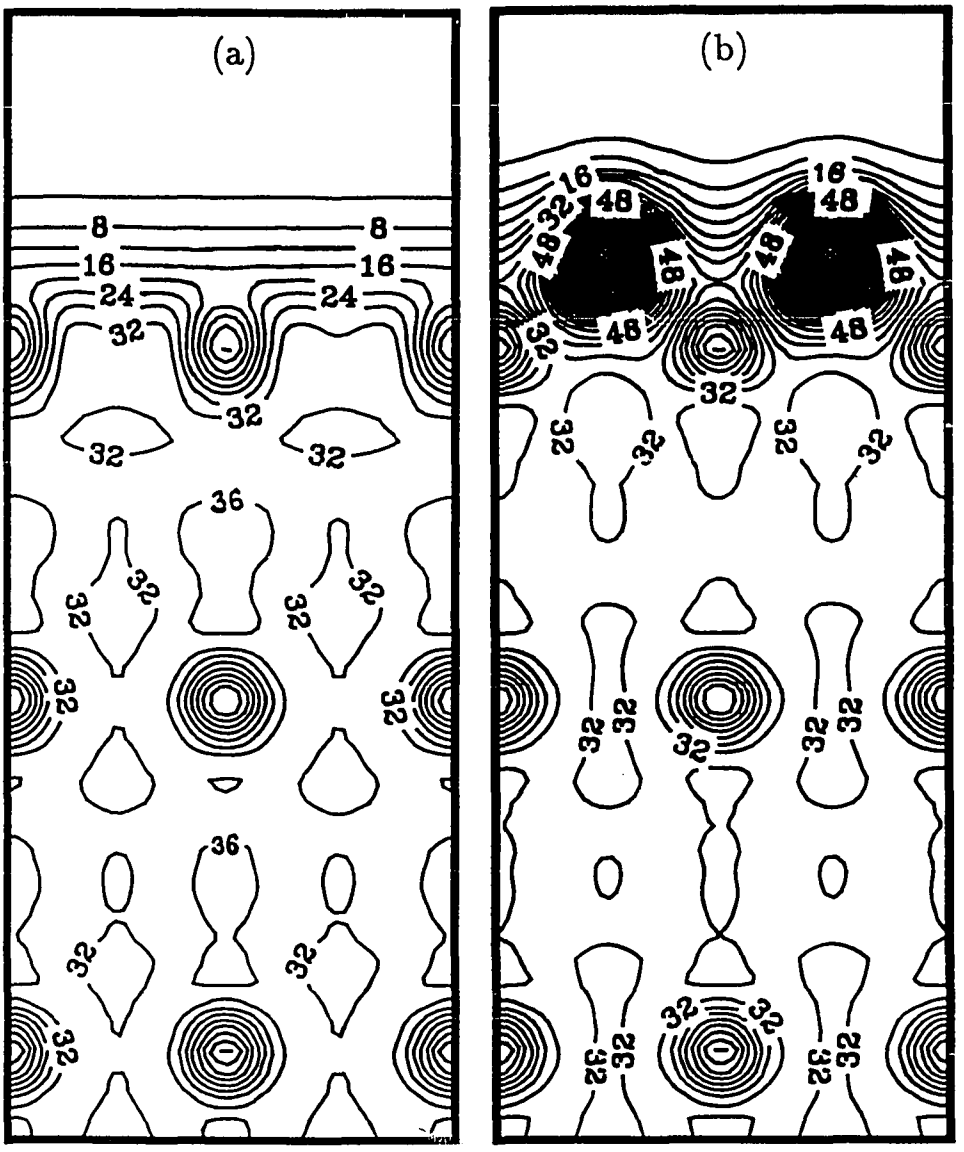

Fig. 22. Contour plots of self-consistent valence charge density in the $(1\bar{1}00)$ plane for (a) clean Be(0001) surface and (b) Be(0001) covered with a monolayer of H in the bridge site. The slab contains ten Be layers in the calculation (the surface, third, and fifth layer atoms are visible). The charge density is in units of $7.7 \times 10^{-3}\ e/\text{Å}^3$.

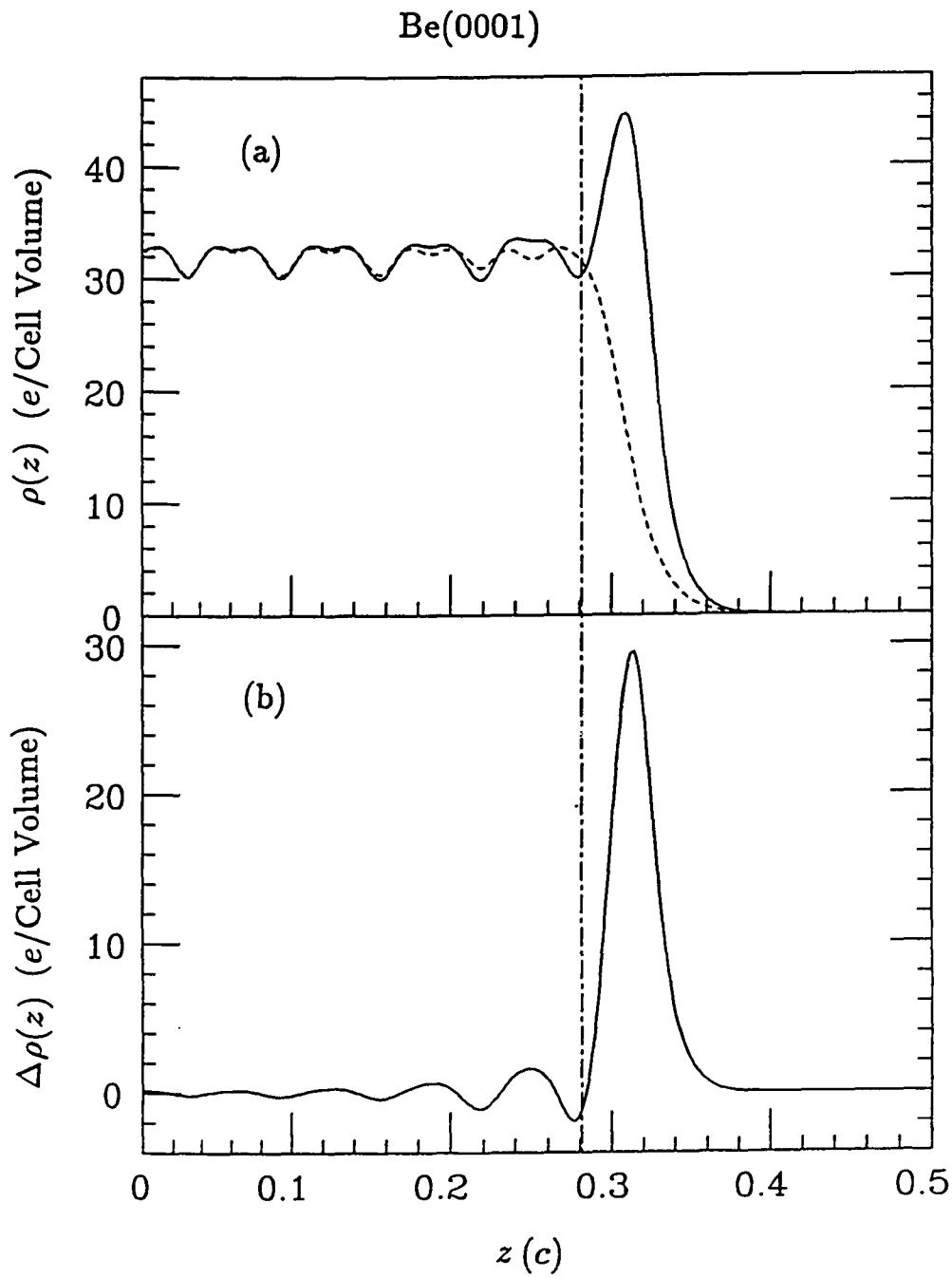

Fig. 23. (a) Valence charge density of a ten-layer Be slab (dashed line) and of the slab covered with monolayers of H in the bridge site (solid line), averaged parallel to the slab, from the center of the slab ($z = 0$) to midpoint between two slabs; (b) difference between the clean and H-covered surface. The dot-dashed line indicates the position of the surface Be layer. Cell volume is 130 Å^3.

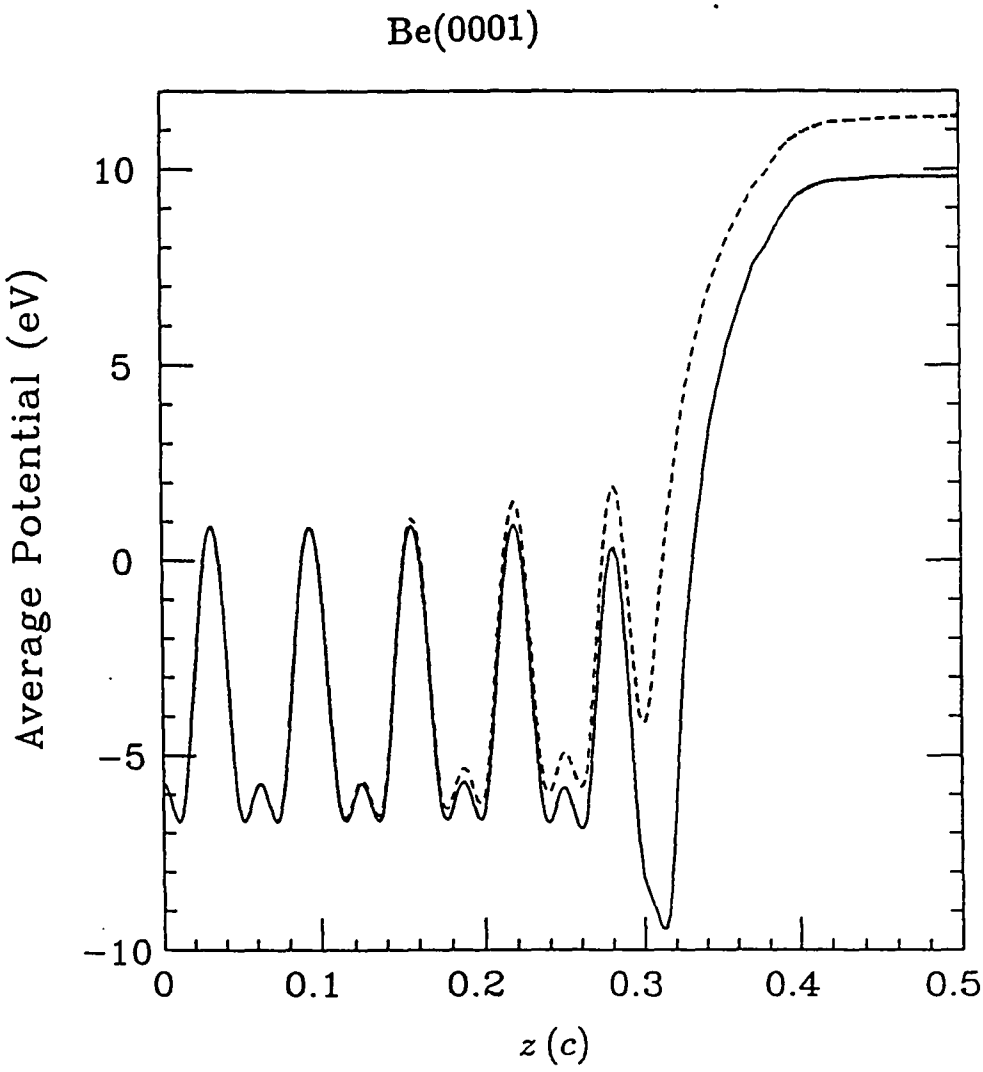

Fig. 24. Self-consistent potential (local part) in the ten-layer Be slab (dashed line) and in the slab covered with monolayers of H in the bridge site, averaged parallel to the surface, from the center of the slab ($z = 0$) to midpoint between two slabs ($z = c/2$). Potentials are lined up at the center of the slab. Potential reference is arbitrary.

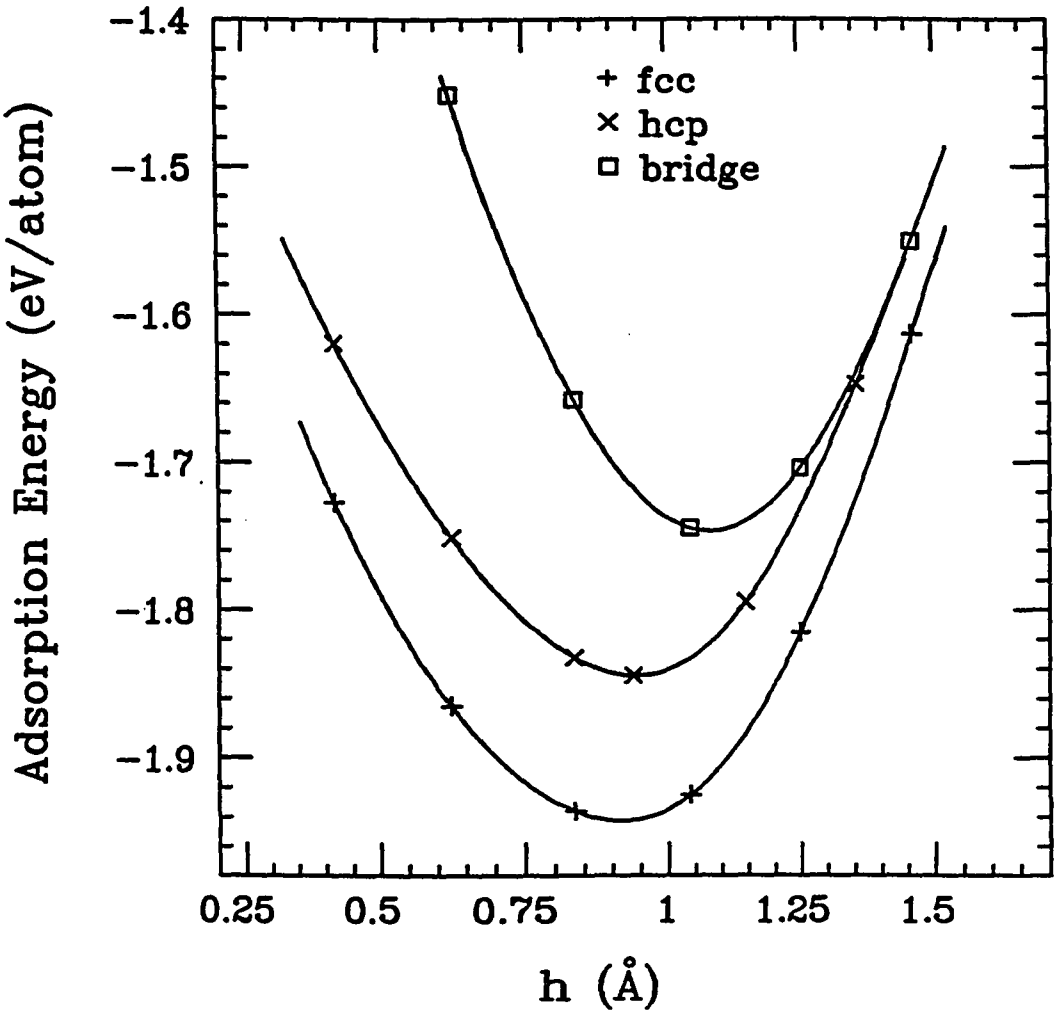

Fig. 25. Calculated adsorption energy of H at different surface sites on Mg(0001) as a function of vertical distance between H and the surface Mg layer.

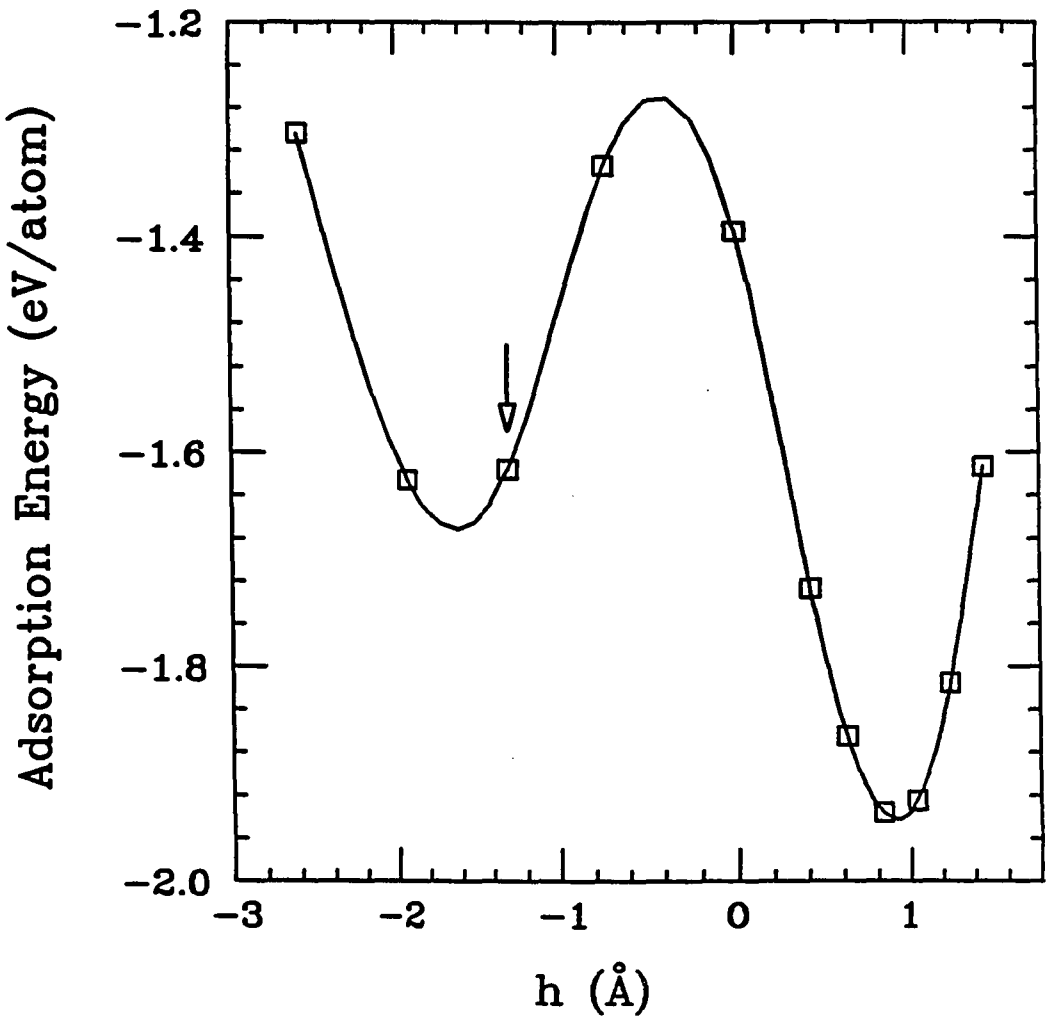

Fig. 26. Calculated adsorption energy of H on Mg(0001) along the path which connects the subsurface octahedral site (indicated by an arrow) and the surface fcc site. The origin is at the surface Mg layer. The leftmost point is at the second Mg layer.

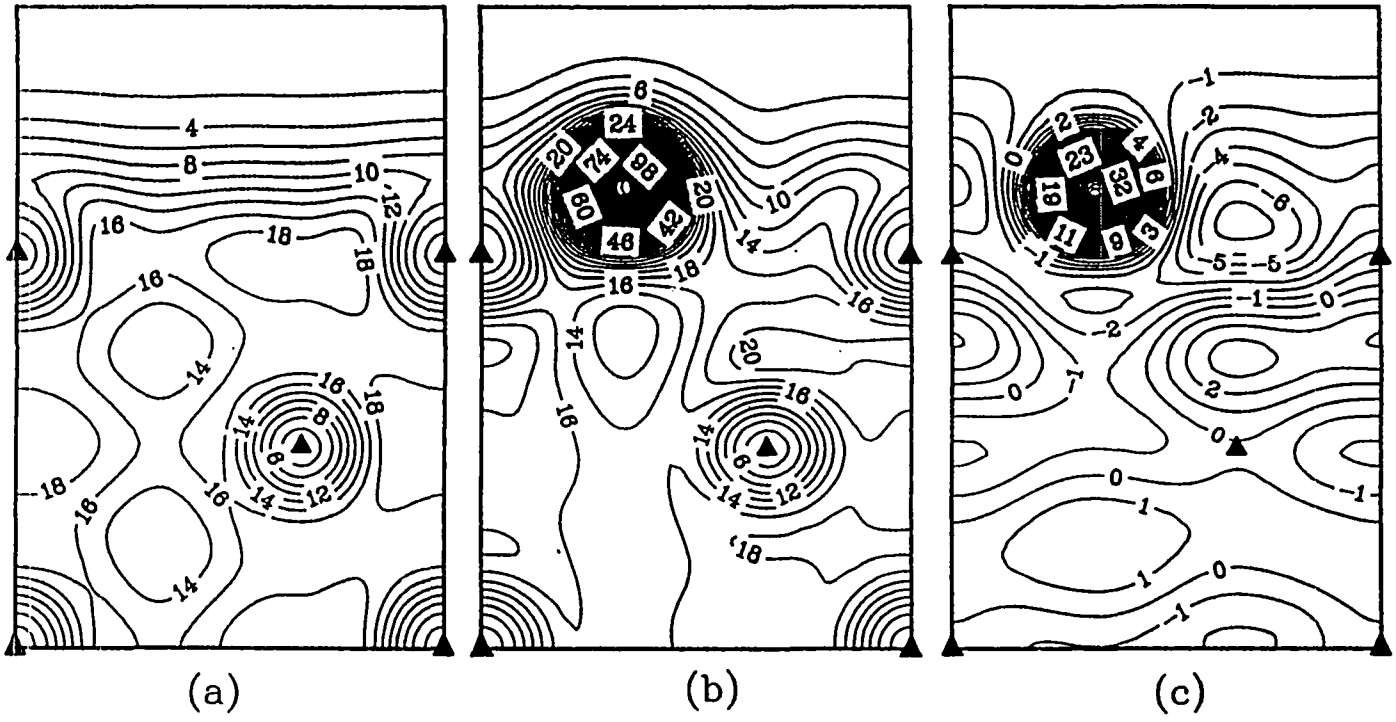

Fig. 27. Contour plots of self-consistent valence charge density in the $(11\bar{2}0)$ plane for (a) clean Mg(0001) surface, (b) Mg(0001) covered with a monolayer of H in the fcc site, and (c) the change upon adsorption from the clean surface and an isolated layer of H. The solid triangles indicate the position of Mg atoms. The slab contains four Mg layers in the calculation (three layers are shown). The charge density is in units of e/Ω with $\Omega = 186$ Å^3.

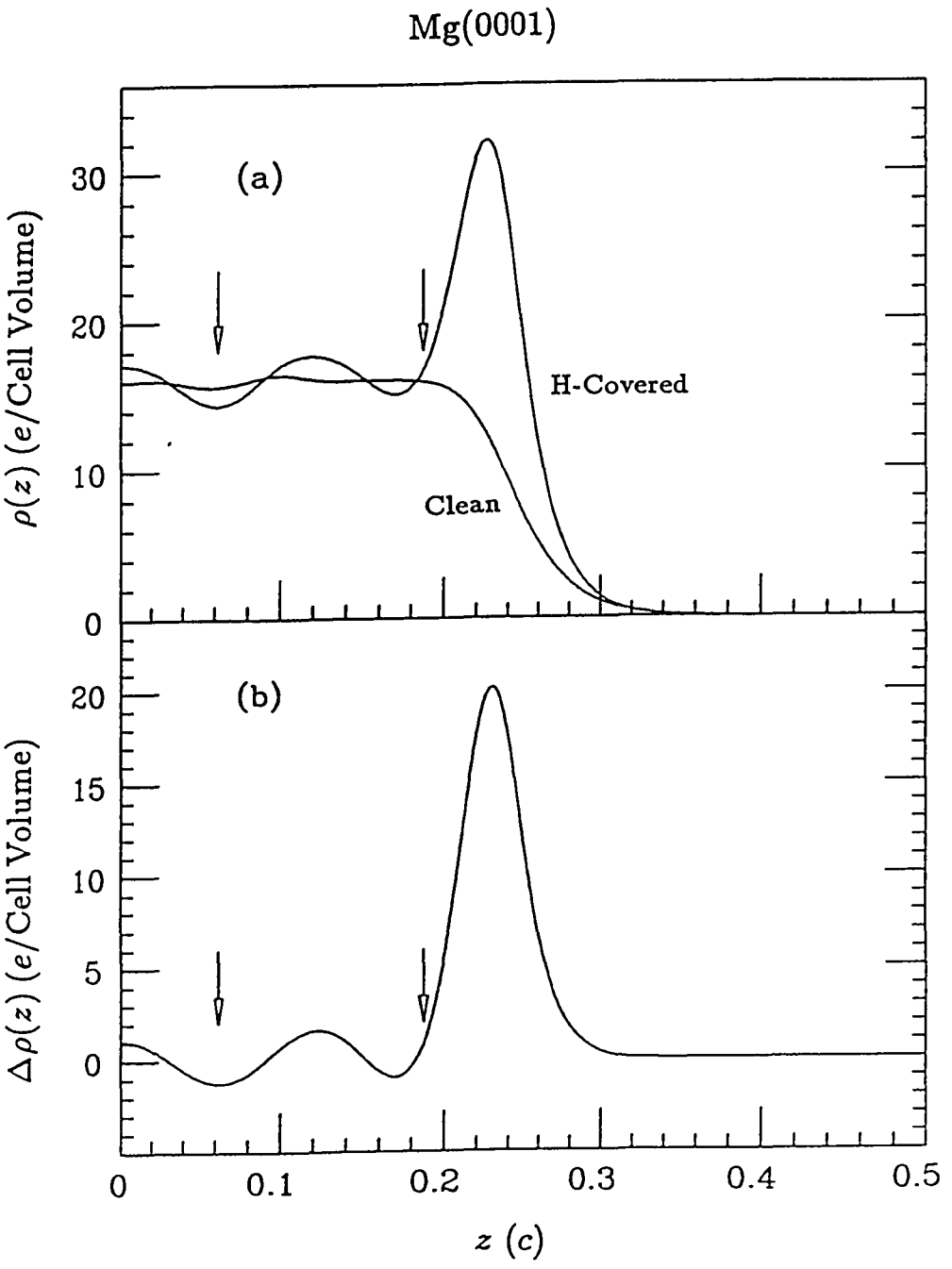

Fig. 28. (a) Valence charge density of a four-layer Mg slab and of the slab covered with monolayers of H in the fcc site, averaged parallel to the slab, from the center of the slab ($z = 0$) to midpoint between two slabs; (b) difference between the clean and H-covered surface. Cell volume is 186 Å^3.

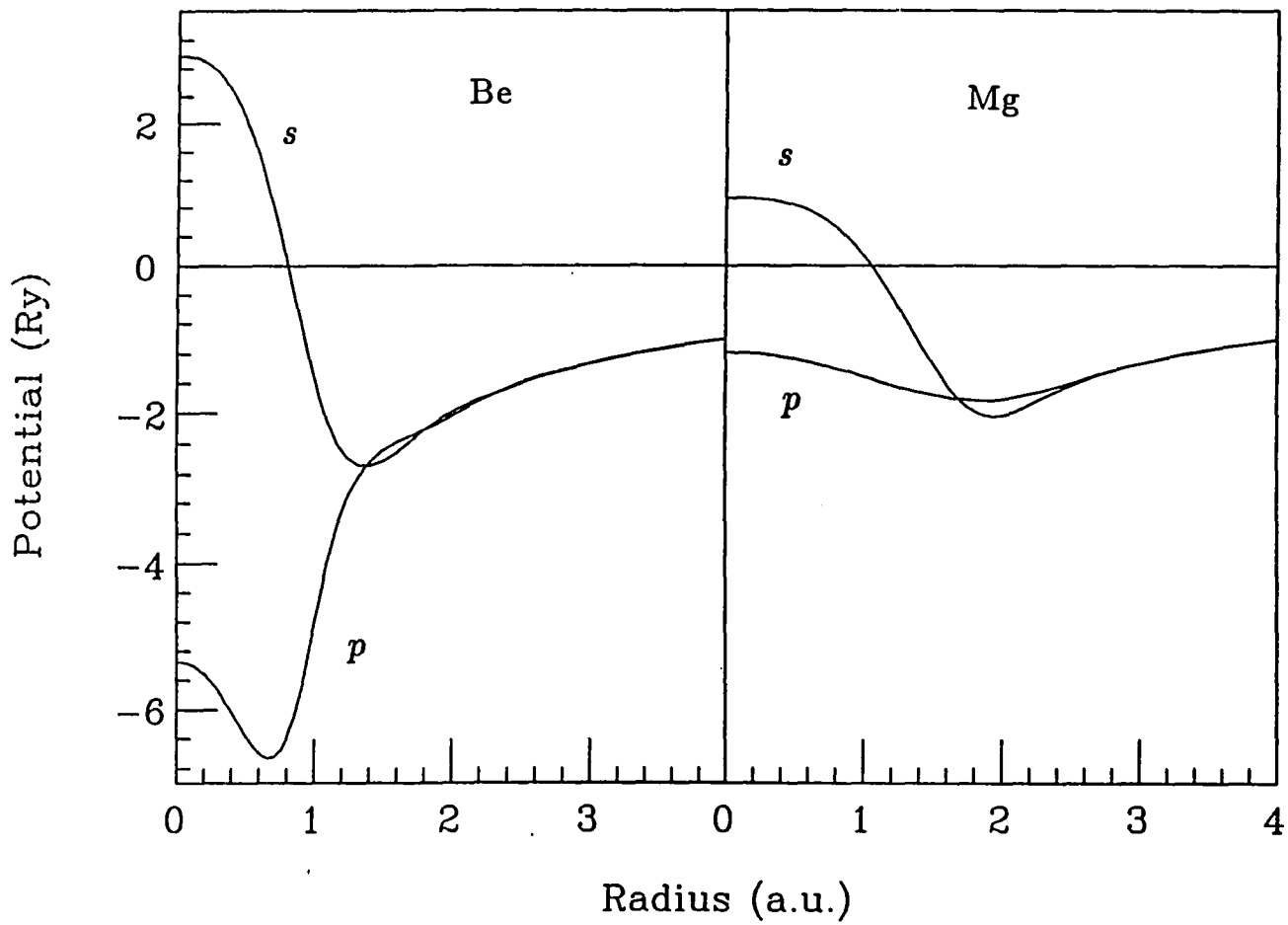

Fig. 29. Comparison of the pseudopotentials of Be and Mg.

Chapter V

Summary

In Chapters III and IV, electronic structure calculations of simple metal hydrides and hydrogen adsorption on simple metals are reported. Here we summarize the results obtained and conclusions drawn in the studies.

(1) Magnesium hydride (MgH_2). Various structural and electronic properties are obtained. Predicted lattice constants and cohesive energy agree well with experiment [1]. The elastic constants, bulk modulus, and the frequency of a zone-center optical mode are also calculated; no experimental results is available on these properties. The electronic band structure and charge density distribution are studied. The compound is found to be a large band-gap insulator (calculated band gap in the local-density approximation is 3.06 eV). The lowest band is free-electron-like near the center of the Brillouin zone. Mg have little influence over the dispersion of the valence bands. The bonding is ionic, but the valence electrons are not all localized around H. Appreciable charge (~19%) is found in interstitial regions. Based on the electronic results, we propose that superconductivity may occur in MgH_2 which is substitutionally doped with monovalent elements (such as Li).

(2) Lithium beryllium hydride ($LiBeH_3$). A structure for $LiBeH_3$ was proposed by Overhauser [2] which suggested metallic bonding and possible high-temperature superconductivity. Two simple structures (perovskite and inverse perovskite) related to the proposed structure are studied. Equilibrium lattice

constants are determined. The atomic density (and valence electron density) determined from the calculated equilibrium lattice constant is about half of that of the proposed structure. The perovskite structure is insulating (with a small band-gap) while the inverse perovskite structure is metallic. The insulating structure is lower in energy. Ionic bonding is the dominant factor in determining the stable structure. Metallization is possible at high pressure. However, the density of states at the Fermi level is low.

(3) Hydrogen adsorption on Be(0001). Be(0001) covered with $p(1 \times 1)$ monolayers of H in the high symmetry sites are studied. The adsorption energy, H—Be bond length, vibrational frequency of H are obtained. The bridge site is found to be the stable adsorption site, which agrees with experiment [3]. The calculated frequency of H vibration perpendicular to the surface also agrees with experiment [3]. Analysis of the energy components indicates that the nonlocal part (of p character) of the electron-ion interaction energy is essential for the preferred bridge site adsorption. The energetics for H to go into the subsurface octahedral site is investigated. The subsurface site is found to be unstable compared to the surface fcc site at a monolayer coverage. The electronic band structure of the clean Be(0001) and of Be(0001) covered with a monolayer of H in the bridge site is investigated. The calculated binding energy of the surface states (SS) of the clean surface agree well with experiment [4]. Upon the adsorption of a H monolayer in the bridge site, the SS of the clean surface deep in the energy gaps disappear. There exists a shallow split-off state at $\overline{\Gamma}$. A strong Be-$p_{x,y}$—H-s bonding band is found near certain parts of the surface Brillouin zone boundary. Because of the low density of states of Be at the Fermi energy, the potential near the clean Be(0001) surface shifts gradually towards higher value. This behavior does not exist in the

H-covered Be slab. Hydrogen thus has the quality of healing the surface. A large reduction (1.6 eV) in the work function is obtained upon the monolayer hydrogen adsorption.

(4) Hydrogen adsorption on Mg(0001). Adsorption of $p(1\times1)$ monolayers of H on the surface is studied. Among the high-symmetry adsorption sites, the fcc site is found to be the stable site. The adsorption energy, equilibrium H—Mg bond length, and H vibrational frequency are calculated. Results are compared with a jellium model calculation [5], where first order effects due to lattice potential perturbation is taken into account. Certain characteristics of our results are in accord with our results for H/Be(0001) and other studies [6]. For example, the H—Mg bond lengths and H vibrational frequency is about the same for H in the fcc site and in the hcp site. The bond length predicted by the jellium model is different by 0.05 Å between fcc and hcp site. The H vibrational frequencies for H in the fcc and hcp site differ by 30 meV. These discrepancies between the jellium model and results of first-principles calculations suggest that the accuracy of the jellium model in quantitative prediction is limited. H in the subsurface octahedral site is unstable compared to H in the the surface fcc site. Our charge density analysis shows that H is in the form of an anion. There are about 1.5 electrons around the H site. This is close to the value in MgH_2 (1.6 electrons). The change in the work function of the Mg(0001) surface due to the adsorption of a monolayer of H is on the order of 0.1 eV.

References for Chapter V

[1] F. H. Ellinger, C. R. Holley, Jr., B. B. McInteer, D. Pavone, R. M. Potter, E. Staritzsky, and W. H. Zachariasen, J. Am. Chem. Soc. **77**, 2647 (1955).

[2] A. W. Overhauser, Phys. Rev. B **35**, 411 (1987).

[3] K. B. Ray and E. W. Plummer, Bull. Am. Phys. Soc. **33**, 655 (1988).

[4] U. O. Karlsson, S. A. Flodström, R. Engelhardt, and W. Gädeke, Solid State Commun. **49**, 711 (1984); R. A. Bartynski, E. Jensen, T. Gustafsson, and E. W. Plummer, Phys. Rev. B **32**, 1921 (1984).

[5] H. Hjelmberg, Surf. Sci. **81**, 539 (1979).

[6] See, e.g., M. Y. Chou and J. R. Chelikowsky, Phys. Rev. Lett. **59**, 1737 (1987).

BIBLIOGRAPHY

Alefeld, G. and J. Völkl (eds.), 1978, *Hydrogen in Metals* I and II (Springer, New York).

Almairac, R., J. L. Sauvajol, C. Benoit, and A. M. Bon, 1978, J. Phys. C **11**, 3157.

Almbladh, C. O., U. von Barth, Z. D. Popovic, and M. J. Stott, 1976, Phys. Rev. B **14**, 2250.

Anderson, O. L., 1966, J. Phys. Chem. Solids **27**, 547.

Angonoa, G., J. Koutecky, and C. Pisani, 1982, Surf. Sci. **121**, 355.

Angonoa, G., J. Koutecky, A. N. Ermoshkin, and C. Pisani, 1984, Surf. Sci. **138**, 51.

Ashcroft, N. W., 1966, Phys. Lett. **23**, 48.

Ashcroft, N. W., 1968, Phys. Rev. Lett. **21**, 1748.

Bachelet, G. B., D. R. Hamann, and M. Schlüter, 1982, Phys. Rev. B **26**, 4199.

Bagus, P. S., H. F. Schaefer, and C. W. Bauschlicher, 1983, J. Chem. Phys. **78**, 1390.

Bambakidis, G. (ed.), 1981, *Metal Hydrides* (Plenum, New York).

Barbee, T. W., A. Garcia, and M. L. Cohen, 1989, Phys. Rev. Lett. **62**, 1150.

Bartynski, R. A., E. Jensen, T. Gustafsson, and E. W. Plummer, 1984, Phys. Rev. B **32**, 1921.

Bauschlicher, C. W., P. S. Bagus, and H. F. Schaefer, 1978, IBM J. Res. Develop. **22**, 213.

Bell, N. A. and G. E. Coates, 1968, J. Chem. Soc. (A) **1968**, 628.

Biswas, R. and D. R. Hamann, 1986, Phys. Rev. Lett. **56**, 2291.

Boettger, J. C. and S. B. Trickey, 1985, Phys. Rev. B **32**, 1356.

Boettger, J. C. and S. B. Trickey, 1986, Phys. Rev. B **34**, 3604.

Born, M. and K. Huang, 1956, *Dynamical Theory of Crystal Lattices* (Oxford University, London).

Bouckaert, L. P., R. Smoluchowski, and E. Wigner, 1936, Phys. Rev. **50**, 58.

Callaway, J., 1964, *Energy Band Theory* (Academic, New York).

Ceperly, D. M. and B. J. Alder, 1980, Phys. Rev. Lett. **45**, 566.

Chadi, D. J. and M. L. Cohen, 1973, Phys. Rev. B **8**, 5747.

Chang, K. J. and M. L. Cohen, 1984, Phys. Rev. B **30**, 4774.

Chou, M. Y. and J. R. Chelikowsky, 1987a, Phys. Rev. B **35**, 2124.

Chou, M. Y. and J. R. Chelikowsky, 1987b, Phys. Rev. Lett. **59**, 1737.

Chou, M. Y. and M. L. Cohen, Solid State Commun. **57**, 785 (1986).

Chou, M. Y., P. K. Lam, and M. L. Cohen, 1982, Solid State Commun. **42**, 861.

Chou, M. Y., P. K. Lam, and M. L. Cohen, 1983, Phys. Rev. B **28**, 4179.

Christiansen, P. A., Y. S. Lee, and K. S. Pitzer, 1979, J. Chem. Phys. **71**, 4445.

Chulkov, E. V., V. M. Silkin, and E. N. Shirykalov, 1987, Surf. Sci. **188**, 287.

Cohen, M. L. and V. Heine, 1970, in *Solid State Physics*, edited by H. Ehrenreich, F. Seitz, and D. Turnbull (Academic, New York), Vol. 24, p. 37.

Cohen, M. L., M. Schlüter, J. R. Chelikowsky, and S. G. Louie, 1975, Phys. Rev. B **12**, 5575.

Colin, R. and D. DeGraï, 1975, Can. J. Phys. **53**, 2142.

CRC, 1985, *Handbook of Chemistry and Physics*, 66th ed. (CRC Press, Boca Raton, Florida).

Dutta, B., S. K. Sarkar, and D. Roy, 1985, Phys. Stat. Sol. **132**, 345.

Ellinger, F. H., C. R. Holley, Jr., B. B. McInteer, D. P vone, R. M. Potter, E. Staritzsky, and W. H. Zachariasen, 1955, J. Amer. Chem. Soc. **77**, 2647.

Felsteiner, J., M. Heilper, I. Gertner, A. C. Tanner, R. Opher, and K.-F. Berggren, 1981, Phys. Rev. B **23**, 5156.

Flodström, S. A., L.-G. Petersson, and S. B. M. Hagström, 1976, J. Vacuum Sci. Technol. **13**, 280.

Fomenko, V. S., 1966, *Handbook of Thermionic Properties* (Plenum, New York).

Friedel, J., 1952, Phil. Mag. **43**, 153.

Froyen, S. and M. L. Cohen, 1984, Phys. Rev. B **26**, 3770.

Gay, J. G., W. A. Albers, Jr., and F. J. Arlinghaus, 1968, J. Phys. Chem. Solids **29**, 1449.

Gell-Mann, M. and K. Brueckner, 1957, Phys. Rev. **106**, 364.

Gibb, T. R. P., 1962, in *Progress in Inorganic Chemistry*, edited by F. A. Cotton (Interscience, New York), Vol. 3, p. 315.

Gray, D. E. (ed.), 1972, *American Institute of Physics Handbook*, 3rd ed. (McGraw-Hill, New York).

Green, A. K. and E. Bauer, 1978, Surf. Sci. **74**, 676.

Gunnarsson, O. and R. O. Jones, 1980, Phys. Scr. **21**, 394.

Gunnarsson, O., B. I. Lunqvist, and J. W. Wilkins, 1975, Phys. Rev. B **12**, 1257.

Gupta, M., 1983, in *Electronic Structure and Properties of Hydrogen in Metals*, edited by P. Jena and C. B. Satterthwaite (Plenum, New York), p. 321.

Gupta, M., 1984, in *The Electronic Structure of Complex Systems*, edited by P. Phariseau and W. M. Tammerman (Plenum, New York), p. 243.

Gupta, M. and L. Schlapbach, 1988, in *Hydrogen in Intermetallic Compounds* I, edited by L. Schlapbach (Springer, New York), p. 139.

Hamann, D. R., M. Schlüter, and C. Chiang, 1979, Phys. Rev. Lett. **43**, 1494.

Harrison, W. A., 1966, *Pseudopotentials in the Theory of Metals* (Benjamin, New York).

Hedin, L. and B. I. Lundqvist, 1971, J. Phys. C **4**, 2064.

Heine, V., 1970, in *Solid State Physics*, edited by H. Ehrenreich, F. Seitz, and D. Turnbull (Academic, New York), Vol. 24, p. 1.

Heine, V. and D. Weaire, 1970, in *Solid State Physics*, edited by H. Ehrenreich, F. Seitz, and D. Turnbull (Academic, New York), Vol. 24, p. 249.

Herring, C., 1940, Phys. Rev. **57**, 1169.

Hjelmberg, H., 1979, Surf. Sci. **81**, 539.

Hohenberg, P. and W. Kohn, 1964, Phys. Rev. **136**, B864.

Hurd, J. J. and R. O. Adams, 1968, J. Vac. Sci. Technol. **5**, 183.

Hybertsen, M. S. and S. G. Louie, 1985, Phys. Rev. Lett. **55**, 1418.

Ihm, J., A. Zunger, and M. L. Cohen, 1979, J. Phys. C **12**, 4409.

Ihm, J. and J. D. Joannopoulos, 1981, Phys. Rev. B **24**, 4191.

Jena, P. and C. B. Satterthwaite (eds.), 1983, *Electronic Structure and Properties of Hydrogen in Metals* (Plenum, New York).

Jena, P. and K. S. Singwi, 1978, Phys. Rev. B **17**, 3518.

Karlsson, U. O., S. A. Flodström, R. Engelhardt, and W. Gädeke, 1984, Solid State Commun. **49**, 711.

Kerker, G. P., 1980, J. Phys. C **13**, L189.

Kittel, C., 1986, *Introduction to Solid State Physics*, 6th ed. (Wiley, New York).

Kohn, W., 1985, in *Highlights of Condensed-Matter Theory*, edited by F. Bassani, F. Fumi, and M. P. Tosi (North-Holland, New York), p. 1.

Kohn, W. and L. J. Sham, 1965, Phys. Rev. **140**, A1133.

Kohn, W. and P. Vashishta, 1983, in *Theory of the Inhomogeneous Electron Gas*, edited by S. Lundqvist and N. H. March (Plenum, New York), p. 79.

Krasko, G., 1982, in *Metal-Hydrogen Systems*, edited by T. Nejat Veziroglu (Pergamon, New York), p. 367.

Lam, P. K. and M. L. Cohen, 1981, Phys. Rev. B **24**, 4228.

Lam, P. K. and M. L. Cohen, 1983, Phys. Rev. B **27**, 5986.

Lam, P. K. and R. Yu, 1988, in Proceedings of International Meeting on Advanced Materials, Symposium I: Hydrogen Absorbing Materials, Materials Research Society, Tokyo, 1988.

Lang, N. D., 1983, in *Theory of the Inhomogeneous Electron Gas*, edited by S. Lundqvist and N. H. March (Plenum, New York), p. 309.

Lehmann, G. and M. Taut, 1972, Phys. Stat. Sol. (b) **54**, 469.

Levy, M., 1982, Phys. Rev. A **26**, 1200.

Lindner, P. and K-F. Berggren, 1973, Int. J. Quan. Chem. **7**, 667.

Louie, S. G., S. Froyen, and M. L. Cohen, 1982, Phys. Rev. B **26**, 1738.

Mackay, K. J. H. and N. A. Hill, 1963, J. Nucl. Mater. **8**, 263.

Mackay, K. M., 1966, *Hydrogen Compounds of the Metallic Elements* (Spon, London), Chapter 4.

Mackay, K. M., 1973, *Comprehensive Inorganic Chemistry*, 1st ed. (Pergamon, New York), Vol. 1.

March, N. H., 1983, in *Theory of the Inhomogeneous Electron Gas*, edited by S. Lundqvist and N. H. March (Plenum, New York), p. 1.

Michaelson, H. B., 1977, J. Appl. Phys. **48**, 4729.

Min, B. I., H. J. F. Jansen, and A. J. Freeman, 1986, Phys. Rev. B **33**, 6383.

Monkhorst, H. J. and J. D. Pack, 1976, Phys. Rev. B **33**, 5188.

Muller, W. M., J. P. Blackledge, and G. G. Libowitz (eds.), 1968, *Metal Hydrides* (Academic, New York).

Murnaghan, F. D., 1944, Proc. Natl. Acad. Sci. USA **30**, 244.

Murphy, R. B., J. M. Mundenar, K. D. Tsui, and E. W. Plummer, 1988, Bull. Am. Phys. Soc. **33**, 655.

Muscat, J. P., 1986, Phys. Rev. B **33**, 8136.

Muscat, J. P. and D. M. Newns, 1978, in *Progress in Surface Science*, edited by S. G. Davison (Pergamon, New York), Vol. 9, p. 1.

Nachman, J. F. and D. A. Rohy, 1982, in *Metal-Hydrogen Systems*, edited by T. N. Veziroglu (Pergamon, New York), p. 557.

Nordlander, P., 1984, Surf. Sci. **136**, 59.

Norskov, J. K., 1977, Solid State Commun. **24**, 691.

Norskov, J. K., 1979, Phys. Rev. B **20**, 446.

Norskov, J. K., 1982a, Phys. Rev. Lett. **48**, 1620.

Norskov, J. K., 1982b, Phys. Rev. B **26**, 2875.

Norskov, J. K. and N. D. Lang, 1980, Phys. Rev. B **21**, 2131.

Overhauser, A. W., 1987a, Int. J. Mod. Phys. **1**, 927.

Overhauser, A. W., 1987b, Phys. Rev. B **35**, 411.

Pack, J. D. and H. J. Monkhorst, 1977, Phys. Rev. B **16**, 1748.

Papaconstantopoulos, D. A. and B. M. Klein, 1977, Ferroelectrics **16**, 307.

Papaconstantopoulos, D. A., L. L. Boyer, B. M. Klein, A. R. Williams, V. L. Morruzzi, and J. F. Janak, 1977, Phys. Rev. B **15**, 4221.

Paul, J., 1988, Phys. Rev. B **37**, 6164.

Pauling, L., 1942, *The Nature of the Chemical Bond*, 2nd ed. (Cornell University Press, Ithaca).

Perdew, J. P. and A. Zunger, 1981, Phys. Rev. B **23**, 5048.

Phillips, J. C., 1973, *Bonds and Bands in Semiconductors* (Academic, New York).

Phillips, J. C. and L. Kleinman, 1959, Phys. Rev. **116**, 287.

Pines, D., 1963, *Elementary Excitations in Solids* (Benjamin, New York).

Ray, K. B. and E. W. Plummer, 1988, Bull. Am. Phys. Soc. **33**, 655.

Rhodin, T. N. and G. Ertl, 1979, *The Nature of the Surface Chemical Bond* (North-Holland, New York).

Schlapbach, L., 1988, *Hydrogen in Intermetallic Compounds* I and II (Springer, New York).

Schlüter, M., J. R. Chelikowsky, S. G. Louie, and M. L. Cohen, 1975, Phys. Rev. B **12**, 4200.

Schneider, T., 1969, Helv. Phys. Acta **42**, 957.

Selvam, P., B. Viswanathan, C. S. Swamy, and V. Srinivasan, 1986, Int. J. Hydrogen Energy **11**, 169.

Shimizu, H., E. M. Brady, H. K. Mao, and P. M. Bell, 1981, Phys. Rev. Lett. **47**, 128.

Slater, J. C., 1974, *The Self-Consistent Field for Molecules and Solids* (McGraw-Hill, New York), Vol. 4.

Smith, G. S., Q. C. Johnson, D. K. Smith, D. E. Cox, R. L. Snyder, R.-S. Zhou, and A. Zalkin, 1988, Solid State Commun. **67**, 491.

Stander, C. M. and R. A. Pacey, 1978, J. Phys. Chem. Solids **39**, 829.

Stritzker, B., 1983, in *Electronic Structure and Properties of Hydrogen in Metals*, edited by P. Jena and C. B. Satterthwaite (Plenum, New York), p. 309.

Stritzker, B. and H. Wühl, 1978, in *Hydrogen in Metals* II, edited by G. Alefeld and J. Völkl (Springer, New York), p. 243.

Switendick, A. C., 1976, in *Superconductivity in d- and f-Band Metals*, edited by D. H. Douglass (Plenum, New York), p. 593.

Switendick, A. C., 1978, in *Hydrogen in Metals* I, edited by G. Alefeld and J. Völkl (Springer, New York), p. 101;

Tomanek, D., S. G. Louie, and C. T. Chan, 1986, Phys. Rev. Lett. **57**, 2594.

Umrigar, C. and J. W. Wilkins, 1985, Phys. Rev. Lett. **54**, 1551.

Van Hove, M. A. and S. Y. Tong, 1979, *Surface Crystallography by LEED* (Springer, New York), p. 253.

von Barth, U., 1984, in *The Eletronic Structure of Complex Systems*, edited by P. Phariseau and W. M. Temmerman (Plenum, New York), p. 67.

von Barth, U. and L. Hedin, 1972, J. Phys. C **5**, 1629.

von Barth, U. and C. D. Gelatt, 1980, Phys. Rev. B **21**, 2222.

Weil, K. H. and V. Nardi, 1985, Int. J. Hydrogen Energy **10**, 859.

Weinert, M., A. J. Freeman, and S. Ohnishi, 1986, Phys. Rev. Lett. **56**, 2295.

Wigner, E., 1934, Phys. Rev. **46**, 1002.

Williams, A. R. and U. von Barth, 1983, in *Theory of the Inhomogeneous Electron Gas*, edited by S. Lundqvist and N. H. March (Plenum, New York), p. 189.

Wimmer, E., 1984, J. Phys. F **14**, 681.

Wiswall, R., 1978, in *Hydrogen in Metals* II, edited by G. Alefeld and J. Völkl (Springer, New York), p. 202.

Wood, D. M. and A. Zunger, 1985, J. Phys. A **18**, 1343.

Wyckoff, R. W. G., 1963, *Crystal Structures*, 2nd ed. (Interscience, New York), Vol. 1, p. 250.

Yin, M. T. and M. L. Cohen, 1980, Phys. Rev. Lett. **45**, 1004.

Yu, R. and P. K. Lam, 1988a, Phys. Rev. B **37**, 8730.

Yu, R. and P. K. Lam, 1988b, Phys. Rev. B **38**, 3576.

Yu, R. and P. K. Lam, 1989, Phys. Rev. B **39**, 5035.

Zunger, A., 1979, J. Vac. Sci. Technol. **16**, 1337.